IJCE

Printed by
Diagnosis Engineering & Technology Corp., Japan

International Journal of Comprehensive Engineering

ISSN 2186-2680

Volume 2, Number 2, June 2013

IJCE

Published by
International Association of Comprehensive Engineering (IACE)

http://www.iace-journal.org/

Honorary Editors

Toshio TOYOTA , Japan Institute of Condition Diagnosis Technology, Japan

Jinji GAO, Academician of the Chinese Academy of Engineering (CAE)

Hisayoshi MATSUYAMA, Vice-president The Society of Plant Engineers Japan

Editor-In-Chief

Peng CHEN
Mie University, 1577 Kurimamachiya-cho,Tsu-shi, Mie-ken, 514-8507 Japan
E-mail : chen@bio.mie-u.ac.jp

Associate Editors

Zhengjia HE, Xi'an Jiaotong University, China
E-mail: hzj@mail.xjtu.edu.cn

Maria Q. FENG, University of California, USA
E-mail: mfeng@uci.edu

Tadao KAWAI, Osaka City University, Japan
E-mail: kawai@mech.eng.osaka-cu.ac.jp

Susumu OKUMURA, University of Shiga Prefecture, Japan
E-mail: okumura.s@usp.ac.jp

Lei Li, Faculty of Science and Engineering Hosei University, Japan
E-mail:lilei@k.hosei.ac.jp

Huaqing WANG, Beijing University of Chemical Technology, China
E-mail: hqwang@mail.buct.edu.cn

Editorial Board

Changzheng CHEN, Shenyang University of Technology, China

Jin CHEN, Shanghai Jiaotong University, China

Fulei CHU, Tsinghua University, China

Zhiqian DONG, China development investment company

Lixin GAO, Beijing University of Technology, China

Jie HAN, Zhengzhou University, China

Min HU, Agent Director, China Plant Engineering Editorial office

Niaoqing HU, National University of Defense Technology, China

Jianping HU, Jiangsu University, China

Lixin LU, Jiangnan University, China

Ke LI, Jiangnan University, China

Hanping MAO, Jiangsu University, China

Zhongxing Li, Jiangsu University, China

Arata MASUDA, Kyoto Institute of Technology, Japan

Tetsuro MITOMA, Mitsui Chemicals, Inc., Japan

Hiromitsu OHTA, National Fisheries University, Japan

Yelian MIAO, Nanjing University of Technology, China

R.R.Pechon, Agriculture,Bohol Agricultural Promotion Center,Philippines

Zhongyong PAN, Jiangsu University, China

Yimin. SHAO, Chongqing University, China

Noriaki SATONAGA, Showa Denko K.K., Japan

Yukio WATANABE, TOSHIBA CORPORATION, Japan

Toshiaki WAKABAYASHI, Kagawa University, Japan

Taiyong WANG, Tianjin University, China

Shiming WANG, Shanghai Ocean University, China

Hongtao XUE, Mie University, Japan

Xiaoli XU, Beijing Information Science and Technology University, China

Mitsushi YAMASHITA, Mie University, Japan

Ruqiang YAN, School of Instrument Science and Engineering, China

Yanyang ZI, Xi'an Jiaotong University, China

Chongsheng YUAN, DIAZYME Corporation, USA

Secretariat Board

Email : ijce@nifty.com

(Head) **Hao SUN,** Jiangnan University, China
Email : sunhao@jiangnan.edu.cn

Ke LI, Jiangnan University, China

Feng WANG, Beijing University of Chemical Technology, China

Hongtao XUE, Mie University, Japan

Haiyang JIANG, MieUniversity, Japan

International Journal of Comprehensive Engineering (IJCE)

International Journal of Comprehensive Engineering (IJCE) is an international interdisciplinary journal that integrates publication from aspects of research on engineering science. This journal provides a medium of communication among engineers and scientists who have engaged in research and development concerning the fields of comprehensive engineering, while maintaining a healthy balance between fundamental and experimental topics. Now, the journal has three separate fields, the scopes of which are Part A: Maintenance Engineering; Part B: Intelligent Engineering; Part C: Engineering in Agriculture, Ocean and Light Industry shown in flows, and other specialized fields will also be updated in the near future.

Part A: Maintenance Engineering

Executive editors：

Prof. Dr. Yanyang ZI
Xi'an Jiaotong University, China
E-mail: ziyy@mail.xjtu.edu.cn

Associate Prof. Dr. Hiromitsu OHTA
National Fisheries University, Japan
E-mail: ohta@fish-u.ac.jp

Prof. Dr. Huaqing WANG
Beijing University of Chemical Technology, China
E-mail: hqwang@mail.buct.edu.cn

Topics of interest for submission on the field of maintenance engineering include, but are not limited to:
Condition Diagnosis Engineering and Technology; Sensing Technology; Maintenance Management; Fault Tolerant System; Fault Self-Recovery Engineering; E-Maintenance; Signal Processing; Risk, Health and Safety Management; Structural Health Monitoring; Information and Communication Technology; Data and Information Fusion; Reliability/Quality; Maintenance Robot; Data Quality and Acquisition; Human Factors; Education and Training; Risk Based Engineering; Others on Maintenance.

Part B: Intelligent Engineering

Executive editors：

Prof. Dr. Huaqing WANG
Beijing University of Chemical Technology, China
E-mail: hqwang@mail.buct.edu.cn

Associate Prof. Dr. Arata MASUDA
Kyoto Institute of Technology, Japan
E-mail: masuda@kit.ac.jp

Associate Prof. Dr. Ke LI
Jiangnan University, China
E-mail: like@jiangnan.edu.cn

Topics of interest for submission on the field of intelligent engineering include, but are not limited to:
Application of Artificial Intelligence in Engineering; Intelligent Design, Modeling, Planning and Control for Applied Engineering; Intelligent Robot System; Intelligent Fault Diagnosis; Intelligent Signal Processing for Applied Engineering; Others on Intelligent Engineering.

Part C: Engineering in Agriculture, Ocean and Light Industry

Executive editors (Agriculture):

Prof. Dr. Hanping MAO
Jiangsu University, China
E-mail: maohp@ujs.edu.cn

Prof. Dr. Jianping HU
Jiangsu University, China
E-mail: hujp@ujs.edu.cn

Executive editor (Ocean):

Prof. Dr. Shiming WANG
Shanghai Ocean University, China
E-mail: smwang@shou.edu.cn

Executive editor (Light Industry):

Prof. Dr. Lixin LU
Jiangnan University, China
E-mail: lulx@jiangnan.edu.cn

Topics of interest for submission on the field of engineering in agriculture, ocean and light industry include, but are not limited to:
Agriculture Engineering: Agricultural Equipment and Mechanical Engineering; Agricultural Bioenvironmental Engineering; Agricultural Renewable Energy Engineering; Agricultural Produce Processing Engineering; Agricultural Information and Electrical Technologies; Others on Agricultural Engineering.
Ocean Engineering: New Ocean Energy; Ocean Maintenance Technology; Ocean Monitoring Technology; Ocean Diagnosis Method; Ocean Experimental Development; Professional Sensor Technology; Observational and Computational Tools Others on Ocean Engineering.
Light Industry Engineering: Agri-food Products Processing/Packaging Technology and Equipment; Comprehensive Utilization of Resource; Preservation; Storage and Packaging of Agri-food Products; Innovative IT Applications in Agri-food Chain; Sensing, Testing, Automation and Internet of Things Technologies; Green Environmental Protection; Energy Saving Technologies; Others on Light Industry.

Manuscript Submission

Manuscripts should be submitted online at http://www.iace-journal.org/ by registering and logging in to the website of the IJCE. Once you have registered, please click the “Submit Manuscript” to go to the submission from. Please use the MS Word template file to prepare your manuscript. Manuscript prepared in MS Word must be converted into a single file before submission. The Microsoft Word template file can be downloaded from the website of the IJCE.

Submission Declaration

The submission, such as articles, reviews, technical report etc., to the IJCE means these facts that the work described has not been published previously, that it is not under consideration for publication elsewhere, that its publication is approved by all authors and tacitly or explicitly by the responsible authorities where the work was carried out, and that, if accepted, it will not be published elsewhere including electronically in the same form, in English or in any other language, without the written consent of the copyright-holder.

Copyright

Authors will be asked to complete a "Copyright Transfer Statement", when submitting the manuscript. Acceptance of the agreement will ensure the widest possible dissemination of information. Permission of the publisher is required for resale or distribution outside the institution and for all other derivative works, including compilations and translations. The "Copyright Transfer Statement" can be downloaded from the website of the IJCE as follows:
http://www.iace-journal.org/views/Copyright_Transfer_Statement.pdf.

Review Policy

The following types of contribution to the IJCE are peer-reviewed: Articles, Reviews and Technical Reports. The articles accepted for publishing in the IJCE include regular paper and letter, which will be decided by editors according the reviewing results. All forms of published correction may also be peer-reviewed at the discretion of the editors. Other contributed types to the IJCE, particularly if they present technical information, may be peer-reviewed at the discretion of the editors. For any general questions and comments about the peer-review process, the journal or its editorial policies that are not mentioned here, please contact us using the email: ijce@nifty.com. Questions about a specific submitted manuscript should be directed to the executive editor who is handling the manuscript.

International Journal of Comprehensive Engineering (IJCE)

Volume 2, Number 2, June 2013 (ISSN 2186-2680)

Part A : Maintenance Engineering

106 Wenrong Xiao, Yanyang Zi, Baojia Chen and Zhengjia He
Operation Reliability Estimation Based on Degradation Feature Extraction from Censored Data of Cutting Tool

117 Xinpeng Zhang, Niaoqing Hu and Lei Hu
An Improved Detector Generation Method based on Artificial Immunity

125 Shuilong He, Yanyang Zi, Zhengjia He, Zigang Cai and Wangpeng He
A review on rolling bearing fatigue life prediction

135 Hongfang Yuan, Fangming Li , Xi Cao , Huaqing Wang , Jianfeng Yang and Wenbin Liu
Application of intelligent data unit based on embedded Linux in wireless monitoring system of rolling bearings

142 Ziqiang Sun and Changzheng Chen
Application of the multifractal method to the feature extraction of megawatt wind turbine main bearing

Part B : Intelligent Engineering

149 Hongtao Xue , Huaqing Wang and Peng Chen
Sequential Diagnosis using Support Vector Machine and Relative Ratio Symptom Parameters for Identifying Early-stage Structural Faults of Rotating Machinery

161 Hongkun Li , Shuai Zhou and Zhenggang Guo
Investigation on Machine Condition Classification by Using Multi-Scale Entropy Feature Extraction and Support Vector Machine

Part C : Engineering in Agriculture, Ocean Industry and Light Industry

172 Chunhui Qi , Jianping Hu , Jun Ma , Jianbing Zhang and Xuejun Yang
Trajectory Planning and Motion Simulation on High-Speed Transplanting Bowl Seeding Robot

180 Chunfang Song , Zhengwei Cui , Chunyang Li and Gelan Qian
Shrinkage During Microwave-vacuum Drying for Carrot Slices

189 Hanping Mao , Bo Hu, Shicha Zheng and Zhongping Xiang
Identifying Weeds in Cotton Field with Morphological Skeleton

196 Shouqi Yuan , Wei Liu , Zhongyong Pan and Xiaojun Li
Review on Rotating Stall in Pumps

208 Hiromitsu Ohta , Keiji Sasada , Shintaro Shiota and Makoto Nakamura
Non Destructive Estimation Method about the Texture of Raw Puffers Meat on its Frequency Response
-- Identification of Optimum Discriminate on Sensitivity by Discrimination Index--

Copyright © 2012 DET Corp., Japan All Rights Reserved
International Journal of Comprehensive Engineering
Part A, 2(2), 106-116, 2013
Doi: 14270/IJCE2013.2.2.a106
Regular paper

ISSN 2186-2680
e-ISSN 2186-2656
www.iace-journal.org

Operation Reliability Estimation Based on Degradation Feature Extraction from Censored Data of Cutting Tool

Wenrong Xiao [1], Yanyang Zi [1,#], Baojia Chen [2], Zhengjia He [1]

[1] State Key Laboratory for Manufacturing Systems Engineering, Xi`an Jiaotong University, Xi`an 710049, PR China
[2] College of Mechanical & material Engineering school, Three gorges university, Yichang 443002, China

[#] Corresponding author: ziyy@mail.xjtu.edu.cn; Tel.: +86-29-82667963;

Abstract: It is difficult to acquire the run-to-failure operating status information of device in the industrial process. How to use the censored data from this information to estimate operation reliability of device becomes vital. Accordingly, this paper proposes an estimation method of operation reliability that can carry out the estimation of instantaneous reliability and the prediction of remained useful life at the same time, by means of the censored data. The key technology is to build an estimation model of instantaneous reliability using the censored data. The three steps of modeling are as follows: Firstly, on-line signals of various types are measured during the operating process. Second, after degradation features are extracted from these signals, considering only censored data, Gaussian process for machine learning is employed to predict various degradation feature indicator values at the time of failure, and distribution hypotheses are adopted to obtain their probability density functions. Third, the Bayes' theorem is used to acquire the instantaneous reliability model. A CNC cutting tests shows the plausibility and effectiveness of the proposed method.

Keywords: Operation Reliability Estimation, Censored Data, Cutting Tool, Bayes' theorem.

Received: Jul. 10,2012 / Accepted: Feb. 20,2013 / Published: Jul. 5,2013

1. Introduction

Aircraft landing gear is a kind of difficult machining and high value workpiece, and its scrap will inevitably causes great economic loss. In order to preventing workpiece from scrap resulting from tool failure, the cutting tools that are far from reaching their effective life are forced to replace frequently. In fact, an aircraft landing gear generally costs millions of Yuan, but the cutting tool is worth hundreds or thousands of Yuan. Therefore, the above-mentioned method directly increases processing cost, and obviously weakens the market competitiveness. How shall we lengthen the service time of cutting tool on the precondition of guaranteeing normal machining? This paper attempts at discussing the similar problem and providing an approach.

Without loss of generality, the difficulties in solving the above-mentioned problem are summed up as follows:

1) There is not a run-to-failure sample set. During processing, cutting tools are always replaced ahead of time according to processor's practical experience. Namely, there are only censored samples.

2) The number of samples is small. In order to reducing waste and affecting production efficiency as little as possible, only limited number of workpieces can be measured. Namely, it is a small sample problem.

3) The reliability of individual-observed must be shown in real time. And then, whether the observed individual will be decided to replace depends on the real-time estimation value of operation reliability.

However, traditional reliability based on the statistical average and steady state probability of long-term observations of the specified objects, is good at describing population characteristics through statistical

induction, but poor in reflecting dynamically individual characteristics. Operation reliability can just make up the deficiency of the traditional reliability methodologies, and broaden the application range of reliability.

Operation reliability is also called real-time reliability or on-line reliability in the refs[1][2][3][4]. Although there are different names, all their duties are to evaluate the ability of the individual device performing its function under specified operating conditions, so that operating condition of the observed device can be dynamically grasped for safety in production, real-time maintenance, reducing material consumption and so on. In addition, there is also the similar thought that all these estimations are almost based on degradation data, and only the methods used are different. For example, Lu H et al[1] created a real-time reliability prediction model which is applicable to an individual product unit operating under dynamic conditions, by using time-series analysis techniques to extract performance degradation trends. Chinnam[2] provided an on-line reliability estimation model of individual components using degradation signals, and think that their degradation performance parameters can be described using polynomial regression model in application process. In fact, Kalbfleisch[5] pointed out the performance degradation data was the abundant information source for reliability estimation in the 1980s. Subsequently, many degradation modeling and corresponding reliability estimation methods have been put forward[6][7][8][9]. Currently, Nagi Z[10] presented a Bayesian updating method in which the real-time condition monitoring information was used to update the stochastic parameters of exponential degradation models. Xu[11] introduced a new real time reliability prediction method for dynamic systems which incorporated an on-line fault prediction algorithm. Zhao Zhao et al[12] created the real-time reliability model of the product by using the on-site measuring data through Bayesian method and the local updating ideas.

Generally, the device is thought of as failure when the key performance indicator of a device exceeds its set value (failure threshold). Therefore, the performance degradation data that are easy to measure directly can most reflect the reliability variety in operation. Of course, this is also the main reason why performance degradation data is often chosen as information source in the above-mentioned reliability estimation based on degradation data. But it is usually difficult or inconvenient to collect directly the performance degradation data sometimes. Some Feature signals that will monotonically vary with the performance degradation of device may be also selected as the information source of reliability estimation. For example, the change of the thrust force and torque in the drilling process was used as degradation signals to monitor the wear condition of the drilling bit and to predict the reliability of the drilling bit on line in the ref [13].

In this paper, degradation data is divided into two kinds of performance degradation data and feature degradation data. Performance degradation indicator (PDI) is the one that can directly identify the service ability of equipment, as the flank wear value of cutting tool. Feature degradation indicator (FDI), for example, the time-domain or frequency-domain indicators extracted form the vibration signals of equipment, can also reflect the operation status of equipment, but it can not be directly used to characterize of the service capacity of equipment. Generally, FDI are easier to acquire than PDI. Therefore, an estimation method of operation reliability is proposed to solve the above three difficulties by using FDIs of a variety of signals instead of PDI. In this paper, Gaussian process for machine learning (GPML) is used to treat the censored data, and in combination with distribution hypothesis, the Bayes' theorem is using as means of information fusion to acquire the instantaneous reliability model. The method has been validated by a CNC cutting tests. Ten cutting tools are used to train the model and two cutting tools are used to validate the model. The result shows that the instantaneous reliability and remained useful life are accurately obtained.

2. Operation reliability modeling

Suppose that there is a sample set of n observed-in-turn samples, denoted by $A=\{A_j \mid j=1,2,\cdots,n\}$. The PDI value of the sample A_j is denoted by $(p_{1j}, p_{2j},\cdots, p_{mj})$ at the moment $(t_{1j}, t_{2j},\cdots, t_{mj})$ respectively, the corresponding z-th FDI value of A_j is denoted by $(f_{1j}^z, f_{2j}^z,\cdots, f_{mj}^z)$ at the moment $(t_{1j}, t_{2j},\cdots, t_{mj})$ respectively, where z is equal to 1 or 2, because of only thinking about 2 degradation features in this paper. When the PDI of A_j reaches its failure threshold value p_g , A_j is referred to as failure. In the same time, A_j obviously arrive at its effective useful life tr_j too. Moreover, note that t_{mj}, p_{mj} is less than tr_j , p_g respectively. In other words, this is a censored test in which all the samples do not run to failure.

2.1 Modeling process

2.1.1 Degradation track and prediction

Because of the censored data, we try to look for a relationship between P_j ($P_j = (p_{1j}, p_{2j}, \cdots, p_{mj})$) and T_j ($T_j = (t_{1j}, t_{2j}, \cdots, t_{mj})$) through regression analysis, and then use this relationship to predict the time of P_j arriving at p_g as the pseudo failure life tp_j of A_j. In the same way, we also hope to find a relationship between F_j^z ($F_j^z = (f_{1j}^z, f_{2j}^z, \cdots, f_{mj}^z)$) and P_j, and correspondingly, the pseudo-life-feature values fp_j^z can be obtained easily.

The usual approach to making regression analysis in the reliability study is firstly to observe the trend of the variables, and then, to assume they follow a certain regression model such as the linear regression, polynomial regression and so on, at last, to obtain the regression equation through the least squares estimation. With the development of the artificial intelligence technology, some machine learning methods can better accomplish this process without manual intervention, for example, support vector machine (SVM)[14] and artificial neural network (ANN). In this paper, the GPML[15] [16] will be applied. It is not only because GPML itself is a common probabilistic type kernel learning machine, but also because it has fewer adjustable parameters and can better combine observed data with prior knowledge without manual intervention. The principle of GPML will be briefly described in 2.2

2.1.2 Distribution hypothesis

For small samples, distribution hypothesis is an effective approach to solving the lack of prior knowledge in practice.

Let $\{tp_j \mid j = 1,2,\cdots,n\}$ follows a random distribution with probability density function $\phi(t:\theta)$, and correspondingly, $\{fp_j^z \mid j = 1,2,\cdots,n\}$ follows a conditional distribution with conditional probability density function $h^z(x:\xi)$ too, where $z = 1,2$, θ and ξ are the parameter vectors to be estimated and. Next, their probability density functions $\phi(t)$, $h^z(x)$ with actual parameter are easy to be obtained by means of the maximum likelihood estimation method, respectively.

According to the definition of reliability, the reliability of an observed individual in any moment t can be calculated by the equation

$$R_t = p\{T > t\} = 1 - \int_0^t \phi(x)dx \tag{1}$$

In particular, considering weibull distribution, the reliability Eq. (1) can be expressed as

$$R_t = p\{T > t\} = 1 - \int_0^t \frac{k}{\lambda}\left(\frac{t}{\lambda}\right)^{k-1} e^{-\left(\frac{t}{\lambda}\right)^k} dt \tag{2}$$

where T is a time random variable, k is the shape parameter and λ is the scale parameter.

Next, let the corresponding feature indicator values of the observed individual be f^z in any moment t through measuring and computing. If all the feature indicators increase monotonically, the probability of the sample's feature indicators at present more than f^z can also be calculated by the equation:

$$R_z = p\{X^z > f^z \mid B\} = 1 - \int_0^{f^z} h^z(x)dx, \tag{3}$$

Considering normal distribution, the probability equation can be expressed as

$$R_z = p\{X^z > f^z \mid B\} = 1 - \int_0^{f^z} \frac{1}{\sigma_z\sqrt{2\pi}} \exp\left(-\frac{(x-\mu_z)^2}{2\sigma_z^2}\right)dx \tag{4}$$

where X_z is a random variable of feature indicator, B denotes the event of product working normally, μ_z is the expectation of the sample set $\{fp_j^z \mid j = 1,2,\cdots,n\}$, σ_z is the Standard Deviation of the sample set $\{fp_j^z \mid j = 1,2,\cdots,n\}$ and $z = 1,2$.

Of course, if decreasing monotonically, the equation of less than f_i^z is expressed as

$$R_z = p\left\{X^z \le f^z \mid B\right\} = \int_0^{f^z} h^z(x)dx \tag{5}$$

Specially, a presumption that the occurrence of the event $X^z > f^z$ is under the condition of the event B has been implied in the test, so Eq. (3) ~ (5) are shown in the form of conditional probability.

Owing to the similarity, the monotonic decrease will not be discussed below again.

In some sense, R_z may also be seen as a reliability estimation of the observed individual at the moment t, but the single sensor information is subject to stochastic impulse and often shows unsteadiness. Therefore, the Bayesian methods are employed to fuse the two-sensor information for estimating the operation reliability of individual as follows.

2.1.3 Reliability model

For some partition of the event space $\left\{B, \overline{B}\right\}$, let A_Z be independent and $A_z \ne 0$, $z = 1,2,\cdots$. Then, when all the events A_Z have occurred, the probability of the occurrence of the event B can be expressed as:

$$R(t) = P\left(B \mid \bigcap_z A_z\right) \tag{6}$$

Give every event to concrete signification with reference to the section 2.1.2: B denotes the normal operation of product, $\overline{B}$ is the complement set of B, A_Z express the event $X^z > f^z$. Provided that $A_z \mid \overline{B}$ and $\overline{A_z} \mid B$ are equiprobable, according to the Bayes' theorem, Eq. (6) can be rewritten as:

$$R(t) = \frac{R_t \prod_z R_z}{R_t \prod_z R_z + (1 - R_t)\sum_z (1 - R_z)} \tag{7}$$

Eq. (7) is the final reliability evaluation model. It implies a simple philosophy form the general to the especial. The general features are reflected through distribution hypothesis and parameter estimation. The inputs of the equation are the cumulative operating time and several FDI values at present. Finally, the instantaneous reliability is obtained by using the operating status information of the product at present.

If 50% is defined as the failure threshold of the instantaneous reliability, the failure time can be determined. Moreover, the remained useful life can be estimated at any moment by using GPML to predict the FDI values of the future time.

2.2 GPML[15] [16]

Let $D = \{x_n, y_n\}_{n=1}^N$ be a given data set, where $x_n \in R^d, y_n \in R$, and define input matrix $X \in R^{d \times N}$, output vector $Y \in R^{N \times 1}$. In a finite data collection of given D, $\{f(x_n) \mid n = 1,2,\cdots,N.\}$ can construct a random variable set, and follow joint Gaussian distribution. Random process $\{f(x_n) \mid n = 1,2,\cdots,N.\}$ is referred to as Gaussian process:

$$f(x) \sim GP(m(x), k(x, x')),$$

where $m(x) = E[f(x)]$, $k(x, x') = E[(f(x) - m(x))(f(x') - m(x'))]$, are called mean function and covariance function, respectively.

Let y be the observed target value. We consider the Bayesian analysis of the standard liner regression model with Gaussian noise:

$$y = f(x) + \varepsilon,$$

where the noise ε follows an independent, identically distributed Gaussian distribution with zero mean and variance σ_n^2:

$$\varepsilon \sim N\left(0, \sigma_n^2\right),$$

From above, we can know:

$$y \sim GP\left(m(x), k(x, x') + \sigma_n^2 \delta_{ij}\right),$$

where δij is the dirac function. When $i = j$, function $\delta_{ij} = 1$.

The covariance function as the matrix form can be expressed as a $N \times N$ covariance matrix:

$$C(X, X) = E\left(yy^T\right) = K(X, X) + \sigma_n^2 I$$

where I is a $N \times N$ unit matrix, $C(X, X)$ is the $N \times N$ covariance matrix, $K(X, X)$ denotes the $N \times N$ kernel function and also called Gram matrix.

If there are n training points and n_* test points, and let m and m_* be mean vectors of the training inputs and test inputs, respectively, and then we can obtain the joint distribution of the training output y and the test outputs f_*:

$$\begin{bmatrix} y \\ f_* \end{bmatrix} \sim N\left[\begin{bmatrix} m \\ m_* \end{bmatrix}, \begin{bmatrix} C(X, X) & K(X, X_*) \\ K(X, X_*) & K(X_*, X_*) \end{bmatrix}\right]$$

According to Bayesian analysis and the property of joint Gaussian distribution, we can obtain the posterior conditional distribution of the output vector f_*:

$$f_* \mid X, y, X_* \sim N\left(\overline{f}_*.\mathrm{cov}(f_*)\right)$$

$$\overline{f}_* = E(f_* \mid X, y, X_*) = m + K(X, X)C(X, X)^{-1}(y - m)$$

$$\mathrm{cov}(f_*) = K(X_*, X_*) - K(X_*, X)C^{-1}(X, X)K(X, X_*)$$

where prediction mean vector $\overline{f}_*$ is the output vector of GP regression model, and is also the prediction value of f_*.

If let $k(x_*) = \left(k(x_*, x_1), \cdots, k(x_*, x_N)\right)^T$ be the covariance vector of the test input and all the training inputs for a single test data x_*, we can obtain the observed output prediction value $\overline{f}(x_*)$ and its error band $\sigma_{\overline{f}}^2(x_*)$, which is respectively expressed as:

$$\overline{f}(x_*) = m(x_*) + k^T(x_*)C^{-1}(y - m(x)) \tag{8}$$

$$\sigma_{\overline{f}}^2(x_*) = k(x_*, x_*) - k^T(x_*)C^{-1}k(x_*). \tag{9}$$

3. Experiment and Estimation procedure

3.1 Experiment setup

In this section, we consider a tool wear experiment that was conducted on an NC lathe. The schematic diagram of the experimental setup is shown in Fig. 1. The cutting tool-used is a carbide tool in the test. Flank wear value V_B that is selected as the PDI of the cutting tool is measured by a micro-optical system with a CCD camera (model: MZDH0670), an adjustable circular-ring-mode LED light and a built-micrometer. The tool vibration signals are acquired by an accelerometer (model: PCB ICP352C34), a data acquisition system (model: LMS SCADAS305) and a portable computer. At the same time, the current signals of spindle motor and Z-servo motor and the acoustic emission (AE) signals are also measured by two hall current sensors (model: GAA-KY1) and an AE sensor (model: Kistler 8152B) respectively. Their installations are shown in Fig. 2.

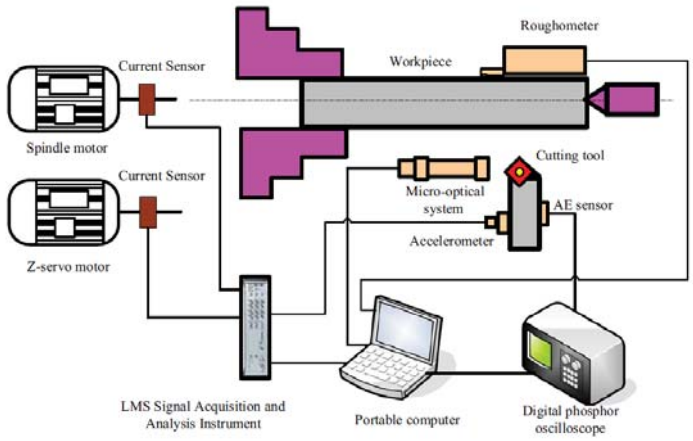

Fig. 1 The schematic diagram of the experimental setup

motor and the acoustic emission (AE) signals are also measured by two hall current sensors (model: GAA-KY1) and an AE sensor (model: Kistler 8152B) respectively. Their installations are shown in Fig. 2.

3.2 Estimation procedure

In this experiment, the wear data, vibration signals and current signals of 12 cutting tools were measured. The flank wear value V_B is select as the PDI of cutting tool in the machining process. If V_B is smaller than the threshold V_t, the cutting tool is considered as in the health state, otherwise, in the failure state. V_t is selected as 0.6 mm with reference to ISO3685 here. Accordingly, two FDIs, the WP energy of frequency band 7 (WE7) and the rate of main cutting force (RM) to feed cutting force, are respectively extracted from the vibration signals and the current signals. Next, V_B, cumulative operating time T, WE7 and RM are used as input variables to train the estimation model of operation reliability in section 2. Finally, the instantaneous reliability estimation and remained useful life prediction of individual can be carried out by using WE7 and RM as input, as shown in Fig. 3. For validating the effectiveness of the method, 10 cutting tools are employed to train model, and the remaining 2 ones to simulate estimating process in this paper.

4. Result and analysis

4.1 Feature extraction

4.1.1 Force ratio

Ref [17] has been shown analytically and experimentally that the ratio of feed forces to main cutting force is most indicative of the flank wear, and the proposed ratio is independent of the workpiece geometry. According to metal cutting theory, the main cutting power $P_z = F_z n_w r$, and the feed cutting power $P_x = F_x n_w f$, where F_z is the main cutting force, F_x is the feed force, n_w is the speed of main spindle, r is the radius of workpiece-machined and f is the feed rate. Therefore, the ratio of feed forces to main cutting force may be expressed as

$$\rho = \frac{F_x}{F_z} = \frac{I_x U_x r \cos\varphi_x}{I_z U_z f \cos\varphi_z} \tag{10}$$

where I_*, U_* and $\cos\varphi_*$ are the working current, working voltage and power factor of the corresponding motor, the symbol * represent x or z.

In Eq. (11), U_* and $\cos\varphi_*$ may be seen as constant related to the corresponding motor, and r and f are process variable that may be acquired from NC machining program conveniently. Therefore, Force ratio $\rho = \frac{F_x}{F_z}$ can be obtained through monitoring the change of motor current. As is shown in Fig. 6(a), force ratio ρ monotonically increases with V_B, it shows reasonable that ρ is selected as a FDI.

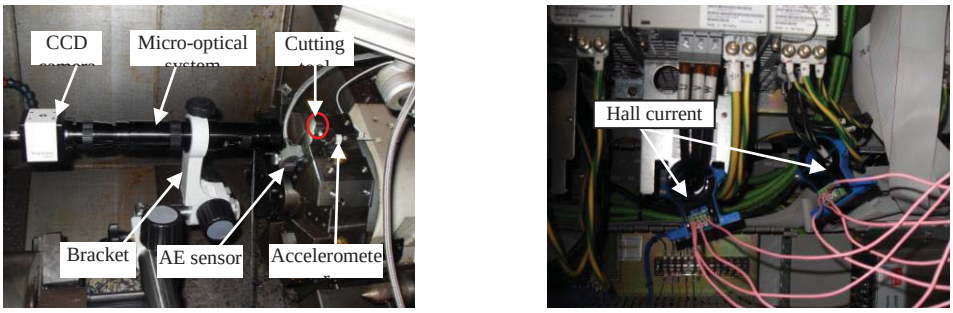

Fig. 2 The installation of micro-optical system, accelerometer, AE sensor and hall current sensors

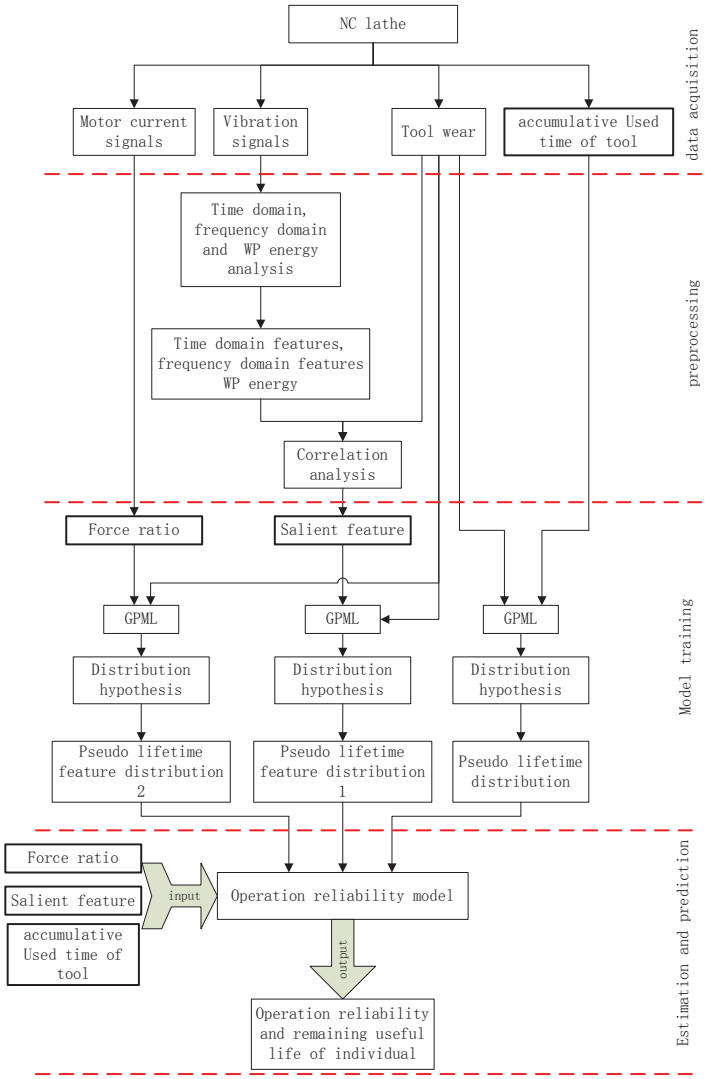

Fig. 3 flow chart of operation reliability estimation

4.1.2 WP energy of frequency band

Tool vibration is caused by a variety of factors, such as cutting force, built up edge, material inhomogeneity, ambient conditions and tool wear. Vibration analysis in this section aims at finding the FDI related to tool wear. In this experiment, the sampling frequency was 32768 Hz. The vibration signals are decomposed by WP transform in which Daubechies 10 is used as the mother wavelet. The WP band energy and entropy of each tool can be obtained. In refs [18], it was observed that the energy is mainly focused on two frequency bands of band 7 and band 9. Next, 11 time-domain features of band 7 and band 9 of every tool were respectively calculated as shown in table 1. Finally, the averaged correlation coefficients (ACCs) between WP band energy, entropy and 22 time-domain features and tool wear are calculated and displayed in Fig. 7(a). It can be observed that the

ACCs of bands 7, 9 are larger. Because WP energy of band 7 (WE7) increases monotonically as shown Fig. 6, it is selected as another FDI.

Table 1 The Feature parameters

$x_m = \frac{1}{N}\sum_{n=1}^{N} x(n)$	$x_p = \max\lvert x(n)\rvert$	$x_{ra} = \left(\frac{1}{N}\sum_{n=1}^{N}\sqrt{\lvert x(n)\rvert}\right)^2$	$x_{rms} = \sqrt{\frac{1}{N}\sum_{n=1}^{N}(x(n))^2}$
$x_{std} = \sqrt{\frac{\sum_{n=1}^{N}(x(n)-x_m)^2}{N-1}}$	$x_{ske} = \frac{\sum_{n=1}^{N}(x(n)-x_m)^3}{(N-1)x_{std}^3}$	$x_k = \frac{\sum_{n=1}^{N}(x(n)-x_m)^4}{(N-1)x_{std}^4}$	$x_c = \frac{x_p}{x_{rms}}$
$x_{ma} = \frac{x_p}{x_{ra}}$	$x_{sha} = \frac{x_{rms}}{x_m}$	$x_i = \frac{x_p}{x_m}$	

where $x(n)$ is a signal series for $n = 1, 2, \cdots, N$; N is the number of data points.

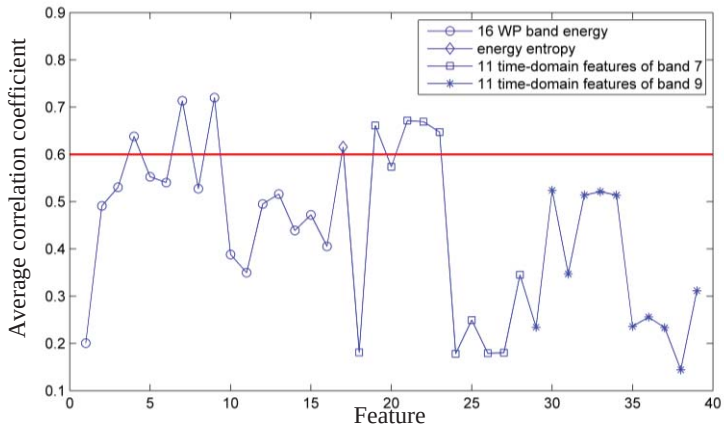

Fig. 4 The ACCs between WP energy, entropy, time-domain features and tool wear

4.2 GPML regression and prediction

Performance degradation data (tool wear) and two group of Performance degradation data (force ratio and WE7) of 10 cutting tools have been acquired through measuring and transforming. The changes of tool wear with accumulative useful time (AUT), force ratio with tool wear and WE7 with tool wear are respectively displayed in Fig. 5(a), 6(a) and 7(a), in which all 10 tool wear are not arrived at the failure threshold 0.6 mm. In order to know the failure life and the two FDI values in failure, the regression is made by means of GPML as shown in Fig. 5(b), 6(b) and 7(b). When tool wear arrive at 0.6 mm, three sets of predictive values, called pseudo failure life, pseudo failure force ratio and pseudo failure WE7 respectively, are obtained.

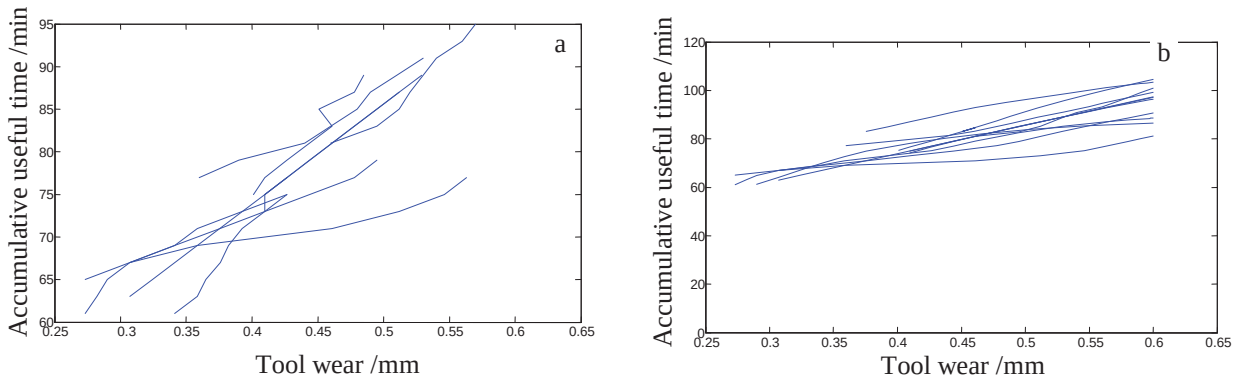

(a) Actual curve, (b) Regression and prediction curve using GPML
Fig. 5 The relationship between AUT and tool wear

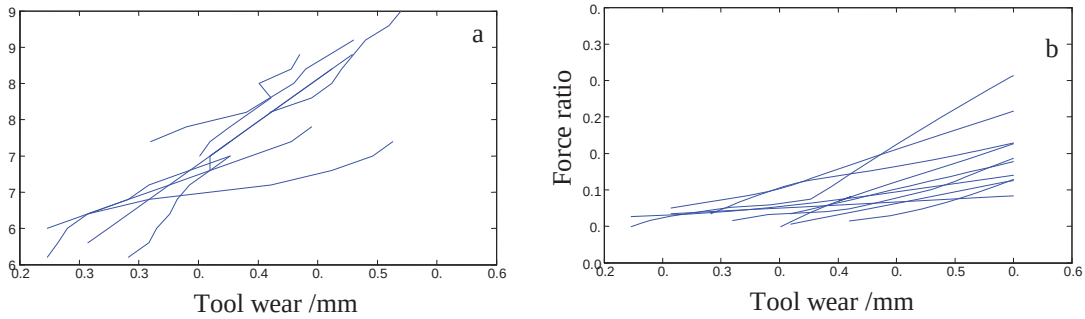

(a) Actual curve, (b) Regression and prediction curve using GPML
Fig. 6 The relationship between force ratio and tool wear

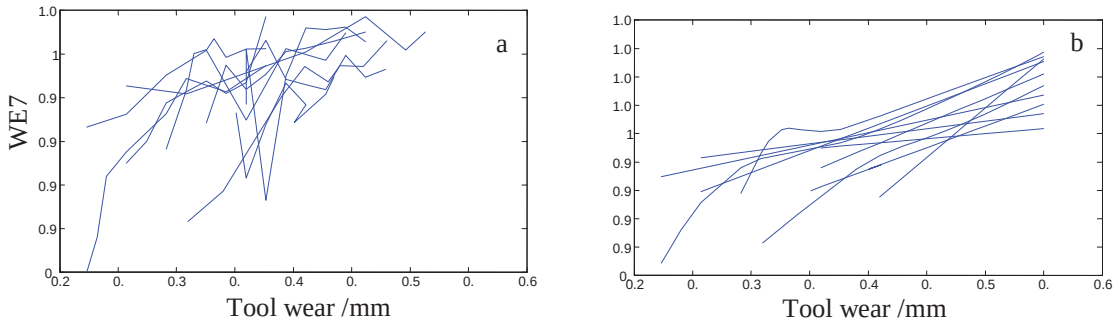

(a) Actual curve, (b) Regression and prediction curve using GPML
Fig. 7 The relationship between WE7 and tool wear

4.3 Distribution hypothesis and estimation model

Provided that pseudo failure life follows weibull distribution, pseudo failure force ratio and pseudo failure WE7 follow normal distribution with different parameters respectively. Using the maximum likelihood estimation methods, the parameters of Eq. (2) (4) can be calculated to λ =96.7, k =13.8, μ_1 =0.1989, σ_1 =0.0477, μ_2 =1.0241 and σ_2 =0.02. The probability density function is depicted as Fig. 7 and the hypothesis testing are made as shown in Fig. 8. It is observed that they nearly distribute on a line, respectively. Therefore, it can be thought that distribution hypotheses are satisfactory overall.

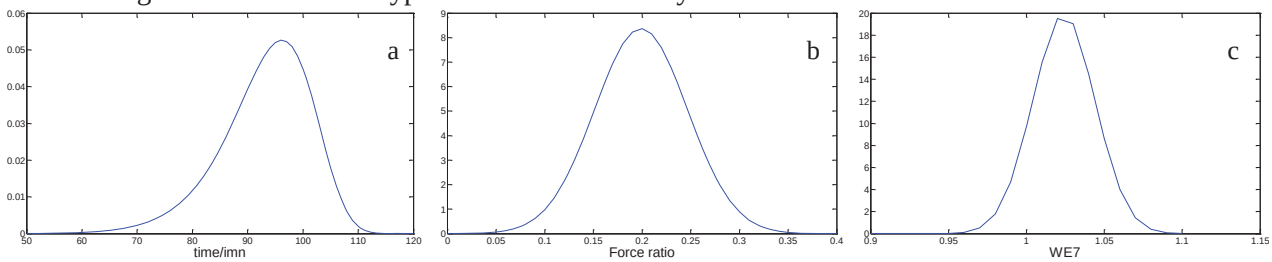

(a) Pseudo failure life, (b) Pseudo failure force ratio | normal working, (c) Pseudo failure WE7 | normal working

Fig. 8 Probability density distribution

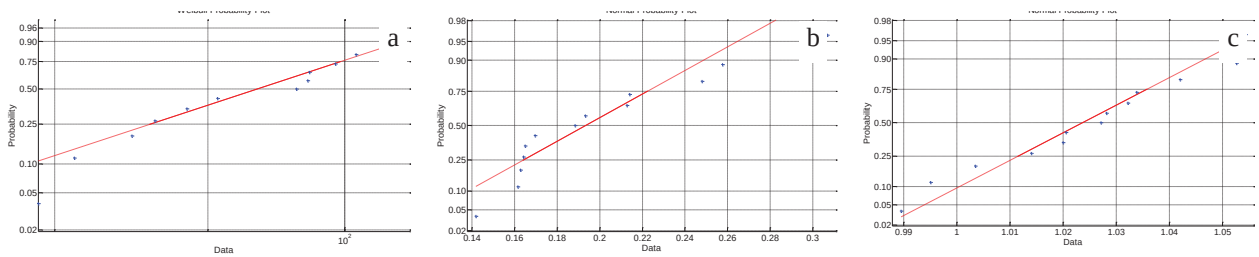

(a) Pseudo failure life, (b) Pseudo failure force ratio | normal working, (c) Pseudo failure WE7 | normal working

Fig. 9 Hypothesis testing

According to the above analysis, the reliability estimation model at the moment t can be expressed as:

$$R(t)=\frac{R_pR_1R_2}{R_pR_1R_2+(1-R_p)(1-R_1)(1-R_2)} \tag{11}$$

where $R_p=1-\int_0^{t_i}\frac{13.8}{96.7}\left(\frac{t}{96.7}\right)^{12.8}e^{-\left(\frac{t}{96.7}\right)^{13.8}}dt$, $R_1=1-\int_0^{f_i^1}\frac{1}{0.0477\sqrt{2\pi}}\exp\left(-\frac{(x-0.1989)^2}{2\times0.0477^2}\right)dx$,

$R_2=1-\int_0^{f_i^2}\frac{1}{0.02\sqrt{2\pi}}\exp\left(-\frac{(x-1.0241)^2}{2\times0.02^2}\right)dx$.

4.4 Reliability estimation

In order to identify the validity of the proposed model, the force ratio f_t^1 and WE7 f_t^2 of tool NO 11 and 12 at the moment t are input into Eq. (11) to calculate the reliability as shown in Fig. 9. If the instantaneous reliability arrives at 0.5, the cutting tool is thought to be invalid. The estimated life of tool NO 11 and 12 is about 90 and 96 min, respectively. However, the real measured failure time is 91 and 99 min, respectively. The estimated errors are 1% and 3%.

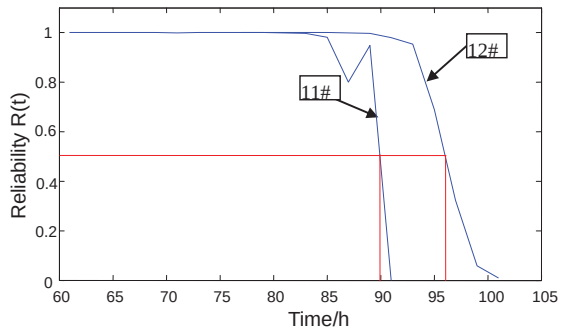

Fig. 10 the estimated reliability of tool NO 11 and 12

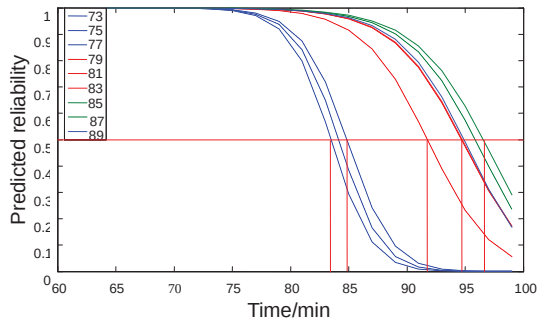

Fig. 11 the predicted life of tool NO 12

4.5 Life prediction

When the two feature indicator values (f_t^1 and f_t^2) at the moment t is input into Eq. (11), the reliability estimation at the moment t is carried out. In addition, if the two FDI values are predicted by using the GPML at a future moment $ti+\Delta t, ti+2\Delta t,\cdots,ti+n\cdot\Delta t$, and then the predicted FDI valves is also input into Eq. (11) respectively, the tool life may be predicted in real time. The predicted instantaneous reliability of tool NO 12 at the moment t =73, 75 …, 89 min is shown in Fig. 11, where $\Delta t=2\,\text{min}$. The predicted life and error in the different moments are shown in Table 2.

Table 2 Predicted life and prediction error of tool NO 12

Starting time of prediction	73	75	77	79	81	83	85	87	89
Predicted life	84.5	83.5	84.9	91.8	94.6	94.8	96.8	96.1	95
Prediction error	14.6%	15.7%	14.2%	7.3%	4.4%	4.2%	2.2%	2.9%	4.0%

5. Conclusion

In the paper, an estimation method of operation reliability for NC cutting tools is proposed under the condition of small samples and censored data. The approach can carry out the real-time reliability estimation and life prediction on line by means of operating status information of device.

The advantages of this approach are:

(1) Only small samples without run-to-failure can be employed to train the estimation model;

(2) Once the model training has been done, the reliability and life prediction of the same observed individual as samples in a certain moment can be automatically calculated on line, without manual intervention.

The further studies need to be made: As shown in Fig. 6(a), the selected feature indicator WE7 has an overall increasing trend, but several curves show bigger in vibration amplitude. Therefore, it is necessary to search out the better degradation feature indicator.

Acknowledgements

This research is supported financially by the key project of National Natural Science Foundation of China (no 51035007), National Natural Science Foundation of China (no 50975220), National Basic Research Program of China (no 2009CB724405), Important National Science and Technology Specific Projects (no 2010ZX04014-016) and the Specialized Research Fund for the Doctoral Program of Higher Education (no 20110201130001).

References

[1] Lu H, Kolarik W J and Lu S S. Real-time Performance Reliability Prediction, *IEEE Transaction on Reliability*, Vol. 50, pp. 353-357, 2001.

[2] R.B. Chinnam. On-Line Reliability Estimation of Individual Components, Using Degradation Signals, *IEEE Transaction on Reliability*, Vol. 48, No. 4 , 1999.

[3] G. X Zheng, D. J Yin and H. Z Dong. Real-Time Reliability Prediction for a Dynamic System Based on the Hidden Degradation Process Identification, *IEEE Transactions on Reliability*, 2008, Vol. 57, No.2, pp. 230-242.

[4] Jianye Ching and Yi-Hung Hsieh. Updating Real-Time Reliability Of Instrumented Systems with Stochastic Simulation, *Probabilistic Engineering Mechanics*, Vol. 24, pp. 242-250, 2009.

[5] J. D. Kalbfleisch and J. F. Lawless. Estimation of Reliability in Field Performance Studies. *Technometrics*, Vol. 30,No. 4, pp. 365-370,1988.

[6] Lu C.J. and Meeker W.Q.. Using Degradation Measures to Estimate a Time-To-Failure Distribution, *Technometrics*, Vol. 35, No. 2, 161-173, 1993.

[7] Crk V. Component And System Reliability Assessment from Degradation Data, *Doctor of Philosophy: The University of Arizona*, 1998.

[8] Jayaram J.S.R. and Girish T. Reliability Prediction Through Degradation Data Modeling Using a Quasi-Likelihood *Approach. Proceedings of the Annual Reliability and Maintainability Symposium*, pp. 193-199, 2005, Alexandria ,USA.

[9] Di Xu and Wenbiao Zhao. Reliability Prediction Using Multivariate Degradation Data, *Proceedings of the Annual Reliability and Maintainability Symposium*, pp. 337-341, 2005, California,USA.

[10] Gebreel N.Z, Lawley M.A,etc. Residual Life Distributions from Component Degradation Signals: A Bayesian Approach, *IIE Transactions*, Vol. 37, No. 6, pp. 543-557, 2005.

[11] Z. G Xu, Y. D Ji, D. H Zhou. A New Real-Time Reliability Prediction Method For Dynamic Systems Based On On-Line Fault Prediction, *IEEE Transactions on Reliability*, Vol. 58, No. 3, pp. 523-538, 2009.

[12] Z. Zhao and D. D Dong. Read Time Reliability Evaluation for Degradation Failure Product Based on Bayes Method, *Journal of National University of Defense Technology*, Vol. 29,No.6, pp. 116-120, 2007.

[13] R. B. Chinnam and Bharatendra Rai. *Intelligence in Reliability Monitoring*, Springer, 2007

[14] Achmad Widodo and Bo-Suk Yang. Support Vector Machine in Machine Condition Monitoring and Fault Diagnosis, *Mechanical Systems and Signal Processing*, pp.2560-2574, 2007.

[15] Seeger M. Gaussian Processes for Machine Learning, *International Journal of Neural System*, Vol. 14, No.2, pp. 69-106, 2004.

[16] Rasmussen C E and Williams C K I. Gaussian Processes for Machine Learning, *Cambridge, MA: The MIT Press*, 2006.

[17] Qiang Liu, Yusuf Altintas. On-Line Monitoring Of Flank Wear in Turning with Multilayered Feed-Forward Neural Network, *International Journal of Machine Tools & Manufacture*,Vol. 39, pp. 1945-1959,1999.

[18] B Chen, X Chen, B Li, Z He, H Cao and G Cai. Reliability Estimation for Cutting Tools Based on Logistic Regression Model Using Vibration Signals, *Mechanical Systems and Signal Processing*, Vol. 25, No. 7, pp. 2526-2537, 2011.

Copyright © 2012 DET Corp., Japan All Rights Reserved
International Journal of Comprehensive Engineering
Part A, 2(2), 117-124, 2013
Doi: 10.14270/IJCE2013.2.2.a117
Regular paper

ISSN 2186-2680
e-ISSN 2186-2656
www.iace-journal.org

An Improved Detector Generation Method based on Artificial Immunity

Xinpeng Zhang [1, #], Niaoqing Hu [2] and Lei Hu [3]

Laboratory of Science and Technology on Integrated Logistics Support, National University of Defense Technology, Changsha, 410073, China

zhang_xinpeng@126.com, Tel.: +86-136-7739-4941; 2. hnq@nudt.edu.cn; 3. lake_hl@hotmail.com

Abstract: There are mainly two ways to define detector radius in artificial immune real-valued negative selection algorithm: one is the detector generation algorithm with fixed radius and the other one is with variable radius. The former method is simple, but tends to be restricted by the efficiency problem caused by small radius and the uncovered space problem caused by big radius. Meantime, the overlaps between different detector space make against classifying of different fault patterns; the latter method is able to make up some disadvantages of the fixed radius method to a certain extent, but if let the radius change freely, it will be probable to bring on another problem that the coverage rate of the detector generated randomly satisfies the demand, but the number of the detectors is small and the radius is large. In this situation, although the abnormal states different from the normal states can be checked out, it is hard to distinguish the specific type of fault. This paper presents a new detector generation method based on both of the methods mentioned above, takes coverage rate to the state space and detection efficiency into account. The whole space corresponding to the abnormal states is divided into several different regions according to the distance with the self space; the detector has a same radius in every region while the radiuses are different between regions. Meanwhile, the size of the overlapped detector space can be controlled here. A comparison with the current detector generation ways is also included in this paper.

Keywords: Artificial Immunity, Detector Generation, Overlapped Space, Fault Diagnosis.

Received: May 25,2012 / Accepted: Feb. 20,2013 / Published: Jul. 5,2013

1. Introduction

Artificial immunity, as a simulation to biological immune system, attracts more and more attention by scholars because of its excellent performance in many areas in recent years. Artificial immunity has been used to resolve different engineering problems. Japanese scholar Ishida diagnosed sensor network failure, which is the earliest research achievement can be referred of artificial immunity [1]. Then, in 1994, American scholar Forrest applied negative selection algorithm (NSA) of biological immune system to the computer security and virus examination [2]. Doctor Dasgupta of Missouri University focuses on the research of algorithm based on immune mechanism and application of artificial immune, mainly include: computer anomaly detection [3], pattern recognition [4], immune intelligent [5] and other related applications [6]. Doctor Timmis of British Kent University mainly studies data mining and data clustering based on immune mechanism such as immune network, clonal vaviation, affinity maturation and immune diversity and so on [7,8]. Beyond that, some researchers from Belgium, Poland, Russian, and China and so on are also studying the artificial immune theory and applications. There is a short time that artificial immune developed, so its own theory system has not been formed, and the theory and applying research based on immune mechanism are now enriching and perfecting the artificial immune system theory continually. Inspired by the self to non self recognition mechanism of biological immune system, Forrest and his colleagues proposed negative selection algorithm (NSA) to detect a variety of changes [2]. There are mainly two algorithms: encoding negative selection algorithm and real-valued negative selection algorithm [9]. Recently, real-valued negative selection algorithm generates detectors based on two methods as fixed radius and variable radius [10], both of which has their deficiencies. This paper presents a new detector

generation method based on multi-level radius in allusion to the disadvantages of the two existing methods mentioned above in order to achieve fault diagnosis effectively.

2. Negative Selection Mechanism

There are mainly two types of lymphocytes segmented into B and T in biological immune system, both of them are stem cells produced in the marrow, distributed in the whole body, and play an important role in the immune system. T cells produced in the marrow need to be sent into thymus and checked. Firstly, progenitor T cells are produced in the marrows and then develop into T precursor cells in thymus. Each precursor T cell wanted to be upgraded into adult T cell must be checked by the MHC (Major Histocompatibility Complex) which related to the genetic factor. The mechanism of negative selection is as follows(as shown in Fig.1): When the detectors existed in the surface of immature T cells can identify the MHC molecules and their own antigen fragments (also known as peptide) complexes, the immature T cell apoptosis occurs, viz, the immature T cells responded to their own organizations will be apoptotic; and those immature T cells, who cannot recognize MHC molecules and self-antigen fragment complex will survive, proliferate and complete the selection and maturation process to T cells. After negative selection, T cells' detectors can accurately identify the non-self elements, and

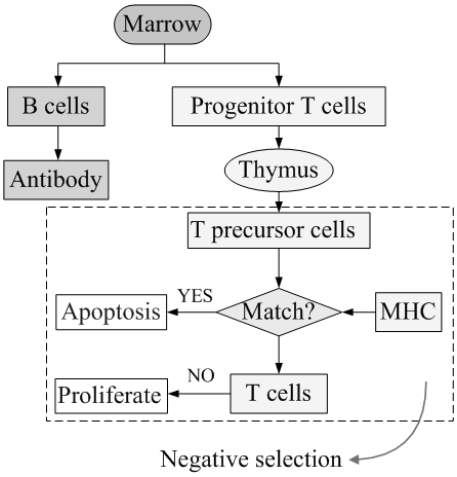

Fig. 1 Negative Selection Mechanism of Biological Immunity

this process is known as self to non-self recognition of the immune system [11].

Artificial immune system negative selection algorithm imitates biological immune system, it first generates a large number of random samples, then checks each sample of the normal data set whether it matches with the random sample, removes the one who matches with the normal sample data, and the samples incompatible with any normal sample data are reserved [12], so that the random samples reserved finally will further constitute the candidate detector set. When the test data is identified by any one detector in candidate detectors, then the corresponding state can be judged as abnormal state. If specific fault data can be collected, candidate detectors generated can be trained to mature detectors corresponding to a variety of fault states, and then we can use these mature detectors to achieve fault pattern recognition.

3. Two Negative Selection Algorithms

3.1 Encoding Negative Selection Algorithm

The negative selection algorithm proposed by Forrest use binary encoding firstly to represent self state and detectors, which is used in virus detection of computer system successfully. The method of binary encoding uses binary strings to represent detectors and self-body samples. Detectors are some simple, fixed-length binary strings. Two binary strings are compared using a simple matching rule to determine whether they are matched or not. If the binary string of detector generated matches with binary string of self-body samples representing normal state, then this detector will be removed. Only the detectors which are not matched with self-body can be retained. The matching rules can be divided into two types: matching completely and matching partially. If the two strings with equal length have the same value in every same position, then the two strings are matching completely. However, partial matching, which has many different matching rules such as Hamming rules and continuous r-bit matching rules, is more common. Hamming rules usually set a threshold value to determine whether the two binary strings match or not: When the Hamming distance between two strings is larger than the threshold value, then the two strings are defined as matching, otherwise, they will be considered not matching;

continuous r-bit matching rules determines whether two binary strings match or not by counting the number of continuous matching bits of the two strings: When the number of continuous matching bits is larger than r value, then they are matched. Otherwise, they are not matched.

Although encoding negative selection algorithm has been applied in many fields such as computer virus detection successfully, it still has many deficiencies: the method is difficult to represent complex detection space [13]; binary coded detectors and the continuous r-bit matching rules lack physical meaning in practice, and the ability of knowledge representation is poor; data dimension is low, and it is difficult to achieve data fusion with other high-dimensional algorithms; lack of ambiguity and robustness, its antinoise ability is poor and so on.

3.2 Real-valued Negative Selection Algorithm

Aiming at the deficiency of encoding negative selection algorithm, Dasgupta proposed real-valued negative selection algorithm [12] and applied it to fault detection of aircraft successfully. Different from the encoding negative selection algorithm, this method has such characteristics as follows:

1) Detection space representation: the self and non-self detection space expressed by a number of status indicators are normalized to an hyperrectangle space $[0,1]^n$, n represents the size of space dimension. Real-valued negative selection algorithm is operated in this normalized hypercube space.
2) Detectors and self-body representation: each detector *d* has a central point and a non-self recognition radius. Each self-body element *s* also has a central point and self-body radius. Self-body radius is introduced for the sake of taking the element close to the self-body center as self-body element. When testing, if the Euclidean distance between the element detected and detector is less than the non-self recognition radius of detector, then this element is deemed to be abnormal data. Detector is defined as follows: $d=(c,r_d)$, *c* is n-dimensional point and $c=(c_0, c_1, \cdots, c_{n-1})$, *d* represents an hypersphere whose center point value is c and radius value is r_d (this is to say, each detector is composed of a center and a radius). Be similar with the detector, each self-body element includes an n-dimensional center, the parameter r_s represents the threshold of self-body samples (allowed radius), and each sample point whose distance with the self-body sample center is larger than the threshold is considered as abnormal sample.
3) Matching rules: When the distance between test sample and detector center or self-body center is less than their radius, then the matching between test sample and detector or self-body occurs. The distance between two points uses Euclidean distance.

4. Two Typical Detector Generation Methods

It can be seen from the theory of real-valued negative selection algorithm mentioned above that the detector radius will directly affect the size of the detection space and thereby affect the test results to abnormal state. The common detector generation method currently can be divided into detector generation method with fixed radius and with variable radius [13] according to whether the radius can be changed or not.

Detectors with fixed radius get the same radius when detectors are generated using real-valued negative selection algorithm. Fig. 2 shows the coverage status of fixed radius detectors and self-body to the two-dimensional rectangular space. The space covered by black circle indicates self-body space corresponding to normal state; white circles are detectors, the space covered by them represents non-self space corresponding to the abnormal state. The regions not covered by detectors or self-body space are known as holes. It can be observed that if we want to achieve high coverage rate to the abnormal state using detectors with fixed radius, then we should reduce the detector radius to compress the holes space on one hand, on the other hand, more detectors should be generated. However, this will result in the problem that the number of detectors is huge and more overlapped space will appear, in this case, the detection efficiency to abnormal state will greatly decline.

To solve the problem mentioned above, a new detector generation method based on variable radius was proposed by Zhou Ji [14]. As shown in Fig. 3, the main idea of variable radius detector generation method is that each detector gets different radius according to its position in the space. The detector radius in negative selection algorithm based on variable radius needs to be calculated, and the calculation process is: If the point generated randomly is covered neither by existing detectors space nor by self-body space, then we get an effective detector, and its radius is the value subtracting the self-body radius r_s from the distance between the detector and the nearest self-body sample from it. It can be seen that on this condition we can get high coverage rate to the non self space only using a few detectors and save memory space for detectors. Meanwhile, the holes will be covered more easily. However, some detectors will get larger radiuses and then cover greater non-self space probably, which is detrimental to the training of detectors because the state corresponding to large radius detector is likely to be classified as two or more failure modes simultaneously, which makes the failure mode identification difficult and results in disabled detectors.

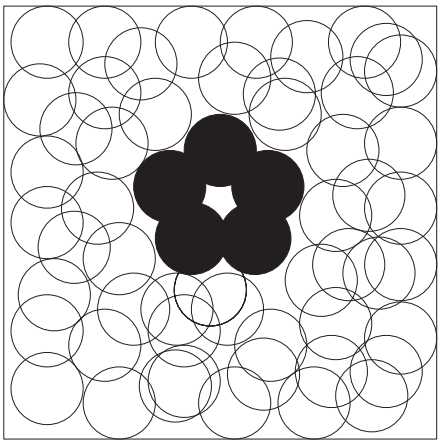

Fig. 2 The coverage status of detectors with fixed radius and self-body to the whole space

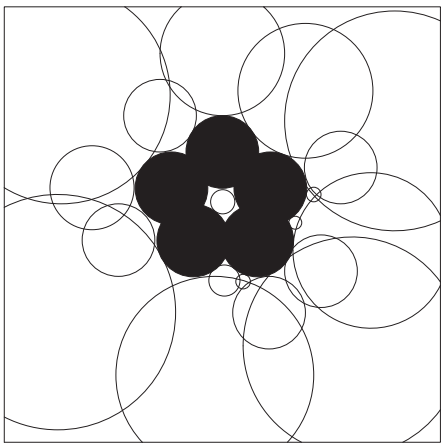

Fig. 3 The coverage status of detectors with variable radius and self-body to the whole space

5. Detector Generation Method based on Multi-level Radius

It can be seen from the analysis and comparison to the two detectors generation method mentioned above that fixed radius detector generation method is simple, but easy to be restricted by the efficiency problem caused by small radius and the uncovered space problem caused by big radius; variable radius detector generation method is able to make up some disadvantages of fixed radius method to a certain extent, but if we let the radius change freely, it will be probable to bring on a problem that the coverage rate of the detector generated randomly satisfies the demand, but the number of the detectors is small and the radius is large. If the number of detectors is initialized, then it will be easily happened that the space is covered by many detectors. In this situation, although the abnormal states different from the normal states can be checked out, it is hard to distinguish the specific type of fault. Considering the analysis above, we propose a new detector generation method based on multi-level radius.

5.1 Basic principle

The basic idea of multi-level radius detector generation method is: non-self space is divided into several different regions according to their distance with self-body space. The detectors in same region get the same radius and the radius is different between regions, as shown in Fig. 4. Then we can choose the detector radius of different regions flexibly according to different kinds of applications. For example, when normal and abnormal states vary greatly, but the distinction between different faults is not obvious, the emphases will be on the classification of specific fault types, then we can set a larger detector radius in the region close to the self space, and distant regions will be the areas where the fault appears in all probability, in this situation ,the radius of detector can be set smaller; by contraries, when detection to the abnormal state became the keystone, then we can set a smaller detector radius in the region close to the self space and set a larger detector radius in more distant area.

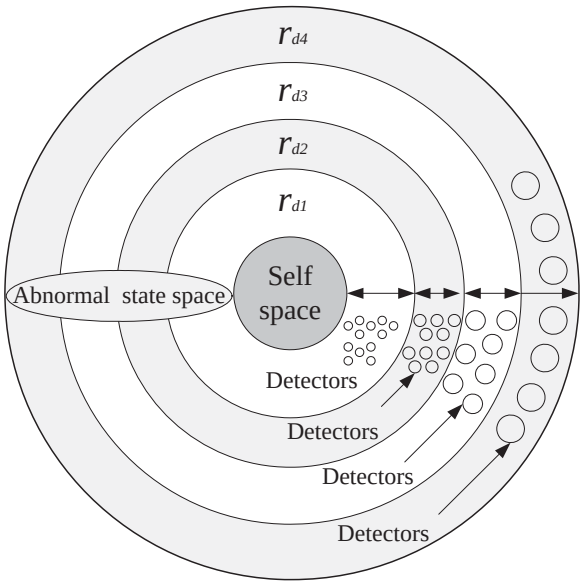

Fig. 4 The detector generation method based on multi-level radius

Meanwhile, the overlap rate between detectors is restricted and a threshold l_0 is set here. The parameter l is introduced to reflect the overlap rate between each new detector and the nearest existing detector from it as in Eq. (1):

$$l = \frac{r_1 + r_2 - d}{\min\{r_1, r_2\}} \tag{1}$$

r_1, r_2 represent radius of the new generated detector and radius of the nearest existing detector from it respectively, d represents the distance between the two detectors above, the value of min{ r_1, r_2} is equal to the smaller one of the two radii above. The value of l_0 and l are compared here: if l is greater than l_0, then the new generated detector will be discarded and the new detector can be reserved only when l is less than l_0. The generation process of detector with multi-level radius is as follows:

1) Define the self-body radius r_s, expected coverage rate co and threshold l_0. Divide non self space into several regions and set the radius r_{di} for each region(the number of regions is always around 5);
2) Generate normalized center sample of the detector randomly;
3) Determine whether the sample generated is covered by self- body space: if covered, this new detector should be discarded and return to step 2), and if not, then execute the next step;
4) Determine the location of new sample in non self space and then get the corresponding detector radius r_1;
5) Determine whether there has existing detectors in non self space: if there is, go to next step, otherwise, execute $r_2 = r_1$ and return to step 2);
6) Calculate the distance d between new detector and the nearest existing detector (radius: r_2) from it. Calculate the value of l and compare l and l_0: if l is less than l_0, then this new detector is reserved; otherwise, discard this new detector and return to step 2);
7) Calculate the coverage rate to the space cr. if cr is less than co, return to step 2), otherwise, go to next step;
8) The end.

Fig. 5 shows the comparisons of three detector generation methods after setting relevant parameters: fixed radius detectors (a), variable-radius detectors (b) and multi-level radius detectors (c). The regions covered by smaller red circles are corresponding to normal state; the blue circles represent initial detectors.

The relevant parameters of Fig. 5 are set as follows:

(a) Fixed radius detectors: detector number is set as 500, self-body radius r_s= 0.03, detector radius r_d= 0.06, then the coverage rate to space would be 99%
(b) Variable radius detectors: the coverage rate to space is set as 99%, self-body radius r_s= 0.03, then the number of detectors generated would be 9
(c) Multi-level radius detectors: the coverage rate to space is set as 99%, self-body radius r_s= 0.03, l = 0.5, then the number of detectors generated would be 84

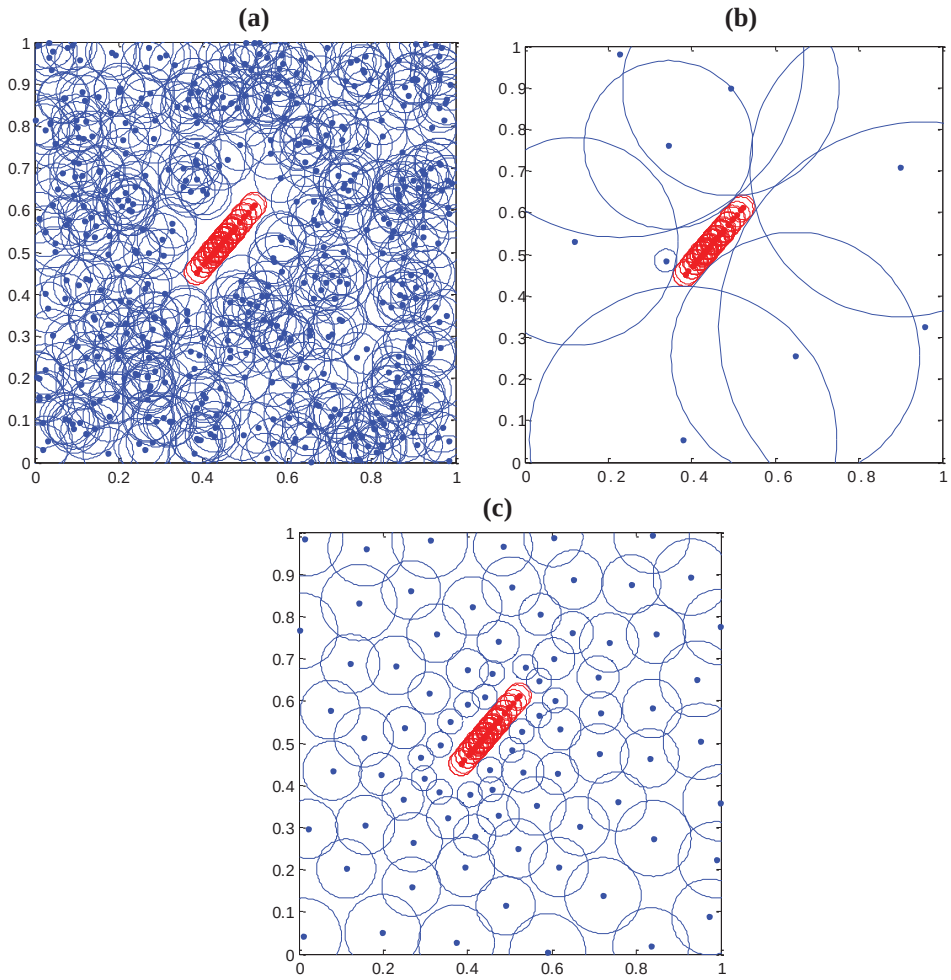

Fig. 5 Comparisons of Three Detector Generation Methods. (a) Detectors with fixed radius. (b) Detectors with variable radius. (c) Detectors with multi-level radius.

5.2 Experimental test

It can be shown from Fig. 5 (a) and (b) that the overlap rate of fixed radius detectors and variable radius detectors would be too high. Meanwhile, when the coverage rate to space is set, the number of fixed radius detectors generated would be large, while the number of variable radius detectors generated would be small, which is detrimental to identification of specific fault types. Multi-level radius detectors could make up this deficiency effectively. It can be seen from the comparison in Fig. 5 that the detector generation method based on multi-level radius has advantages that the detector number is moderate and the overlap rate can be controlled when the coverage rate to space has been set in advance. Then we will apply this method to detect and identify the bearing fault in inner ring and outer ring to verify effectiveness of the method proposed here, meanwhile, compared with the results using the other two methods (all three methods have the same parameters: coverage rate is 99% and self-body radius r_s= 0.03). Three types of samples which are normal state, inner ring fault and outer ring fault are collected and divided into two groups: one is for the training of mature detectors and the other is for testing.

We can get initial detectors using detector generation method based on the three methods mentioned earlier (as shown in Fig. 5), then we use collected samples of inner ring fault and outer ring fault in experiment to train initial detectors into mature detectors. After that, we can get mature detectors corresponding to inner ring fault and outer ring fault separately. There are 150 groups of test data(each group has 20,000 points), including 54 groups of normal state data, 48 groups of inner ring fault date and 48 groups of outer ring fault data. The test results are shown in Table 1, from which we can see that the detectors using the method proposed in this paper can identify outer ring fault excellently and the recognition rate can reach 100%, higher than using the other two methods , meanwhile, the recognition rate to inner ring fault can also be 85.4%, which is also higher than using the other two methods, and the 7 groups of test data which are not detected correctly using the new method are classified as unknown fault types data distinguished from the normal state samples. Because of using the same

normal state data, the three methods have the same detection rate to normal state. Besides the detection rate using proposed method is a little higher than using the other two methods, the new method has a higher detection effectiveness because it has a proper detector number, not too large than method (a) and not too small than method (b).

Table 1 Test results of the fault diagnosis

Bearing condition	Methods	Detector number	Test data number	Detection number	Detection rate
Normal state	a	54	54	54	100%
	b	54		54	100%
	c	54		54	100%
Inner ring fault	a	98	48	39	81.3%
	b	5		38	79.2%
	c	19		41	85.4%
Outer ring fault	a	69	48	46	95.8%
	b	2		43	89.6
	c	5		48	100%

(a) Detectors with fixed radius. (b) Detectors with variable radius. (c) Detectors with multi-level radius.

6. Conclusions

The two common types of detector generation method based on artificial immune negative selection algorithm are described in this paper and the advantages and disadvantages of the two methods above are also analyzed. Based on the knowledge mentioned above, a new detector generation method based on multi-level radius is proposed here. From the comparison of existing detector generation method and multi-level radius detector generation method we can get that the new method proposed in this paper has the advantages of both existing methods above, meanwhile, the number of detectors generated is moderate and the overlap rate of detectors can be controlled. According to test results of this method to bearing inner ring fault and outer ring fault we can see that the new method can perform excellently in fault detection and identification, and the effectiveness and practicality of the method is also validated.

Acknowledgment

The authors gratefully acknowledge financial support of National Natural Science Foundation of China (Grant No. 50905183)

References

[1] Y Ishida and E Mizessyn. Learning Algorithms on an Immune Network Model : Application to Sensor Diagnosis, *Proceedings of the Intemational Conference on Neural Networks*, Vol. 1, pp. 33-38, 1992, China.

[2] S. Forrest, A. S. Perelson and L. Allen. Self-Nonself Discrimination in a Computer, *Proceedings of the IEEE Symposium on Research in Security and Privacy*, pp. 202-212, 1994, Okaland.

[3] D. Dasgupta and F. Nine. A Comparison of Negative and Positive Selection Algorithm in Novel Pattern Detection, *Proceedings of the IEEE International Conference on Systems, Man and Cybernetics*, pp. 8-11, 2000, Nashville.

[4] D. Desgupta and Y. Cao. An Immunogenetic Approach to Spectra Recognition, *Proceedings of the Intemational Conference on Genetic and Evolutionary Computation*, pp. 13-17, 1999.

[5] O. Nasaroui, D. Dasgupta and F.Gonzalez. The Fuzzy Artificial Immune System：Motivations, Basic Concepts and Application to Clustering and Web Profiling. *Proceedings of the IEEE International Conference on Fuzzy System*, pp. 711-716, 2002.

[6] D. Dasgupta and S. Forrest. Artificial Immune Systems in Industrial Applications, *Proceedings of the International Confefence on IPMM*, pp. 10-15, 1999.

[7] J. Timmis and M. Neal. A Resource Limited Artificial Immune System for Data Analysis, *Knowledge Based Systems*, Vol.14(3-4), pp. 121-130, 200l.

[8] J. Timmis and M. Neal. Investigating the Evolution and Stability of a Resource Limited Artificial Immune Systern, *Proceeding of GECCO*, pp. 40-41, 2000, AAAI Press, Las Vegas, Nevada, USA.

[9] D. Dasgupta, Z. Ji and F. González. Artificial Immune System (AIS) Research in the Last Five Years, *IEEE Evolutionary Computation, 2003. Cec'03.The 2003 congress on*, Vol. 1, pp. 123-130, 2003.

[10] J. R. Al-Enezi, M. F. Abbod and S. Alsharhan. Artificial Immune Systems–Models, Algorithms and Applications, International Journal, 2010.

[11] Farmer J D, Packard N H and Perelson A S. The immune system, adaptation, and machine learning, *Physica D*, Vol. 22, pp. 187-204, 1986.

[12] D. Dasgupta, K. KrishnaKumar and D. Wong. Negative Selection Algorithm for Aircraft Fault Detection, *3rd International Conference on Artificial Immune Systems*, Vol. 23, pp. 1-13, 2004, Springer-Verlag.

[13] González,F. A study of artificial immune systems applied to anomaly detection. University of Memphis, phD:199, 2002.

[14] Zhou Ji. Real-Valued Negative Selection Algorithm with Variable-Sized Detectors, *Genetic and Evolutionary Computation–GECCO 2004*, 287-298, 2004.

Copyright © 2012 DET Corp., Japan All Rights Reserved
International Journal of Comprehensive Engineering
Part A, 2(2), 125-134, 2013
Doi: 10.14270/IJCE2013.2.2.a125
Regular paper

ISSN 2186-2680
e-ISSN 2186-2656
www.iace-journal.org

A review on rolling bearing fatigue life prediction

Shuilong He [1], Yanyang Zi [1, #], Zhengjia He [2], Zigang Cai [1] and Wangpeng He [1]

[1] School of Mechanical Engineering, Xi'an Jiaotong University,
Xi'an Jiaotong University, Xi'an 710049, PR China
[2] School of Mechanical Engineering, State Key Laboratory for Manufacturing and Systems Engineering,
Xi'an Jiaotong University, Xi'an 710049, PR China

[#] Corresponding author: ziyy@mail.xjtu.edu.cn; Tel.: +86-29-82663689; Fax: +86-29-82663689

Abstract: The research of the rolling bearing fatigue life prediction has been extensively studied and developed over the past few decades with the purpose of predictive maintenance and shortening breakdown time. Due to the necessity and significant importance of bearing fatigue life prediction, there has been an increasing amount of work involving this research topic. This article reviews the techniques in previous publication, whose merits and limitations are also discussed. For clarification of preliminary material about the development of rolling element bearing life prediction, current models are summarized and classified into four different types: statistical lifetime model, fracture mechanics based lifetime model, condition monitoring data based lifetime model and integrated lifetime model. Then, according to the deficiency of the existing research, the worthy research directions, including indicators of degradation assessment, degradation failure standard, efficient and fast signal processing algorithms as well as fast and precise prognostic approaches, are pointed out.

Keywords: Rolling Bearing, Prognostics, Life Prediction Model, Information Fusion.

Received: Jul. 4,2012 / Accepted: Feb. 20,2013 / Published: Jul. 5,2013

1. Introduction

Rolling element bearing is among the key elements in machineries and it is widely used in equipments such as helicopter, aircraft's landing gearbox and the wind driven generator, etc. Therefore, there has been the extensive research in bearing's fatigue life in the past decades [1]. Prediction of bearing's fatigue life is vital to ensure the safety and reliability of machineries as well as reduce their maintenance costs. Failures of rolling bearings can be classified as the following: fatigue failure, wear, flaw, fracture, rust, creep, electric pitting, among which the fatigue failure is very common [2]. The fatigue failure results from shear stresses cyclically occurring immediately on the load carrying surface. As the rolling elements pass over the cracks fragments of material break away and cracks are progressively developed on the surface [3]. This phenomenon is known as flaking. The flaking gradually increases in extent and eventually makes the bearing unserviceable. As such, rolling bearing fatigue life prediction is a matter of great account.

The rolling bearing prognosis is the forecast of its remaining serviceable life, future working condition, or the probability of reliable operation of an equipment based on acquired condition monitoring data. The fatigue life of the rolling bearing is the total working time until their working surface (including inner ring, outer ring, roller and cage) has fatigue failure that can not satisfy the rotation and loading requirements. Usually, the fatigue life is one of the most important design criterion and performance indicators of the rolling bearing. Therefore, the predicting the remaining life of rolling bearing with high precision has constantly being a hot topic in the research of rolling bearing technology. The existing models for predicting rolling bearing life can be categorized into the following four main types: statistical lifetime model [4], fracture mechanics based lifetime model, condition monitoring data based lifetime model and integrated lifetime model [5].

2. Statistical assessment models

The statistical lifetime model is based on the relationship between the life distribution and the control factors through fatigue life tests of a large number of bearings of the same type. Generally, two approaches are employed. One approach is the traditional lifetime estimation, which is based on the assumption that the rolling bearing lifetime of event records of a population of identical units satisfies specific failure distribution using statistical models such as Weibull, Poisson and Exponential distributions. Another approach pays more attention to the fatigue failure mechanism. The Lundberg-Palmgren theory is the typical example. In order to build a widely used lifetime model, this approach keeps revising the Lundberg-Palmgren theory by means of statistics method, which also requires massive rolling bearing fatigue life tests. The second approach is pioneered by a Swedish scholar Arvid Palmgren. His work with Professor Lundberg, published in 1947 [6] and 1952 [7], put forward the well known Lundberg-Palmgren theory. Their theory assumes that the logarithm of the reciprocal of the probability of survival *S* could be expressed as a power function of orthogonal shear stress τ, the number of stress cycles until failure *N*, depth to the maximum orthogonal shear stress Z_0, and stressed volume *V*, as shown in Eq.(1).

$$\ln\frac{1}{S} \propto \int_V \frac{\tau^c N^e}{z_0^h}\mathrm{d}V \tag{1}$$

Based on maximum dynamic shear stress theory, Hertz elastic contact theory and nominal dynamic load theory [8], Lundberg and Palmgren obtained the typical rolling bearing life prediction model (L-P model). That is,

$$L_{10} = \left(\frac{C}{P}\right)^{\varepsilon} \tag{2}$$

Where L_{10} denotes the rating lifetime of rolling bearing; *C* is the basic dynamic load rating or capacity that is defined as the load that a bearing can carry for 1 million inner-race revolutions with a 90% probability of survival; *P* is the equivalent bearing load; and ε is the load-life exponent. Usually, $\varepsilon = 3$ for ball bearings and $\varepsilon = 10/3$ for cylindrical rolling bearings.

In 1985, Ioannides and Harris made modifications to Lundberg-Palmgren theory based on a material fatigue limit and discrete finite elements [9]. Their new concept of "When bearing material has a loading stress below the fatigue-limiting stress, the fatigue failure would not happen" can perfectly explain the reason for bearings' long lifetime when performing fatigue tests under ideal condition. They introduced the fatigue limit stress, known as the I-H model:

$$\ln\frac{1}{\Delta S} \propto \int_V \frac{(\tau\text{-}\tau_u)^c N^e}{z^h}\mathrm{d}V \tag{3}$$

Where τ denotes the critical shear stress; τ_u is the fatigue limit shear stress; *N* is the number of stress cycles until failure; *c*, *e* and *h* are parameters determined by experiments. This theory assumes there would be no material fatigue if the maximum stress does not exceeds the fatigue stress τ_u. In contrast to L-P model, this model is more closed to the practical situation.

Other modifications to the L-P theory are continuously being made. In 1996, Tallian developed a mathematical model based on the L-P theory and is more fit to a bearing data base [10-13]. In 2001, Yu and Harris presented a new fatigue life model (Y-H model) for bearings [14]. The proposed model is a stress-based, as opposed to empirical factor-based, method which can more accurately model the increasing demanding operating conditions of modern machinery. Moreover, the results of their investigation indicated that the introduced model could be a more accurate predictor of bearing life than either the L-P or I-H model.

The statistical lifetime model basically uses historical time-to-failure data to estimate the population characteristics (such as mean time to failure and probability of reliable operation). However, these approaches only provide general overall estimations for a large number of identical bearings. As a result, this type of estimations is useful to manufacturers that produce bearings in high volumes. Unfortunately, they may not necessarily accurate for individual operating units.

3. Fracture mechanics based assessment models

The fracture mechanics based lifetime model is an important direction of rolling bearings life prediction. These models have assumed that the life of bearings was dominated by crack propagation. In order to achieve accurate bearing prognostics, these models combine crack propagation formula with monitoring data.

In 1850s, a German engineer, Woehler, conducted vast experiments to explore the fatigue systematically for the first time. He introduced the concept of stress-life curve and fatigue limit. Manson and Coffin were the pioneers whose work related the number of cycles to crack initiation to the amplitude of plastic strain [15]. In 1954, they proposed the noted equation of the strain-life curve, namely the Manson-Coffin equation where the total strain amplitude $\Delta\varepsilon$ is divided into elastic $\Delta\varepsilon_{\mathrm{e}}$, and plastic $\Delta\varepsilon_{\mathrm{p}}$ components. That can be written as

$$\Delta\varepsilon = \Delta\varepsilon_{\mathrm{e}} + \Delta\varepsilon_{\mathrm{p}} = \frac{\sigma'_f}{E}(2N)^b + \varepsilon'_f(2N)^c \tag{4}$$

Where σ'_f and ε'_f denotes the fatigue strength coefficient and ductility coefficient respectively; E is the Young's modulus of the material; $2N$ is the number of cycles until fatigue failure (crack initiation); b and c denote the fatigue strength and ductility, respectively.

In 1997, G. Irwin presented the stress intensity method and established the concept of stress intensity factor K which laid the foundation of life prediction based on fatigue crack propagation [16]. In 1963, a pioneering researcher, P. Paris, suggested the use of Irwin stress intensity factor (more precisely, its range ΔK) to characterize the rate of crack propagation $\mathrm{d}a/\mathrm{d}N$ [17,18].The following fatigue crack propagation model based on Paris's law has been widely acknowledged for many years:

$$\frac{\mathrm{d}a}{\mathrm{d}N} = C_0(\Delta K)^n \tag{5}$$

Where a is the instantaneous length of a dominant crack and N represents running cycles; the parameters C_0 and n are regarded as material-dependent constants. The term ΔK is the range of stress intensity factor over one loading cycle.

In 1996, Asok and Sekhar proposed a nonlinear stochastic model of fatigue crack dynamics for real-time computation of the time-dependent damage rate and accumulation in mechanical structures [19]. In 2000, Li et al. presented a stochastic defect-propagation model by expanding the deterministic model to accommodate a lognormal random variable [20]. Moreover, an on-line procedure based on recursive least-squares method has been developed to calibrate the model without the need of priori knowledge. The simulation proved that the proposed model can continuously improve prediction accuracy and reduce prediction uncertainties. In 2002, H. Oppenheimer and A. Loparo developed a life model based on the Forman crack growth law of linear elastic fracture mechanics to determine the number of machine cycles remaining until catastrophic failure [21]. In the same year, Qiu et al. discussed the use of damage mechanics for bearing prognosis by considering bearing system as a single-degree-of-freedom vibratory system [22]. They presented a stiffness-based prognostic model based on vibration data and damage mechanics. Then in 2006, Marble and Morton developed a model which computes the spall growth trajectory and time to failure based on operating conditions, and uses diagnostic feedback to self-adjust and reduce prediction uncertainty [23].

The fracture mechanics-based assessment model requires only a set of small samples. When the predetermined physical mechanism is well matched to the systems, these models predict the rolling bearings residual life accurately. Although the deterministic damage model and the stochastic model are both capable of predicting crack propagation rate, there are still several challenges when they are used in practical situations, especially for mechanism are more complicated and the real-time monitoring of the crack length and flaking area is hard.

4. Condition monitoring data based assessment models

The condition monitoring data based lifetime models are built in the view point of inverse problem, instead of based on physical mechanism. These models adaptively construct bearing's performance degradation index based on historical records of condition monitoring data and further build bearing's lifetime assessement model. These models do not require prior knowledge. Their procedures consist of the following steps: condition data acquisition, feature extraction, feature selection, indicator construction and model construction, as shown in Fig. 1.

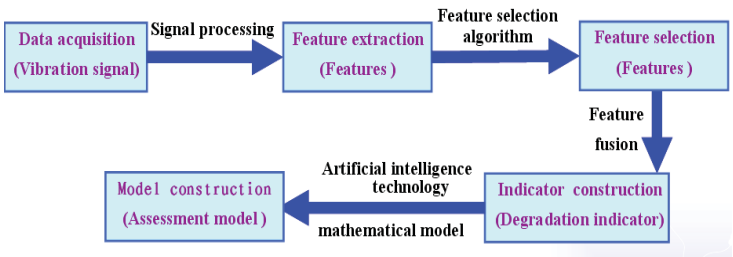

Fig. 1 The flow chart of life assessment model based on condition monitoring data

The condition data acquisition step collects multiple processing parameters such as vibration, noise, temperature, acoustic emission and fragment content, etc, which serve as means of reflecting the operating stauts of bearings. Owing to its good performance in reflecting bearings dynamic characteristics, vibration becomes the major source of monitoring information.

In terms of the construction of degradation indicator, the intial research are characteristic of using signal indexes derived from time domain, frequency domain and time-frequency domain. For example, Gebraeel employed bearing fault frequency and the mean value of its first six harmonic amplitudes as degradation index [24, 25]. Qiu derived a minimum quantization error (MQE) index, which is sensitive to bearing's early failure, through feature fusion technique of self organizing map (SOM) [26]. The MQE index is presented as a feasible index as it shows significant change according to the development of the failure. Pan and Chen [27] proposed a new status index calculation method based on improved wavelet packet decomposition (IWPD) and support vector data description (SVDD), through which the distance from the feature vector of the bearing of unknown status to the optimal hyperplane are calculated and is used as status assessment index. Yan and Gao investigate the application approximate entropy (ApEn) in machine health monitoring [28]. The results of the simulation and experiment show ApEn has robust performance in characterizing the fault severity. Huang and Li try to make prediction of ball bearing's remaining useful life through a new scheme based on self-organizing map (SOM) and back propagation neural network methods [29]. They used MQE index derived from six vibration index as the bearing's characteristic indicator. Liao and Lee proposed a novel performance assessment method based on transient data without failure history [30]. The performance index of the machine is calculated based on the overlap between the distribution of the baseline feature space and that of the testing feature space. Pan et al. presented a new method based on lifting wavelet packet decomposition and fuzzy c-means [31,32]. This new method utilized normal and final failure data as training samples to build assessment model and the subjection of tested data to normal state is defined as the degradation indicator. Reyes adopted the ratio of condition index to failure threshold to indicate the bearing degradation [33].

After the construction of degradation index, algorithm which maps degradation index into the remaining life needs to be investigated. According to modeling algorithm, the condition monitoring data based lifetime model fall into two main categories. The first category made certain assumptions to the index which can reflect the bearing status and its objective was to select relevant mathematical model to predict bearing life or evaluate bearing status. Nagi Gebraeel et al. proposed Bayesian updating methods that use real-time condition monitoring information to update the stochastic parameters of exponential degradation models. Zhang et al. used Hidden Markov Models (HMMs) to predict bearing lifetime [34]. In a HMM, a system is modelled to be a stochastic process in which the subsequent states have no causal connection with previous states. Li and Shin developed a method to identify a bearing dynamic model from a measured bearing vibration using a system identification method [35]. Then, this bearing dynamic model is properly inverted to recover the impact impulse behind a measured vibration signal. However, their method needs high signal to noise ratio (SNR) in order to get high accuracy. Orchard introduced a method for accurate and precise prediction of a failing component based on particle filtering and learning strategies [36].

The second category used machine learning theory, such as fuzzy logic, neural network and support vector machine (SVM), to predict bearing lifetime. Many researches have shown that artificial neural network has better performance than system identification in predicting bearing lifetime. Moreover, artificial neural networks are able to capture complex phenomena without prior knowledge, and can be reduced to a simpler model if the phenomena are not complex [37-39]. Shao and Nezu developed a prediction model based on variables characterizing the state of a deterioration mechanism which are determined from on-line measurements and the application of prediction of remaining life via a compound model of neural computation [40]. Gebraeel and Lawley presented a feedforward backpropagation neural network based model to predict bearing life [24]. Huang et al. proposed a scheme for the prediction of a ball bearing's remaining useful life based on self-organizing map and back propagation neural network methods [29]. Wang developed a recurrent

wavelet neural network (RWNN) to predict rolling element bearing crack propagation [41]. However, their method needs large dataset and is computationally expensive. Nagi Gebraeel et al. presented several neural network based models to predict bearing life. Meanwhile, They combined neural network and lifting Bayes approach to enhance the accuracy of the prediction. Sun used multivariable support vector machine to predict bearing life [42].

Condition monitoring data based life model is built directly from condition monitoring data. It is a simple method and doesn't need priori knowledge. Moreover, the modeling only aim at signal bearing. Therefore, it has the ability to predict signal bearing life, which is suitable to the circumstance of limited quantities in bearing industry. However, the modeling need large number of samples and failure data. Unfortunately, factories and military organizations don't allow their equipment run to failure. For this reason, it is really hard to collect failure data of bearing. Another limitation is that this model is sensitive to interference, which affects the accuracy of the prediction.

5. Integrated life assessment models

Three factors weigh heavily against the establishment of integrated life assessment model: (1) harsh and varying operating conditions of the bearing; (2) dynamic characteristics cause difficulties in applying the high precision life assessment model based on theoretical damage mechanism; (3) lack of model depend on data from condition monitoring. Some scholars took full advantage of all available information from the viewpoint of information fusion and presented the integrated life assessment model. In [43], Hall classified the information fusions into three types: source fusion, feature fusion and decision fusion.

In the level of source fusion. The condition monitoring data may reflect the operating status of a specific unit, while unable to replace this type of machine's overall reliability property. Taking this fact into considerration, several valueable models effectively combine the reliability information with the condition monitoring data to perform more dependable prediction and higher precision. Tsen et al. integrated mathematical model simulation data and experimental data in artificial neural network learning [44].

Goode et al. proposed a statistical method in predicting the residual life of pump [45]. In his method, statistical process control theory is used to set the alarm threshold and normal distribution model is imposed for normal working status. Statistical process control theory assumes that: under stable condition, if the continuous monitoring data has overlapping with the normal state data to the rate of 99.743%, the equipment is in the transition stage between normal state to the initial damage state (IP), otherwise it belongs to the initial damage to the failure state (PF). And the remaining life of the equipment is predicted by using statistical information and monitoring data. In IP stage, statistical data is utilized to calculate the cumulative failure function; and in PF stage, monitoring data is used to calculate the cumulative failure function. So it effectively combines the reliability information and the monitoring data to achieve a higher precision remaining life prediction.

Jardine et al. applied proportional hazards model (PHM) to assess the reliability of rolling bearing and engine [46,47].The model can be defined by the equation

$$h(t,\mathbf{Z}) = h_0(t)\exp\left(\sum_i \gamma_i Z_i\right) \tag{6}$$

Where $h_0(t)$ is a deterministic baseline hazard function such as Weibull distribution, Poisson distribution, and estimated using the maximum likelihood method. **Z** is a vector of time-dependent covariates such as vibration and temperature ,and γ_i is the weight coefficient. This model took the following factors into consideration: the reliability based on probability and statistics to reflect the overall average properties and operational reliability that reflects the individual operational status and performance degradation, so it obtains the reliability of the equipment and carries out preventive maintenance decision-making. Ding et al, working at Xi'an Jiaotong University, used the proportional failure rate model to assess the reliability of the CNC cutting tools and aircraft engine bearings.

In view of the lack of historical failure data, Heng et al. presented a life assessment model, which made full use of the suspension data and integrated the reliability and condition monitoring data effectively, where the suspension data refers to data not yet reached the failure state [1]. Firstly, using the Kaplan - Meier estimator and the failure Probability Density Function (PDF) estimator calculates the instantaneous reliability, then treats the instantaneous reliability as the preamplifier neural network training target, using neural network to predict the survival probabilities of the running machine, finally this model can make full use of various information and realize long term prediction.

With the foundation of statistical bearing fatigue life theoretical models and recent development of research in fracture mechanics, Shen, from Xi'an Jiaotong University, proposed a extended model of fatigue based on bearing's vibration data [48]. This model combines second generation wavelet packet transform and shock pulse method to make quantitative assessment of bearing damage, and then combined with the rolling bearing fatigue spalling extended model and quantitatively analyse the area of the law of fatigue spalling of the bearing during the operation. In Shen's method, the quantitative assessement criterion for failure is illustrated in Fig. 2.

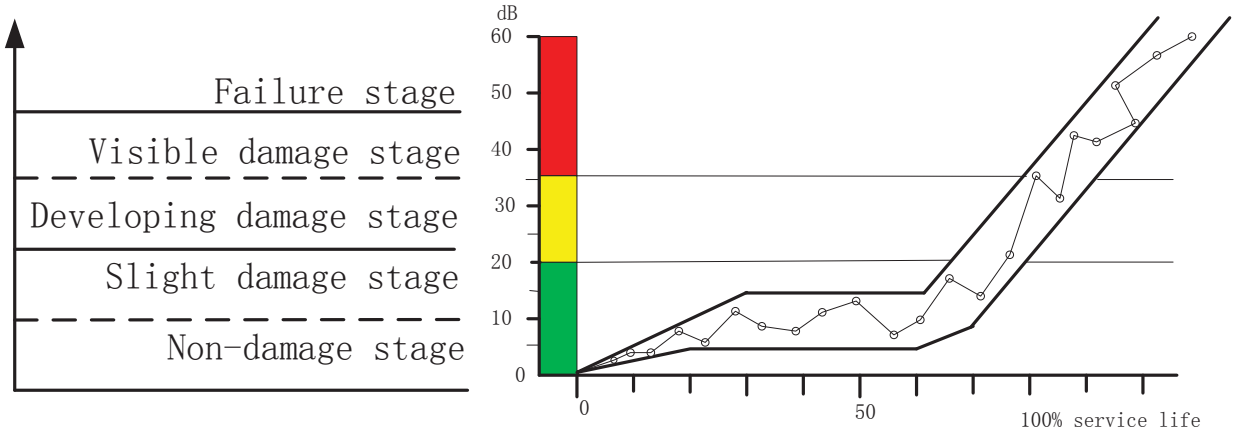

Fig. 2 Mapping between failure severity and shock value

In the level of decision fusion, with the findings of the study, a single prediction model is only valid for the type of bearing recession at some stage or some kind of fault type.There will bring large errors if using the single model to predict the bearing life cycle. According to this, some scholars try to combine multiple assessment models to predict the remaining life of the bearing, and have made some progress. But the question is which model should be choiced in the different circumstances.

Liao et al. proposed an lifetime assessment method based on integration of multiple auto-regressive and moving average (ARMA) model [49]. Firstly, self-organizing neural network are employed to realize the effective integration of multi-source information so that the status of bearings can be assessed and classified. Secondly, enhanced learning techniques are used to determine the appropriate forecasting model in accordance to bearing's different operating status, and subsequently the remaining life is predicted. Finally, the remaining life prediction precision is enhanced through an improved probability evaluation algorithm.

Gang et al. proposed a lifetime prediction model based on information fusion [50]. This model utilizes the source fusion of multi-source information so as to realize a reasonable assessment of the compressor's state. The remaining life of the compressor is predicted by the integrated D-S recession model and the least square support vector machine (SVM) model.

Guo, working at Harbin Institute of Technology, proposed four improved variations of Markov life prediction model [51]. Among these models, a dynamic scale Markov lifetime prediction model is based on the diversity of the thought of dynamic weighting prediction method. This model takes the concept of dynamic variable-dimension of wavelet theory into consideration, and divides the historical information and real-time information into a different state, overcoming the shortcomings of the lack of unknown future information of single-sample prediction model.

Feature fusion is made with the purpose of obtaining the degradation assessment index possessing robuster performance in capturing the change of bearing operating status, which is detailedly described in section 1. 3.

Integrated life assessment model attempts to make full use of the combination of available information, as shown in Fig. 3, real-time feature of diagnosis monitoring information and the universality of statistical information, and the microcosmic characteristic of the fracture mechanics to establish prediction models with higher precision. These models overcome the disadvantage of low accuracy of the single step prediction at single point, achieving dependable life prediction performance, which is an important development direction of life assessment model.

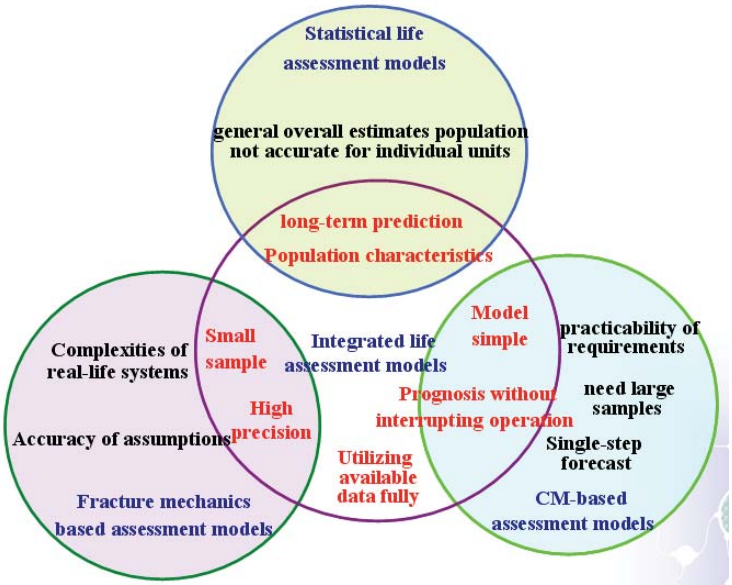

Fig. 3 Relationship among the four life assessement models in section 2-5 (Remarks in red color represent its merits，and remarks in black color represent its shortcomings)

6. Conclusion

As mentioned above, the technology of bearing life assessment has made a number of progresses in recent years, and achieved some effect in practice. However, many fundamental issues still remain:

(1) Construction of robust degradation assessment index that can capture the change of bearing’s performance

Steady indicators of the recession on the bearing condition assessment, intelligent early warning and the effectiveness and accuracy of the life prediction is very necessary.And the multi-feature fusion offers the possibility to select this indicator. Different characteristics reflect different operational phase’s characteristic of the bearing, play an optimization and combination of them,so it not only retains effective information of the fusion of multiple features in a certain extent, but also eliminates redundant information due to the subjective and objective factors involved in the integration of features, which is of great sinnificance to monitoring and diagnosis of bearings.But the index construction method based on feature fusion have a certain degree of inadequacy at present. Qiu et al. proposed a state evaluation method based on SOM, but the difficulty is how to construct the subspace that stably reflects bearing recession mode’s characteristics from so many original features. Yuna Pan et al. proposed a assessment method based on the combination of improved wavelet packet decomposition (IWPD) and support vector data description (SVDD), but results in poor precision on bearing evaluation of the variable condition of multiple features.

Through the analysis of above-mentioned methods, it is concluded that indicators fusion performance depends on the input characteristics of the training phase’s performance.In fact, not all features are useful to characteristic fusion, some irrelevant and redundant features will not be able to play a positive role on feature fusion may also play a negative role; if we use all features at the same time, the calculation amount will increase greatly because of a large number of irrelevant and redundant features, which causes the dimension disaster.Therefore, it is necessary to design a kind of feature selection methods to choose a subset of features with excellent characteristics, so as to ensure and improve the performance of the fusion index, reduce the amount of calculation, improve the accuracy and robustness of the condition assessment and life prediction.

(2) Development of effective and fast signal processing algorithms

In the early stage of failure, the fault features are very weak and are of non-stationary nature. Moreover, these futures are buried in strong background noises. It is of great difficult in extracting the fault feature from vibration signals of such low signal-to-noise ratio. In the fields of non-stationary signal processing, there has been a number of new signal analysis theory and technology, and the one most widely used to in dynamic signal analysis is the theroy and technology of wavelets. However, the scalar wavelets cannot satisfy the excellent characteristic of orthogonality, symmetry, compact support and high order vanishing moments simultaneously, thus only fit for signal feature extraction of single type. Many researchers pay attention to the research of multiwavelets and other methods of signal processing.

(3) Correct distinction between normal status and early damage status

The current alarm thresholds are generally settled according to international ISO standards (ISO13381-1, ISO-10816, and ISO-7919), and then fine-tune it according to the operator's experience. ISO specified the alarm

threshold of the RMS value just according to the specifications and installation ways of the machine, while the other characteristic indicators' explanations and descriptions are not provided. However, we know the RMS value is not sensitive to the initial damage, restricting its performance in industrial applications. While for the application of other characteristics indicators, each indicator should be set an alarm threshold, and this alarm threshold is generally no longer applicable in case the work environment changes, so the formulation of alarm strategy becomes very difficult, at the same time hard threshold division or relatively soft threshold partition are generally used in the practical application, which is most likely cause the misrepresentation or omission due to accidental events of machines.

(4) Establishment of high precision life prediction model restricted to small samples

In engineering applications, the history failure information of the bearing installed in specific equipment is difficult to obtain, its degradation and failure mechanism is not clear, and the data reference of the same type of bearings is not dependable due to their different operating conditions. In most cases, only bearing's running data in normal operation status can be obtained, restricting the application of remaining life assessment model in engineering practice. So it is a big challenge to construct life prediction model with high accuracy only rely on normal state data with limited samples.

Acknowledgment

This research is supported financially by the key project of National Natural Science Foundation of China (no 51035007), National Natural Science Foundation of China (no 50975220), National Basic Research Program of China (no 2009CB724405), Important National Science and Technology Specific Projects (no 2010ZX04014-016) and the Specialized Research Fund for the Doctoral Program of Higher Education (no 20110201130001).

References

[1] S. Y. Heng. *Intelligent Prognostics of Machinery Health Utilising Suspended Condition Monitoring Data*, Queensland University of Technology, 2009.

[2] R. B. Randall and J. Antoni. Rolling Element Bearing Diagnostics-a Tutorial, *Mechanical Systems and Signal Processing*, Vol. 25, No. 2, pp. 485-520, 2011.

[3] X. W. Miao and D. W. Wang. Progress of Life Theory of Rolling Bearings, *Bearing*, No. 3, pp.47-52, 2008.

[4] J. F. Lawless. *Statistical Models and Methods for Lifetime Data*, New York: John Wiley and Sons,1982.

[5] E. V. Zaretsky and J. V. Poplawski. Rolling Bearing Life Prediction-Past, Present, and Future. *International Tribology Conference*, pp.1-7, October 30-November 2, 2000, Nagasaki, Japan.

[6] G. Lundberg and A. Palmgren. *Dynamic Capacity of Roller Bearings*, Ing. Vetanskaps Akad. -Handl., No. 196, 1947.

[7] G. Lundberg and A. Palmgren. *Dynamic Capacity of Roller Bearings*, Ing. Vetanskaps Akad. -Handl., No. 210, 1952.

[8] H. Hertz. *On the Contact of Rigid Elastic Solids and on Hardness*, MacMillan, London ,1896.

[9] E. Ioannides and T. A. Harris. A New Fatigue Life Model for Rolling Bearings, *Journal of Tribology*, No. 3, pp. 367-378, 1985.

[10] T. E. Tallian. Data-fitted Bearing Life Prediction Model-part, Mathematical Model, Tribology Transactions, Vol. 39, No. 2, pp. 249-258, 1994.

[11] T. E. Tallian. Data-fitted Bearing Life Prediction Model-part Ⅱ, Experimental Database, *Tribology Transactions*, Vol. 39, No. 2, pp. 259-268, 1996.

[12] T. E. Tallian. Data-fitted Bearing Life Prediction Model-part Ⅲ, Parametric Study, *Tribology Transactions*, Vol. 39, No. 2, pp. 269-275, 1996.

[13] T. E.Tallian. Data-fitted Bearing Life Prediction Model-part Ⅳ, Model Implementation for Current Engineering Use, *Tribology Transactions*, Vol. 39, No. 4, pp. 957-963, 1996.

[14] W. K. Yu and T. A. Harris. A New Stress-Based Fatigue Life Model for Ball Bearings, *Tribology Transactions*, Vol. 44, No. 1, pp. 11-18, 2008.

[15] A. Niesłony, C. Dsoki and K. Heinz. New Method for Evaluation of the Manson-Coffin-Basquin and Ramberg-Osgood Equations with Respect to Compatibility, *International Journal of Fatigue*, Vol.30, pp. 1967-1977, 2008.

[16] G. R. Irwin. Analysis of Stresses and Strains Near the End of A Crack Traversing A Plate, *J. appl. Mech*, Vol. 137, pp. 167-170, 1997.

[17] P. Paris and F. Erdogan. A Critical Analysis of Crack Propagation Laws, *Journal of Basic Engineering*, Vol. 85, No. 4, pp. 528-534, 1963.
[18] N. Pugnoa, M. Ciavarellab, P. Cornettia and A. Carpinteri. A Generalized Paris' Law for Fatigue Crack Growth, *Journal of the Mechanics and Physics of Solids*, Vol. 54, pp. 1333-1349, 2006.
[19] R. Asok, T. Sekhar. Stochastic Modeling of Fatigue Crack Dynamics for On-Line Failure Prognostics, *IEEE Transactions on Control Systems Technology*, Vol. 4, No. 4, pp. 443-451,1996.
[20] Y. Li, T. R. Kurfess, S. Y. Liang. Stochastic Prognostics for Rolling Element Bearings, *Mechanical Systems and Signal Processing*, Vol. 14, No. 5, pp. 747-762, 2000.
[21] H. O. Charles and A. L. Kenneth. Physically Based Diagnosis and Prognosis of Cracked Rotor Shafts, *Proceedings of the Society of Photo-optical Instrumentation Engineers*, Vol. 4733, pp. 122-132, 2002.
[22] J. Qiu, C. Zhang and S. Y. Liang. Damage Mechanics Approach for Bearing Lifetime Prognostics, *Mechanical Systems and Signal Processing*, Vol. 16, No. 5, pp. 817–829, 2002.
[23] S. Marble and B. P. Morton. Predicting the Remaining Life of Propulsion System Bearings, *Aerospace Conference*, IEEE xplore,2006
[24] N. Z. Gebraeel, M. A. Lawley. A Neural Network Degradation Model for Computing and Updating Residual Life Distributions, *IEEE Transactions on Automation Science and Engineering*, Vol. 5, No. 1, pp. 154-163, 2008.
[25] N. Z. Gebraeel, M. Lawley. Residual Life Predictions From Vibration-Based Degradation Signals: A Neural Network Approach, *IEEE Transactions on Industrial Electronics*, Vol. 51, No. 3, pp. 649-700, 2004.
[26] H. Qiu, J. Lee, J. Lin and G. Yu. Robust Performance Degradation Assessment Methods for Enhanced Rolling Element Bearing Prognostics, *Advanced Engineering Informatics*, Vol.17, No. 3-4, pp. 127-140, 2003.
[27] Y. Pan, J. Chen and L. Guo. Robust Bearing Performance Degradation Assessment Method Based on Improved Wavelet packet-Support Vector Data Description, *Mechanical Systems and Signal Processing*, Vol. 23, No. 3, pp. 669-681, 2009.
[28] R. Q. Yan and R. X. Gao. Approximate Entropy as a Diagnostic Tool for Machine Health Monitoring, *Mechanical Systems and Signal Processing*, Vol. 21, No. 2, pp. 824-839, 2007.
[29] R. Q. Huang, L. F. Xi, X. L. Li and et al.. Residual Life Predictions for Ball Bearings based on Self-organizing Map and Back Propagation Neural Network Methods, *Mechanical Systems and Signal Processing*, Vol. 21, No. 1, pp. 193-207, 2007.
[30] L. X. Liao and J. Lee. A Novel Method for Machine Performance Degradation Assessment based on Fixed Cycle Feature Stest, *Journal of Sound and Vibration*, Vol. 326, No. 3-5, pp.894-908, 2009.
[31] Y. N. Pan, J. Chen and X. L. Li. Bearing Performance Degradation Assessment based on Lifting Wavelet packet Decomposition and Fuzzy c-means, *Mechanical Systems and Signal Processing*, Vol. 24, No. 2, pp. 559-566, 2010.
[32] Y. N. Pan and J. Chen. Spectral Entropy: A Complementary Index for Rolling Element Bearing Performance Degradation Assessment, *Proc. ImechE Part C*, Vol. 223, No. 5, pp. 1223-1331, 2009.
[33] A. S. Reyes. *Data-Driven Life Prediction Model for Bearing Failure*, Mechanical Engineering University of Puerto Rico MayagUez Campus, 2009
[34] X. D. Zhang, R. Xu, C. Kwan and et al.. An Integrated Approach to Bearing Fault Diagnostics and Prognostics, *2005 American Control Conference*, pp. 2750-2755, June 8-10, 2005, Portland, OR, USA.
[35] C. J. Li and H. Shin. Tracking Bearing Spall Severity Through Inverse Modeling, *ASME International Mechanical Engineering Congress and Exposition*, Anaheim, California USA, November 13-20, 2004.
[36] M. Orchard, B. Q. Wu and G. Vachtsevanos. A Particle Filtering Framework for Failure Prognosis, *Proceedings of WTC2005 World Tribology Congress III*, September 12-16, 2005, Washington D. C., USA.
[37] J. Lee. A Systematic Approach for Developing and Deploying Advanced Prognostics Technologies and Tools: Methodology and Applications, *Proceedings of the Second World Congresson Engineering Asset Management*, pp.1195-1206, 2007, Harrogate, UK.
[38] P. Tse and D. Atherton. Prediction of Machine Deterioration Using Vibration Based Fault Trends and Recurrent Neural Networks, *Transactions of the ASME Journal of Vibration and Acoustics*, Vol. 121, No. 3, pp. 355-362, 1999.
[39] D. G. Bostwichk, H. B. Burke. Prediction of Individual Patient Outcome in Cancer, *Cancer Supplement*, Vol. 91, pp. 1643-1646, 2001
[40] Y. Shao and K. Nezu. Prognosis of Remaining Bearing Life Using Neural Networks, *Proc. ImechE Part I*, Vol. 214, No. 13, pp. 217-229, 2000.

[41] P. Wang. Fault Prognostics Using Dynamic Wavelet Neural Networks, Artificial Intelligence for Engineering Design, *Analysis and Manufacturing*, Vol. 15, No. 4, pp. 349-365, 2001.
[42] C. Sun. *Research on Bearing Life Prediction Based on Support Vector Machine and its Applications*, Xi'an Jiaotong University, 2010.
[43] D. L Hall and J. Llinas. An Introduction to Multisensor Data Fusion, *Proceedings of the IEEE*, Vol. 85, No. 1, pp. 6-23, 1997.
[44] A. Y. Tsen, S. S. Jang, D. S. H. Wong and et al. Predictive Control of Quality in Batch Polymerization Using Hybrid Ann Models, *AIChE Journal*, Vol. 42, No. 2, pp. 455-465, 1996.
[45] K. B. Goode, J. Moore and B. J. Roylance, Plant Machinery Working Life Prediction Method Utilizing Reliability and Condition-Monitoring Data, *Proceedings of Institution of Mechanical Engineers Part E*, Vol. 214, No. E2, pp. 109-122, 2000.
[46] A. K. S. Jardine, P. M. Anderson and D. S. Mann, Application of the Weibull Proportional Hazards Model to Aircraft And Marine Engine Failure Data, *Quality and Reliability Engineering International*, Vol. 3, No.2, pp. 77-82, 1987.
[47] A. K. S. Jardine, P. M. Anderson, N. Reid and J. Stafford. Proportional Hazards Analysis of Diesel Engine Failure Data, *Quality and Reliability Engineering International*, No. 5, pp. 207-216, 1989.
[48] S. W. Shen. *Research on Rolling Element Bearing Fatigue life Based on Quantitavie Diagnosis*, Xi'an Jiaotong University, 2010.
[49] L. X. Liao. *An Adaptive Modeling for Robust Prognostics on a Reconfigurable Platform*, School of the University of Cincinnati, 2010.
[50] G. Niu and B. S. Yang. Intelligent Condition Monitoring and Prognostics System Based On Data-Fusion Strategy, *Expert Systems with Applications*, Vol. 37, No. 12, pp. 8831-8840, 2010.
[51] C. Z. Guo. *Study of Remaining Life Prediction Based on Markov Model*, Harbin Institute of Technology, 2009.

Copyright © 2012 DET Corp., Japan All Rights Reserved
International Journal of Comprehensive Engineering
Part A, 2(2), 135-141, 2013
Doi: 10.14270/IJCE2013.2.2.a135
Regular paper

ISSN 2186-2680
e-ISSN 2186-2656
www.iace-journal.org

Application of intelligent data unit based on embedded Linux in wireless monitoring system of rolling bearings

Hongfang Yuan [1], Fangming Li [1], Xi Cao [1], Huaqing Wang [2, #], Jianfeng Yang [2] and Wenbin Liu [2]

[1] School of Information Science and Technology, Beijing University of Chemical Technology, Beijing, 100029, China
[2] School of Mechanical and Electrical Engineering, Beijing University of Chemical Technology, Beijing, 100029, China

[#] Corresponding author: wanghq_buct@hotmail.com; Tel.: +86-138-0102-3830;

Abstract: An intelligent data unit based on embedded Linux system is designed to monitor operating condition of rolling element bearings. Meanwhile, specific fault can be diagnosed by the intelligent data unit in real-time. As a node of wireless monitoring network, the unit can also upload the monitoring result and fault data to upper server. Compared with other detection devices, this unit has the advantage in parallel data processing and wireless transmission. Thus performance of the whole wireless monitoring network would be improved. In the experiments, it has been verified that condition monitoring and fault diagnosis could be achieved by the intelligent data unit effectively and accurately.

Keywords: Rolling Bearing, Condition Monitoring, Fault Diagnosis, Embedded Linux, ARM.

Received: Oct. 10,2012 / Accepted: Feb. 20,2013 / Published: Jul. 5,2013

1. Introduction

As the fundamental part of each kind of industrial equipments, rolling bearing and its operation status directly affect the performance, security and effectiveness of the entire manufacturing system. Therefore, it is very meaningful to do deep research on detection methods and system designing of condition monitoring and fault diagnosis based on rolling element bearings. At present, means of rolling monitoring and diagnosis mainly focus on the analysis of released signals during its operation, such as vibration signal, temperature signal and acoustic emission signal [1]. Through many years' research and development, vibration detection technique has been relatively accepted, also with high accuracy and popular application. However, current devices for vibration detection are mainly portable monitoring terminals, which should be used in the way of regular inspection. This detection method is inaccurate for the reason that human experience is largely depended on while the rolling bearing has large life dispersion. As a result, there are many limitations on the application of portable monitoring terminal in equipment monitoring under complex work situation [2].

To solve problems of rolling bearings monitoring manner presented above, the combination of embedded technology and wireless communication technology is used in system designing to improve data processing ability and wireless communication capability of the intelligent data unit. Three parts are included and their tasks are described as follows: vibration signal acquisition, signal analysis in time-domain and frequency-domain, wireless data communication [3]. Collected vibration signals of rolling bearings would be processed instantly in time-domain and frequency-domain, then results of condition recognition and fault diagnosis would be transmitted back to monitoring center for further verification and judgment. And it had been verified by experiments that each module of intelligent data unit can finish the tasks of condition monitoring and fault warning with high-efficiency.

2. Principle of Condition Monitoring and Fault Diagnosis

During the operation of rolling bearings, vibration signals are released because of the impact between roller and inner-race or outer-race. When there is some damage on outer-race, inner-race or roller, an alternating vibratory force would be generated, which could intensify bearings' vibration and strengthen energy on some certain frequencies. Based on the principle, vibration signals collected from sensors would be processed by intelligent data unit for further analysis, to achieve the target of rolling bearings condition monitoring and fault diagnosis. The function and relation of each module is shown in Fig.1.

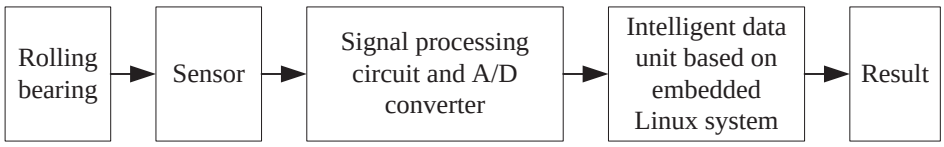

Fig. 1 Principle of condition monitoring and fault diagnosis

Vibration signals and rotate speed signals are collected by signal acquisition unit. While vibration signals are obtained by acceleration transducer, rotate speed signals are gained through the method of Key-phase signal detection. After signal processing circuit and A/D converter, collected signals are transformed to digital signals available in digital signal processing platform [4]. Condition recognition would be completed by diagnosis methods running in the intelligent data unit based on embedded Linux system, and then results of condition recognition and fault data would be transmitted to upper computer through wireless network [5].

3. Design of Intelligent Data unit Based on Embedded Linux

The high-speed ARM9 processor is selected as the CPU of the intelligent data unit, with embedded Linux as its software platform. System designing especially software development will be simplified with humanized program interface of embedded Linux platform [6].

3.1 Hardware Design of Intelligent Data Unit

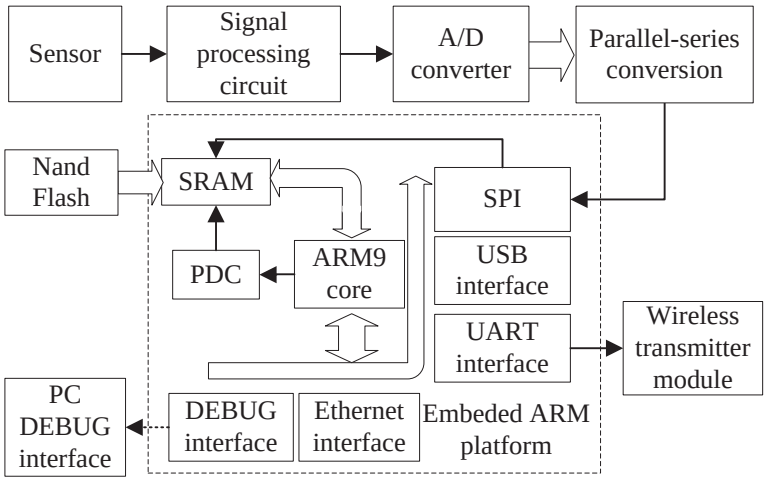

Fig. 2 Hardware structure of intelligent data unit

As is shown in Fig.2, vibration signals are measured by accelerometer and rotate speed signals are measured by eddy current sensor. And veracity of collected signals are largely improved by low-pass filter and amplifier of signal processing circuit unit. Gain of amplifier and cutoff frequency of low-pass filter can be set based on the design of combination of multiplexer and resistance group. The AD9240 with 14-bit sampling precision used as A/D converter can ensure veracity of collected signal. The 32-bit AT91SAM9260 is selected as core processor, and design of core circuit board based on industrial condition requirement can adapt to complex industrial environment. Two-level storage structure with SRAM as its internal memory and Nand Flash as its external memory is used in memory design of intelligent data unit. After system powers on, BootLoader will be copied from Nand Flash to SRAM and then conduct system initialization and Linux kernel loading [7]. Meanwhile, design of external interfaces for data collecting, transmitting and system debugging can meet the requirement of industrial application. Detail design of main external interfaces is as follows:

a) SPI (Serial Peripheral Interface) is used as data collecting interface. Data transmission rate on SPI bus is programmable. DMA (Direct Memory Access) technology is applied to SPI data transmission. In DMA mode, data will be copied and stored directly from read buffer of SPI to SRAM. Thus CPU load would be largely reduced by using data transmission method of DMA [8].
b) UART (Universal Asynchronous Receiver or Transmitter) is used as data communication interface between ARM and wireless transmitter module. Results of condition recognition and diagnosis are transmitted from ARM to wireless module via UART interface.
c) DEBUG interface, USB interface and Ethernet interface are communication channel between embedded system and PC, which are used for system debugging or software updating.

3.2 Software Design of Intelligent Data Unit

Based on the design of hardware, the tasks of software consist of data collecting, data storage, data analysis on time-domain and frequency-domain, wireless data transmitting, peripheral modules control and interrupt control. The complex tasks can hardly be finished by program with simple sequential structure or single process. Thus multi-process structure is applied to software platform to ensure availability and high effectiveness of intelligent data unit. The overall structure of software platform is shown in Fig.3. And multi-process structure is shown in Fig.4.

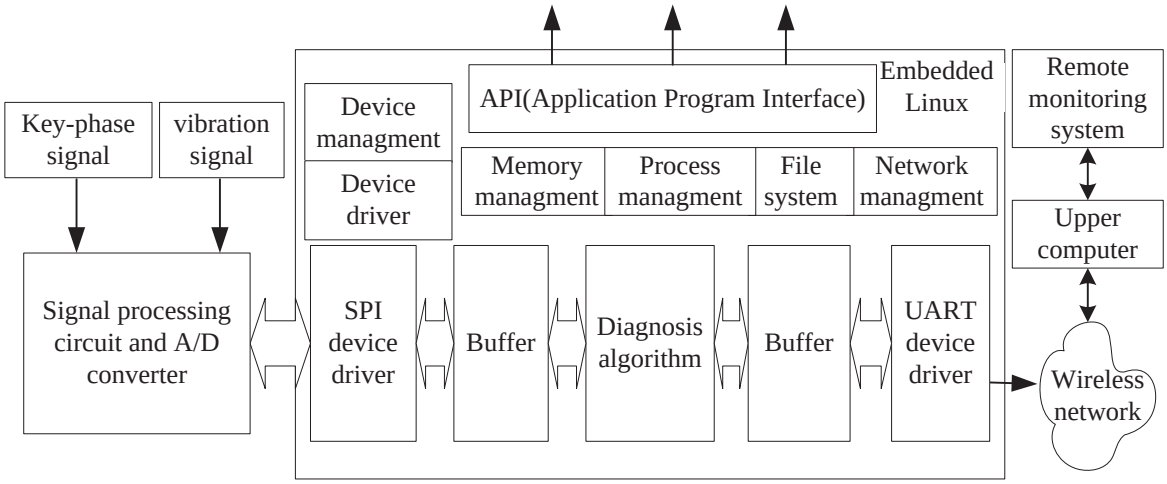

Fig. 3 Software structure of intelligent data unit

As is shown in Fig.3, each task is abstracted as a child process controlled by main process. Application program interfaces are provided by Linux for process scheduling, inter process communications and synchronization [9]. Data flow of lower layer can be simply controlled by process management.

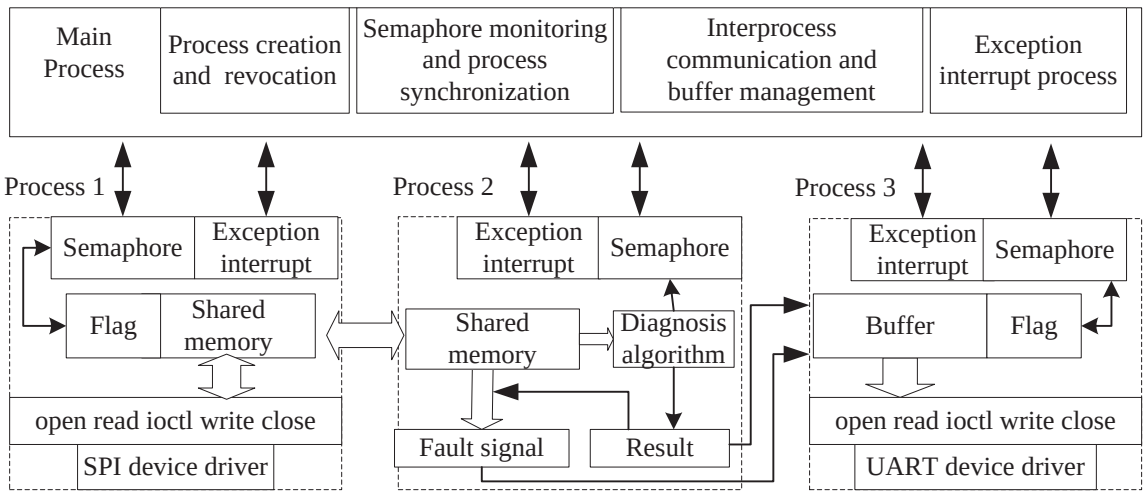

Fig. 4 Multi-process structure

As is shown in Fig.4, multi-process structure contains main process and child processes including process 1, process 2 and process 3 [10]. Detail function of each process is described as follows:

a) Data manipulation, such as vibration data reading and caching are achieved by Process 1. SPI transfer protocol is used for vibration data reading, and operations of SPI are provided by API of its device driver, such as open(),read(),ioctl(),write(),close() and etc. [11]. During vibration data reading procedure, the flag of integral period sampling provided by Key-phase signal, would inform process 1 to adjust the size of buffer for data caching. Meanwhile, the task of storing vibration data into buffer is all in the charge of DMA controller. Semaphore would be sent by process 1 to main process when buffer is in null or full status, thus data stream among each process can be balanced by main process. When process 1 is in error state, main process will be informed by high priority interrupt.
b) The algorithm of condition recognition and fault diagnosis is achieved by Process 2. Base on the algorithm principle, characteristic parameters of vibration signal are calculated and analyzed in time-domain and frequency-domain. Process 2 gets vibration data from process 1 by sharing memory unit of the buffer. The diagnosis algorithm of intelligent data unit is described in detail in next part. After intelligent diagnosis, the results of condition recognition and fault diagnosis would be transferred to buffer 3 in process 3.
c) Process 3 is responsible for results transmitting wirelessly. UART is selected as the data transfer protocol between ARM and wireless module. And operations of UART are provided by API of UART device driver. Based on the format definition of wireless data frame, data packing and encryption are also tasks of process 3. Main process will be informed by semaphore to balance data transmitting speed of UART and the wireless module.
d) Main process is the controller of the three child processes above. By calling function fork() or exit(), Process 1-3 can be created or revoked. The abnormal state of each child process is also monitored by main process. Meanwhile, P and V semaphores are used for synchronizing each child process.

3.3 Algorithm of Condition Recognition and Fault Diagnosis

The algorithm of condition recognition and fault diagnosis contains the part of recognition of rolling bearings and the part of fault diagnosis. Primarily, intelligent data unit calculates the time-domain characteristic parameters of collected vibration signal. By comparison with thresholds of the parameters, normal state or abnormal state of rolling bearings can be recognized. But before it is implemented in practical application, intelligent data unit should be trained with the guide of expertise to get suitable thresholds of the characteristic parameters.

Five time-domain characteristic parameters listed in Eq.(1-5) are Peak-peak value, Absolute peak, RMS, Kurtosis and Peak index, as follows:

$$X_{peak} = \max(x(t)) - \min(x(t)) \tag{1}$$

$$X_{abs} = \max|x(t)| \tag{2}$$

$$X_{rms} = \sqrt{\frac{1}{T}\int_0^T x^2(t)dt} \tag{3}$$

$$\alpha_4 = \int_{-\infty}^{+\infty} x^4 p(x)dx \tag{4}$$

$$C = \frac{X_{peak}}{X_{rms}} \tag{5}$$

In Eq.(1-5), $x(t)$ is the vibration response signal of a certain feature point, which is located on the vibration model of rotating equipment. T is the sampling time, and $p(x)$ is the probability density function of $x(t)$ [12].

By comparison with thresholds of the characteristic parameters, the intelligent data unit can recognize the abnormal conditions of rolling bearings. During practical application, if the thresholds were exceeded, flag of abnormal condition would be set and further diagnosis in frequency-domain would be executed. The characteristic parameters of frequency-domain used in intelligent data unit are fault characteristic frequency of inner-race, fault characteristic frequency of outer-race and fault characteristic frequency of rolling, as follows:

$$f_i = \frac{1}{2} f_n (1 + \frac{d}{D_m} \cos\alpha) Z \tag{6}$$

$$f_o = \frac{1}{2} f_n (1 - \frac{d}{D_m} \cos\alpha) Z \tag{7}$$

$$f_{RS} = \frac{1}{2} f_n (1 - \frac{d^2}{D_m{}^2} \cos^2\alpha) \frac{D_m}{d} \tag{8}$$

In Eq.(6-8), f_n is the rotating frequency, Z is the number of rolling element, α is the bearing pressure angle, D_m is the diameter of bearing, and d is the diameter of rolling element [13].

According to the specific features of rolling bearings, f_i , f_o and f_{RS} used as the standard for the frequency-domain analysis can be calculated ahead of time. If flag of abnormal condition were set, Fourier transform would be executed for further diagnosis in the frequency-domain. If energy value increased evidently at the point of the fault characteristic frequency or its multiple frequencies in the signal spectrum, specific fault could be recognized correctly.

After the analysis of the vibration signals in the time-domain and the frequency-domain is accomplished, the characteristic parameters of rolling bearings will be sent to the upper computer. Meanwhile, detail information of fault vibration data will be sent additionally if the result of condition recognition is abnormal.

4. Experiments and Results

In order to verify the effectiveness of the intelligent data unit, two kinds of rolling bearing were utilized in the experiment: a bearing without fault and one with outer-race defect. The specific type of the rolling bearings is NSK206. Roller diameter of NSK206 is 6.5mm, the number of roller is 10, pitch circle diameter is 32mm, and contact angle is 0 rad. The rotating speed of each roller bearing is set at 1100 rpm, and the calculated characteristic frequency of outer-race defect is 73 Hz.

The time-domain waveforms of normal signal and outer-race defect signal are shown in Fig.5 and Fig.6, respectively.

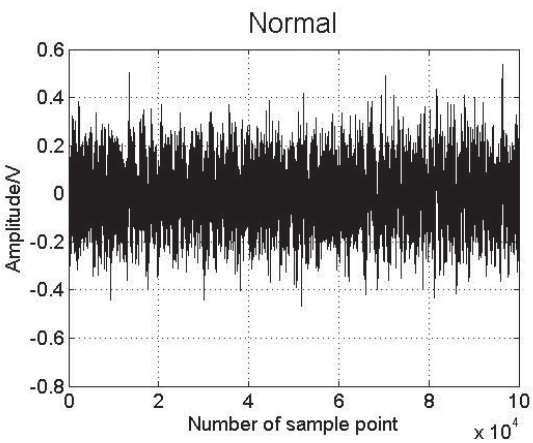

Fig. 5 Waveform of normal signal

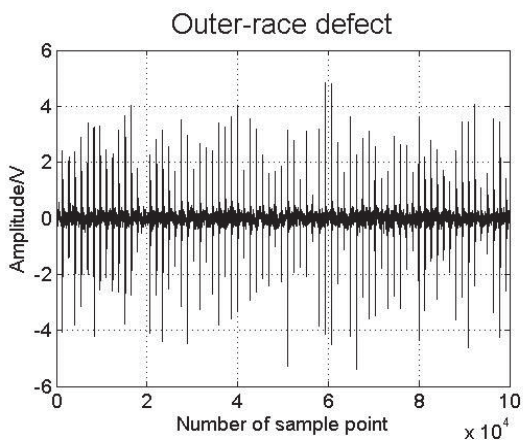

Fig. 6 Waveform of outer-race defect signal

Table 1 Characteristic parameters of normal signal

Test NO.	Peak-peak value	Absolute peak	RMS	Kurtosis	Peak index
1	0.945	0.503	0.101	3.176	4.948
2	0.811	0.439	0.102	2.968	4.290
3	0.886	0.467	0.099	3.071	4.683
4	0.911	0.492	0.108	3.008	4.523
5	0.970	0.538	0.116	3.400	4.614

Table 2 Characteristic parameters of outer-race defect signal

Test NO.	Peak-peak value	Absolute peak	RMS	Kurtosis	Peak index
1	8.238	4.204	0.301	40.191	13.924
2	8.090	4.478	0.310	42.110	14.427
3	10.122	5.294	0.280	48.583	18.861
4	10.187	5.384	0.337	46.487	15.948
5	8.674	4.620	0.280	47.631	16.444

Table 3 Threshold of each characteristic parameter

Peak-peak value	Absolute peak	RMS	Kurtosis	Peak index
2.715	1.465	0.318	9.375	13.837

The vibration data of each status was processed in embedded Linux intelligent data unit, and 5 characteristic parameters were calculated, respectively, shown in Table.1 and Table.2. According to ISO 10816 and ISO 7919, standards of mechanical fault diagnosis, thresholds of parameters are set at 3 times of the mean values in normal condition relatively [14]. And threshold of each parameter is shown in Table 3.

According to the thresholds in Table 3, five groups of data in Table.1 are all within the threshold value range, so the recognition results are all normal. Peak value and absolute peak value in Table.2 exceed the threshold value range largely, and kurtosis and peak index also go beyond corresponding range, so the processing result of intelligent data unit to this type of bearing status is abnormal. Signal in time-domain would be transformed to signal in frequency-domain by FFT (Fast Fourier Transform) algorithm for further analysis [15]. In this experiment, the frequency with maximum of power picked out by intelligent data unit was 72.48Hz, corresponding to the characteristic frequency of outer-race defect 73Hz. Thus the result of fault diagnosis was outer-race defect, and collected fault signals were sent to upper computer. After fault signals were received by upper computer, power spectrum was plotted. As is shown in Fig. 7, the energy protrudes evidently in the positions of 72.48Hz and its multiplication, confirming that the result of intelligent data unit is correct.

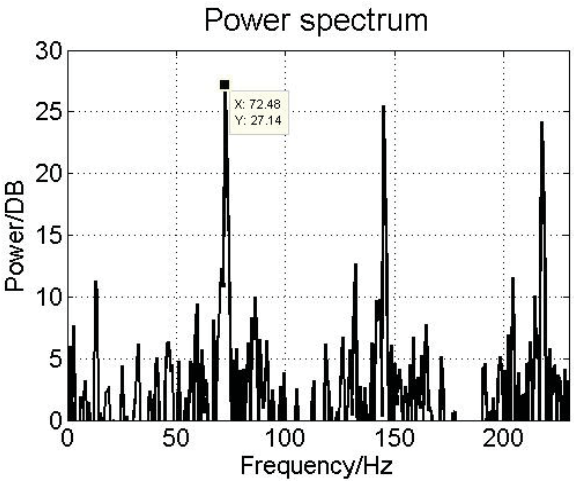

Fig. 7 Power spectrum of outer-race defect signal

According to the experiment above, condition recognition and fault diagnosis of rolling bearings could be effectively completed with high accuracy by intelligent data unit based on embedded Linux. Meanwhile, the results could be sent to upper computer in real-time for further verification and judgment, confirming accuracy and effectiveness.

5. Conclusion

To conclude, intelligent and instantaneous data unit based on Linux system for rolling bearings condition monitoring and fault diagnosis is introduced in the paper, as a research direction on intelligent equipments. It is fully exerted that the strong processing ability of ARM9 and the advantage of Linux on parallel processes and

process scheduling. Based on the design of embedded technology and wireless communication technology, structure of intelligent data unit is simplified, but stability and intelligence are enhanced. Experiments verified that vibration signals could be instantaneously acquired and processed by the intelligent data unit. Meanwhile, the goal of condition recognition and fault diagnosis could be achieved by comparing characteristic parameters extracted from vibration signals. Furthermore, upper computer connected with intelligent data unit through the wireless network, could make further verification and anticipation, ensuring high accuracy and effectiveness of the entire detection system.

Acknowledgment

This project is supported by National Program on Key Basic Research Project (Grant No. 2012CB026000), National Natural Science Foundation of China (Grant No.51075023, 51135001) and National Key Technologies R&D Program (Grant No. 2011BAK06B02), and Fundamental Research Funds for the Central Universities (Grant No. ZZ1124) and SRF for ROCS, SEM.

References

[1] Q. G Shen and S. Y Zheng. *Equipment Fault Diagnosis*, Chemical Industry Press, 2005.

[2] E. G Peng, Z. L Liu. Research on The Embedded Condition Monitoring and Fault Diagnosis System for The Rotation Machine, *Applied Mechanics and Materials,* Vol. 84-85, pp. 544-547, 2011.

[3] F. Y Xu, J. Z Hu, M. P Jia, etc. Recent Progress of Vibration Analysis on Fault Diagnosis for Rolling Bearing, *Journal of Southeast University (Natural Science Edition),* Vol. 34, No. 6, pp.761-765, 2004.

[4] Q. H Tang, L. N Fu and S. A Zhu. Bearing Testing and Fault Diagnosis System Based on DSP and ARM, *Mechanical & Electrical Engineering Magazine,* Vol. 23, No. 2, pp. 1-4, 2006.

[5] M. Lynch, Zakrzewski, Radoslaw, etc. Wireless Sensing for Bearing Monitoring and Rotor Balance, *Annual Forum Proceedings - AHS International,* Vol. 3, pp. 1729-1735, 2011.

[6] J. Cheng, Y. M Wei, X. Xiong, etc. Design and Development of Embedded Turbine Supervisory Instruments Based on ARM and Linux, *Applied Mechanics and Materials,* Vol. 80, pp. 1237-1243, 2011.

[7] H. H Wang. *The Development Guide of Embedded System Linux (ARM Platform),* Electronic Industry Press, 2009.

[8] S. S Dai and X. H Yuan. Application of DMA in Realtime Image Processing, *Journal of Chongqing University,* Vol. 26, No. 12, pp. 22-24, 2003.

[9] M. Q Hu, W. Gao and M. Zhong. *The Operating System Course and Experiment*, Tsinghua University Press, 2007.

[10] H. Q Zhan, X. H Song and T. X Gu. Software Design of Intelligent Instruments Based on Multi-tasks and Multi-threads, *Instrument Technique and Sensor,* No. 11, pp. 20-24, 2004.

[11] J. Corbet. *Linux Device Drivers(3rd Edition)* , O'Reilly & Associates Inc., 2005.

[12] X. L Li, Y. P Zhang, M. L Cao, etc. Development of Fault Detection and Diagnosis Technology of Rolling Bearing , *Engineering and Test,* Vol. 49 , No. 4, pp.1-5, 2009.

[13] C. Z Chen, L. X Hu, B. Zhou, etc. *Equipment Vibration Analysis and Fault Diagnosis Technology*, Science Press, 2007.

[14] D. C Tong. Standard Establishment of Vibration and Diagnosis, *Construction Machinery and Maintenance,* vol . 5, pp. 110-111, 2001.

[15] P. Q Cheng. *Digital Signal Processing Course*, Tsinghua University Press, 2007.

Copyright © 2012 DET Corp., Japan All Rights Reserved
International Journal of Comprehensive Engineering
Part A, 2(2), 142-148, 2013
Doi: 10.14270/IJCE2013.2.2.a142
Regular paper

ISSN 2186-2680
e-ISSN 2186-2656
www.iace-journal.org

Application of the multifractal method to the feature extraction of megawatt wind turbine main bearing

Ziqiang Sun, Changzheng Chen

School of Mechanical Engineering, Shenyang University of Technology, Shenyang 110870, China

Abstract: The fault signal problems of wind turbine are non-linear and non-stationary, thus it is difficult to obtain the obvious fault features. The development of non-linear dynamic theory brought a new method, multifractal method, for recognizing and predicting the complex non-linear dynamic behavior. The singularity spectrum obtained from the multifractal method is a comprehensive reflection of the distribution of the singularities of signals. In this study, the faults of megawatt wind turbine main bearing are investigated by the multifractal method. The real vibration signals collected from the main bearing are analyzed using the singularity spectrum. The results show that the vibration signals of the inner race fault have the strongest singularity. It means that the multifractal method is effective to extract the fault features and can reflect the real operating conditions of the megawatt wind turbine.

Keywords: Wind Turbine, Main Bearing, Multifractal Method, Feature Extraction.

Received: May 25,2012 / Accepted: Feb. 20,2013 / Published: Jul. 5,2013

1. Introduction

Wind turbines are popular energy harnessing devices that produce electrical power derived from the wind. One of the wind turbine key components is roller bearings. Bearing problems account for between 21% and 95%, respectively, of all failures in electrical machines, and for induction machines of the size and type used in wind turbines this figure is probably >45% [1]. Therefore, fault prediction or sufficiently fast fault diagnosis for the bearing is needed. Fault diagnosis can reduce the cost for maintenance in the future. Many techniques have been applied on the detection and diagnosis of bearing defects, such as wavelet transform, empirical mode decomposition, and time–frequency representation, etc [2-4].

Wind turbine is typical low speed rotating machinery, and it rotates at approximately 40 rpm. Generally, wind turbines are massive in size and heavy-load, consequently when defects begin to occur the resulting vibration is often very low. The vibration signals of wind turbine are non-linear and the noise signal is so strong that it is difficult to recognize the fault vibration signals.

Apart from those widely used techniques mentioned above, fractal dimension is a promising approach to non-linear dynamics [5-7]. The fractal dimension is a useful tool to characterize the nonlinearity and complexity of dynamic system. Recently, fractal dimension is broadly applied to the field of fault diagnosis [8-11].

However, single fractal approach only can reflect the overall irregularity of signals, but cannot describe the local scaling properties [12, 13]. An alternative way, multifractal method which can provide more information of signals, was presented systematically by Grassberger [14] and Hentschel, Procaccia et al [15]. Based on multifractal method, the local conditions of fractal objects are described more precisely; the relationship of local scaling properties and the overall characteristics is established.

The multifractal method has been applied to a large number of empirical as well as theoretical studies of a wide variety of problems. It was also used in bearing fault diagnosis [16]. To our knowledge, the multifractal method has never been used for wind turbine main bearing fault diagnosis in literature.

In this paper, the multifractal method is used to analyze the vibration signals of three typical faults of the wind turbine main bearing. Section 2 gives a brief review of the multifractal method. In Section 3 the real data of the

main bearing used in the wind turbines is studied by the multifractal spectrum. The typical fault features are extracted from the multifractal spectrum. Finally, a conclusion is summarized in Section 4.

2. The multifractal method

During monitoring the vibration signals of the wind turbine, the vibration time domain waveforms of the main bearing have self-similar characteristic in a certain time domain length. The vibration velocity time domain waveforms of the main bearing in the vertical direction of the bearing block, colleted by the Germany VIBXPERT expert FFT data collection and analyze apparatus at different sample frequencies, are shown in Fig. 1. From the figure, it can be seen that the time domain have self-similar characteristic.

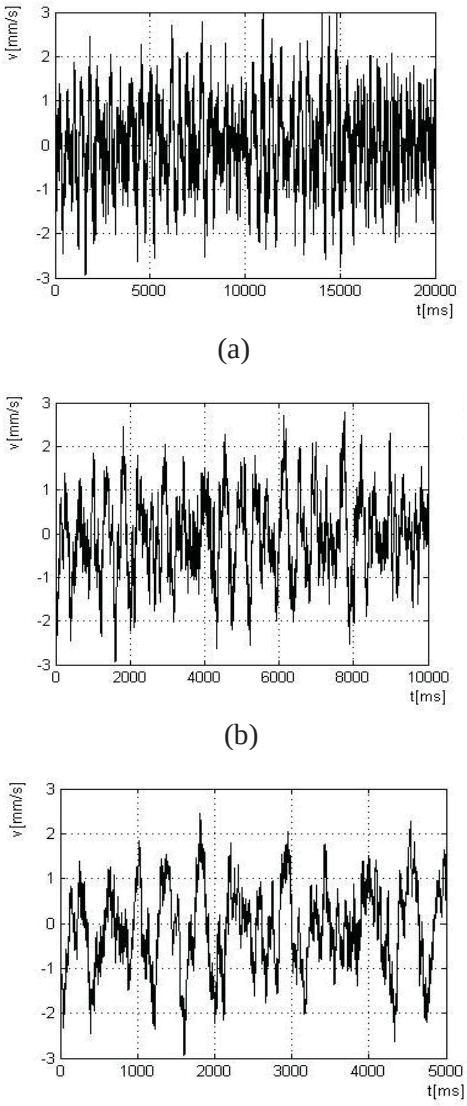

Fig. 1 Time spectrums of main bearing at different sampling frequencies. (a) 16 kHz, (b) 8 kHz, (c) 4 kHz.

One can adopt the capacity dimension, information dimension, and correlation dimension to descript the vibration signal of the main bearing. These methods have been used on the fault diagnosis. However, when to reflect the fractal dimension of the wind turbine main bearing vibration time domain waveform, it is not enough to use the single and scale exponent lying on the whole character. It is relatively rough for the identification of the wind turbine main bearing working state. The multifractal defined on the fractal, is assemble of the singularity measure which has multi-scale exponent. It depicts the distribution of the sub-measure on the support, i.e. a spectrum function is used to depict the characteristic of the different fractal scales.

Consider the local behavior of the system and the different level characteristics of the fractal body during the molding process:

$$P_i = L_i^{\alpha}, \tag{1}$$

$$\alpha_i = \lim_{L_i \to 0} \frac{\ln P_i}{\ln L_i}, \tag{2}$$

where α_i is fractal dimension of some fractal micro-region, named local fractal dimension. Its magnitude reflects the magnitude of the generating probability of the micro-region. P_i is growth probability of the fractal body growth interface in the micro-region. L_i is the size of the micro-region. Because there are a large number of the micro-regions, α_i can compose infinite sequence spectrum, and one can use $f(\alpha)$ and α describe the multifractal. Obviously, it is difficult to measure P_i in the real project. Using the expression of the moment in the statistic physics to do the weighing summation of the probability in Eq. (1) by the equation

$$\sum_{i=1}^{N} P_i^q = \sum_{i=1}^{N} (L_i)^{\alpha_i q} = X(q). \tag{3}$$

Define the q-order information dimension as D_q

$$D_q = \lim_{L \to 0} \frac{1}{q-1} \cdot \frac{\ln X(q)}{\ln L} = D(q). \tag{4}$$

The relation of the parameters mentioned above is

$$D_q = \frac{1}{q-1} \cdot \left[q\alpha - f(\alpha) \right], \tag{5}$$

or

$$f(\alpha) = q\alpha - (q-1) D_q. \tag{6}$$

Different scale fractal can be used to describe the distribution of the non-uniform random probability of the vibration signals of the wind turbine main bearing at different levels. According to the multifractal spectrum α-$f(\alpha)$, the multiscale fractal characteristic can be found.

3. Calculation process and result analysis

The research reported in this paper is performed with industrial data collected at operating wind turbines. Our data are from the main bearings of the wind turbine with a rated power of 3MW. The measurements are performed by Germany VIBXPERT Expert FFT Data Collection and Signal Analytic Instrument with a sampling frequency 16 kHz.

Assume that $\{x_k, k=1,2,...N\}$ is the time series of one bearing, put it into m-dimension Euclidean space R_m, a assemble can be obtained. The assemble can be described as

$$X_{m\times l} = \begin{bmatrix} x(t_1) & x(t_2) & \cdots & x(t_l) \\ x(t_1+\tau) & x(t_2+\tau) & \cdots & x(t_l+\tau) \\ \vdots & \vdots & \vdots & \vdots \\ x(t_n+(m+1)\tau) & x(t_2+(m+1)\tau) & \cdots & x(t_l+(m+1)\tau) \end{bmatrix}. \tag{7}$$

During the process of the reconstruct the phase space of the time series, embedding dimension refers to the least space progression. In 1980, Tackcns proved the embedding theorem of the embedding space dimension:

$$m > 2D_A + 1, \tag{8}$$

where m is the dimension of the embedding space, D_A is the space dimension in which the attactors of the original state space. Generally, the embedding dimension is chosen as m>20, for making the correlation dimension stable. In this paper, m=25. Calculate the distance of the random two points in matrix X_{ml}:

$$r_{ij} = d\left(X_i, X_j\right) = \left[\sum_{i=0}^{m-1}\left(x_{i+lr} - x_{j+lr}\right)^2\right]^{\frac{1}{2}}. \tag{9}$$

All the distance between the space vectors can construct a $k \times k$ matrix R. So the q-order correlation integral can be defined as:

$$C_q\left(r\right) = \left\{\frac{1}{N_m}\sum_{j=1}^{N_m}\left[\frac{1}{N_m}\sum_{i=0}^{N_m} H\left(r - r_{ij}\right)\right]^{q-1}\right\}^{\frac{1}{q-1}}, \tag{10}$$

where H is Heabiside function. The multifractal spectrum of the time series can be calculated through, $\{y_k, k=1,2,\ldots N\}$ is q-order correlation integral:

$$D_q = \lim_{r \to 0}\frac{\ln C_q\left(r\right)}{\ln r}. \tag{11}$$

The waveforms of the vibration signal of four main bearing running states, i.e. normal condition, ball fault, inner race fault and outer race fault, are shown in Fig. 2.

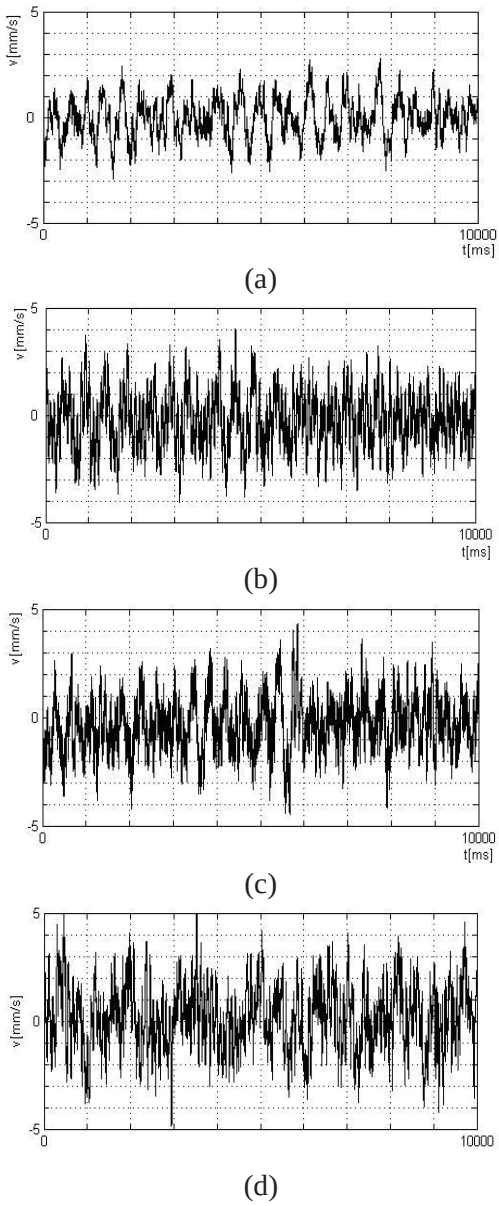

Fig. 2 Vibration signals of the main bearing: (a) normal state, (b) ball fault, (c) inner race fault, and (d) outer race fault.

Chose the iterative order as $\Delta q = 0.02$, the singularity spectrums (as shown in Fig. 3) are calculated based on the method mentioned above.

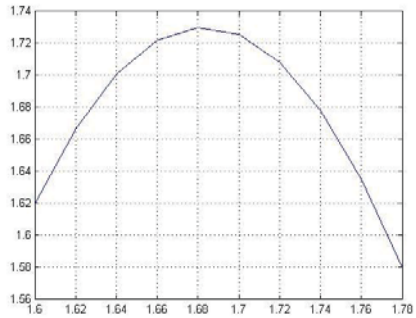

(a)

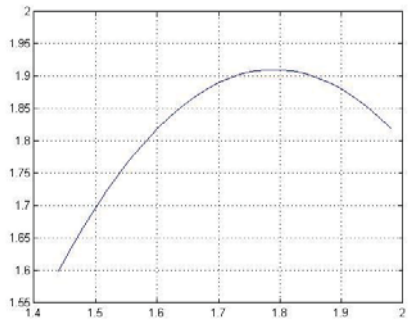

(b)

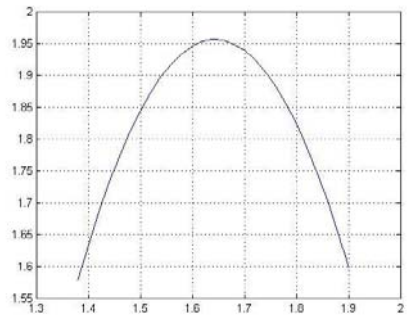

(c)

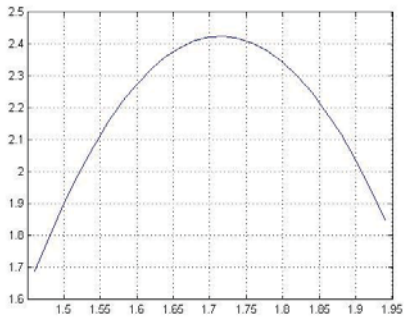

(d)

Fig. 3 The multifractal spectrum of the vibration signal: (a) normal state, (b) ball fault, (c) inner race fault, and (d) outer race fault.

From Fig. 3, it can be seen that there is significant difference in the multifractal spectrums of the bearing under different working state. When the fault occurs in the bearing, the width and height of the spectrum change obviously.

The strength of multifractality can be characterized by the span of the multifractal singularity strength function, that is, $\Delta\alpha=\alpha_{max} - \alpha_{min}$. If $\Delta\alpha$ is large, the return series owns multifractality, while the return series is

almost monofractal if $\Delta\alpha$ gets close to zero [17]. $\Delta\alpha$ reflects the degree of fluctuation in vibration signal. The α_{max}, $\Delta\alpha$ and f_{max} calculated from Fig. 3 are shown in Table I.

Table 1 the main bearing signal parameters of multifractal spectrum

State	$\Delta\alpha$	α_{min}	f_{max}
Normal	0.18	1.60	1.73
Ball fault	0.58	1.43	1.91
Inner race fault	0.52	1.37	1.96
Outer race fault	0.48	1.46	2.41

The $\Delta\alpha$ of the three faults are all highter than the normal. These indicate that the vibration signals of the fault bearing are more irregular than the normal bearing. For the ball fault and the inner race fault, their $\Delta\alpha$ are relative larger than the outer race fault. The valve of $\Delta\alpha$ for the ball fault is 0.58, and for the inner race fault is 0.52. Those reflect that the vibration signals of the ball and inner race fault have strong irregularity and are more complicated than the signals of the outer race fault.

The α_{min} of the outer race fault is smaller than the normal and bigger than the other two faults, which reflects weaker multifractality or even monofractality. It means that the vibration signals of the outer race fault has strong regularity and is smooth.

The inner race and outer race fault signal's f_{max} are all bigger than the normal and the ball fault. The result indicates that the changing speed of high and low peak value in inner race and outer race fault signals are faster and the vibration amplitude are larger, so the vibration in inner race and outer race fault signal is more tempestuously.

4. Conclusions

In this paper, the multifractal method is used in main bearing fault detection of megawatt wind turbines. The multifractal features of non-linear signals are extracted based on the multifractal spectrum. The important parameters, such as α_{max}, $\Delta\alpha$ and f_{max} are obtained from the spectrum. Those parameters are applied to identify the main bearing faults.

The vibration signals of four bearing working conditions, including the normal, the ball fault, the inner race fault and the outer race fault, are analyzed. The results show that the signal of the inner race fault is the most irregular, which change acutely, and so are the most complicated. According to the multifractal method, the main bearing running states are distinguished effectively. This research provides an effective method for feature analysis of wind turbine faults.

Acknowledgements

This study was supported by the National Natural Science Foundation of China, under project number 50975180.

References

[1] S. J. Watson, B. J. Xiang, W. Yang, P. J. Tavner and C. J. Crabtree. Condition Monitoring of the Power Output of Wind Turbine Generators Using Wavelets, *IEEE Transactions on Energy Conversion*, Vol. 25, No. 3, pp. 715-720, Sep. 2010.

[2] A. K. S. Jardine, D. Lin and D. Banjevic. A Review on Machinery Diagnostics and Prognostics Implementing Condition-Based Maintenance, *Mechanical Systems and Signal Processing*, Vol. 20, pp. 1483–1510, 2006.

[3] N. Tandon and A. Choudhury. A Review of Vibration and Acoustic Measurement Methods for the Detection of Defects in Rolling Element Bearings, *Tribology International*, Vol. 32, pp. 469-480, 1999.

[4] J. Yu. Bearing Performance Degradation Assessment Using Locality Preserving Projections, *Expert Systems with Applications*, Vol. 38, pp. 7440-7450, 2011.

[5] B. B. Mandelbrot. *The Fractal Geometry of Nature*, W. H. Freeman, San Francisco, 1982.

[6] K. Falconer. *Fractal Geometry: Mathematical Foundations and Applications, second ed.*, Wiley , Chichester, 2003.

[7] K. Falconer. *The Geometry of Fractal Set*, Cambridge University Press, Cambridge, 1985.

[8] D. Logan and J. Mathew. Using the Correlation Dimension for Vibration Fault Diagnosis of Rolling Element Bearing—I. Basic Concepts, *Mechanical Systems and Signal Processing*, Vol. 10, pp. 241-250, 1996.

[9] J. D. Jiang, J. Chen and L. S. Qu. The Application of Correlation Dimension in Gear Box Condition Monitoring, *Journal of Sound and Vibration*, Vol. 223, pp. 529-541, 1999.

[10] J. Yang, Y. Zhang and Y. Zhu, Intelligent Fault Diagnosis of Rolling Element Bearing Based on SVMs and Fractal Dimension, *Mechanical Systems and Signal Processing*, Vol. 21, pp. 2012-2024, 2007.

[11] D. Jiang, C. E, W. Ni, Fractal Geometry and Its Application on Vibration Faults Diagnosis for Rotating Machinery, Key Engineering Materials, Vol. 245-246, pp. 265-272, 2003.

[12] Z. K. Peng, Y. Y. He, Q. Lu, et al., Wavelet Multifractal Spectrum: Application to Analysis Vibration Signals, *Chinese Journal of Mechanical Engineering*, Vol. 38, pp. 59-63, 2002.

[13] J. Hu, L. Zhang, W. Ling and Z. Wang, Incipient Mechanical Fault Detection Based on Multifractal and MTS Methods, *Petroleum Science*, Vol. 6, pp. 208-216, 2009.

[14] P. Grassberger. Generalized Dimensions of Strange Attractors, *Physics Letters A*, vol. 97, pp. 227-320, 1983.

[15] H. Hentschel and I. Procaccia. The Infinite Number of Generalized Dimensions of Fractals and Strange Attractors, *Physica D: Nonlinear Phenomena*, Vol. 8, pp. 435-444, 1983.

[16] F. V. Nelwamondo, T. Marwala and U. Mahola. Early Classifications of Bearing Faults Using Hidden Markov Models, Gaussian Mixture Models, Mel-Frequency Cepstral Coefficients and Fractals, *International Journal of Innovative Computing, Information and Control*, Vol. 2 , pp. 1281-1299, 2006.

[17] G. Gu and W. Zhou. Detrending Moving Average Algorithm for Multifractals, *Physical Review E*, Vol. 82, pp. 011136, 2010.

Copyright © 2012 DET Corp., Japan All Rights Reserved
International Journal of Comprehensive Engineering
Part B, 2(2), 149-160, 2013
Doi: 10.14270/IJCE2013.2.2.b149
Regular paper

ISSN 2186-2680
e-ISSN 2186-2656
www.iace-journal.org

Sequential Diagnosis using Support Vector Machine and Relative Ratio Symptom Parameters for Identifying Early-stage Structural Faults of Rotating Machinery

Hongtao Xue [1], Huaqing Wang [2] and Peng Chen [1, #]

[1] Graduate School of Bioresources, Mie University, 1577 Kurimamachiya-cho, Tsu-shi, Mie, 514-8507, Japan
[2] School of Mechanical & Electrical Engineering, Beijing University of Chemical Technology, Beijing, 100029, China

[#] Corresponding author: chen@bio.mie-u.ac.jp; Tel & Fax: +81-59-231-9592

Abstract: This study proposes a new sequential diagnosis method based on relative ratio symptom parameters (RRSPs) and support vector machines (SVMs) for identifying early-stage structural faults of rotating machinery. RRSPs are defined to reflect the characteristics from early-stage structural faults of rotating machinery, and distinction index (DI) is used to select the higher sensitive RRSPs for distinguishing two states. Moreover, the optimal hyper-plane of two states is automatically obtained using a SVM, and then using multi-SVMs, the system of sequential diagnosis is built to detect many faults and identify fault types from rotating machinery in early stage. The proposed method has been applied to detect structural faults from rotating machinery in early stage, and the efficiency of the method has been verified using practical examples.

Keywords: Sequential Diagnosis, Support Vector Machine, Relative Ratio Symptom Parameter, Distinction Index, Early-stage Fault, Optimal Hyper-plane.

Received: May 25,2012 / Accepted: Feb. 20,2013 / Published: Jul. 5,2013

1. Introduction

In a real plant, unbalanced, looseness, misalignment, etc. states are the common faults and easily occur. These faults are normally seen and show respective characteristics in the low frequency band, so these faults in the low frequency band are called “structural faults” [1]. Structural faults not only impact on equipment performance or product quality, but also add an excessive stress to circumference parts, such as bearing and gear, thereby causing secondary faults. So it is a very important issue that structural faults are diagnosed in early stage [2]. And then the fault caused in early stage is called “early-stage fault”. The degree of early-stage fault is slight, the abnormal characteristics are unclear.

In the field of condition monitoring and machinery diagnosis, symptom parameter (SP) is extremely important as an effective tool. If good SPs that sensitively reflect the feature of the machine states can be found, automatic diagnosis for mechanical failure is possible [3]. However, it is not easy to find effective SPs for early-stage faults. And traditional intelligent methods such as neural networks (NN), which are based on statistical learning, require a large number of training samples. In most cases of practical machinery diagnosis, measured signals are not sufficient for conditioning the learning data [4~7]. Moreover, these methods often do not converge during the learning phase of these networks [3, 8].

To solve these problems, after analyzing the features from structural faults of rotating machinery, relative ratio symptom parameters (RRSPs) are defined to identify structural faults of rotating machinery. At the same time, SVMs are adopted as a novel intelligent classifier. SVMs use a structural risk minimization principle to minimize an upper bound based on an expected risk, which leads to a better generalization performance. This study proposes a new intelligent diagnosis method based on RRSPs and SVMs in early stage using sequential diagnosis. These proposed methods have been applied to diagnose structural faults of rotating machinery in early stage, and verification results will show that the methods are accurate and practical.

2. Relative Ratio Symptom Parameters (RRSPs)

2.1 Distinctive Characteristics of Structural Faults

Structural faults have many categories. However the rotational frequency and these high-order harmonic components of structural faults are not only more prominent than in normal states, but these frequencies and components also show respective characteristics, even though early-stage faults [1].

Generally, in the unbalanced state, the spectrum captures a rotating frequency f_r that is the main and dominating 2nd-order harmonic component; this harmonic has sometimes appeared clearly; however, high-order harmonic components of a rotational frequency $i \cdot f_r (i \geq 3)$ have hardly appeared. Moreover, the level of the vibration is related to the channel measuring the signal, and the amplitude is proportional to the second power of the rotational speed. In contrast, the vibration level in the horizontal direction is the strongest, and the vibration level in the axial direction is a little weaker.

When the looseness state is occurring, the influence from the rotational speed is large, and the noise level is also comparatively large, and there is a possibility that impact will occur. Therefore, the high-order harmonic components of rotational frequency appear with significant amplitude.

While in the misalignment state in the frequency components, $2f_r$, $3f_r$ or $4f_r$, … appear, but then $2f_r$, $3f_r$ or $4f_r$ is significant and dominating, and the amplitude of f_r is minor. Compared with the unbalanced state, the influence of the amplitude from the rotational speed is much lower. However the vibrating level of the axial direction is larger.

On top of these faults, bent shaft, shaft crack also show those characteristics in the low frequency band. The rotational frequencies and their high-order harmonic components can demonstrate the features of the vibration signals and reflect structural faults.

2.2 Relative Ratio Symptom Parameters (RRSPs)

According to the distinctive characteristics of structural faults, relative ratio symptom parameters (RRSPs) are defined as in Eq. (1) ~ (10) for diagnosing structural faults of rotating machinery, so RRSPs are also called "exclusive symptom parameters: ESPs" for structural faults.

$$P_1 = \frac{P_d(f_r) \Big/ \sum_{i=2}^{20} P_d(i \cdot f_r)}{P_n(f_r) \Big/ \sum_{i=2}^{20} P_n(i \cdot f_r)} \tag{1}$$

$$P_2 = \frac{P_d(2f_r)/P_d(f_r)}{P_n(2f_r)/P_n(f_r)} \tag{2}$$

$$P_3 = \frac{P_d(3f_r)/P_d(f_r)}{P_n(3f_r)/P_n(f_r)} \tag{3}$$

$$P_4 = \frac{\sum_{i=4}^{10} P_d(i \cdot f_r) \Big/ P_d(f_r)}{\sum_{i=4}^{10} P_n(i \cdot f_r) \Big/ P_n(f_r)} \tag{4}$$

Here, f_r is the rotating frequency. $P_n(f_r)$, $P_d(f_r)$ are the spectrum value at f_r in normal state and abnormal state respectively, $P_n(i \cdot f_r)$ and $P_d(i \cdot f_r)$ are the high-order harmonic value at $i \cdot f_r$ in normal and abnormal state respectively.

$$P_5 = \frac{P_d(f_r)/P_n(f_r)}{|N_d - N_n|/100} \tag{5}$$

Here, N_n and N_d are the rotation speed of the machine in normal and abnormal state respectively.

$$P_6 = \frac{\sum_{>0.6kH}^{<1.5kH} P_d(f) \Big/ \sum_{<0.6kH} P_d(f)}{\sum_{>0.6kH}^{<1.5kH} P_n(f) \Big/ \sum_{<0.6kH} P_n(f)} \tag{6}$$

$$P_7 = \frac{\sum_{i \neq i \cdot f_r}^{f_i > 6 f_r} P_d(f_i) \Big/ \sum_{i=1}^{6} P_d(i \cdot f_r)}{\sum_{i \neq i \cdot f_r}^{f_i > 6 f_r} P_n(f_i) \Big/ \sum_{i=1}^{6} P_n(i \cdot f_r)} \tag{7}$$

$$P_8 = \frac{A_{ad} / A_{rd}}{A_{an} / A_{rn}} \tag{8}$$

Here, A_{an} and A_{rn} are the vibration level of shaft direction and radial direction in normal state respectively, A_{ad} and A_{rd} are the vibration level of shaft direction and radial direction in abnormal state respectively. (Vibration level is Standard deviation or root mean square value .etc.)

$$P_9 = \frac{A_{vd} / A_{hd}}{A_{vn} / A_{hn}} \tag{9}$$

Here, A_{vn} and A_{hn} are the vibration level of vertical direction and horizontal direction in normal state respectively, A_{vd} and A_{hd} are the vibration level of vertical direction and horizontal direction in abnormal state respectively.

$$P_{10} = \beta_d - \beta_n \tag{10}$$

Here, β_n and β_d are the skewness in normal state and abnormal state respectively.

3. Intelligent Diagnosis using SVMs and RRSPs

3.1 Support Vector Machines (SVMs)

SVMs are a relatively new computational learning method based on the statistical learning theory, and the basic idea is to create an optimal hyper-plane, as shown in Fig. 1, in a 2-dimensional situation [9~13]. Fig. 1 shows a series of points for two different classes: the black points for class A and the white circles for class B. The SVMs try to place a linear boundary between the two different classes and orient it in such way that the margin represented by the dotted line is maximized. Furthermore, SVMs attempt to orient the boundary to ensure that the distance between the boundary and the nearest data point in each class is maximized. Then, a boundary, such as H, is placed in the middle of this margin and between the two points. The nearest data points used to define the margin are called the support vectors and are represented by the circles. When the support vectors have been selected, the rest of the data feature set is not required as the support vectors can contain all the basic information needed to define the classifier.

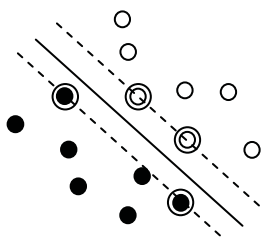

Fig. 1 The optimal hyper-plane

When given samples S (x_i , y_i) (i =1, 2, $\cdots$, N) , where N is the number of samples, the samples are assumed to have two classes, $x_i \in X = R^N$, $y_i \in Y = \{+1,-1\}$, and each of classes associates with labels: y_i =1 for class A and y_i = -1 for class B. The goal of SVMs is to defin**e** an optimal hyper-plane that divides S so that all samples with the same label are on the same side of the hyper-plane, and the distance between two classes and the hyper-plane is maximized. In the case of linear data, the hyper-plane can be expressed as follows:

$$f(x) = \omega \cdot x + b = \sum_{i=1}^{N} \omega_i \cdot x_i + b = 0, (\omega \in R^N, b \in R) \tag{11}$$

Where ω is N-dimensional vector, x is the input data, b is a classification threshold, and ω , b are used to define the position of separating the hyper-plane. The decision function is made using $sign(f(x))$ to create separating hyper-planes that classifies the input data as either belonging to class A or class B. A separating hyper-plane should satisfy the constraints:

$$\begin{aligned} f(x_i) &= 1, \quad if \quad y_i = 1; \\ f(x_i) &= -1, \quad if \quad y_i = -1. \end{aligned} \tag{12-1}$$

or it can be presented in complete equation:

$$y_i(\omega \cdot x_i + b) \geq 1, \quad i = 1, \cdots, N \tag{12-2}$$

The SVM method tries to find a unique separating hyper-plane by minimizing $\|\omega\|$ under the constraining conditions. Here $\|\omega\|$ is the Euclidean norm, and the distance between the hyper-plane and the nearest data points of each class is $2/\|\omega\|$. By introducing the Lagrange multiplier α_i, the optimal hyper-plane problem transformed into a quadratic problem (QP) as follows:
Maximize

$$Q(\alpha) = \sum_{i=1}^{N} \alpha_i - \frac{1}{2} \sum_{i,j=1}^{N} \alpha_i \alpha_j y_i y_j x_i x_j \tag{13}$$

Subject to

$$\sum_{i=1}^{N} \alpha_i y_i = 0 \tag{14-1}$$

$$\alpha_i \geq 0, \quad i = 1, \cdots, N \tag{14-2}$$

Thus, by solving the QP, the coefficient α_i is obtained, which is required to express ω and b using Eq. (15) and Eq. (26). When α is very small, the influence is negligible for the optimal hyper-plane, so we take it as zero. If $\alpha_i > 0$, x_i is called a support vector (SV).Obviously, the fewer number of support vectors, the fewer number of constraints, and the SVMs' generalization ability will be stronger.

$$\omega^* = \sum_{i \in SV} \alpha_i y_i x_i \tag{15}$$

$$b^* = y_{i,} - \omega^* x_i, i \in SV \tag{16}$$

When the SVMs are trained, the decision function can be written as

$$y = sign(\omega^* \cdot x + b^*) = sign(\omega^* \cdot y_i x_i x + b^*) \tag{17}$$

For a linear non-separable case, SVMs perform a non-linear mapping of the input vector x from the input space into a higher dimensional feature space and create the optimal hyper-plane in the feature space; the principle is shown in Fig. 2.

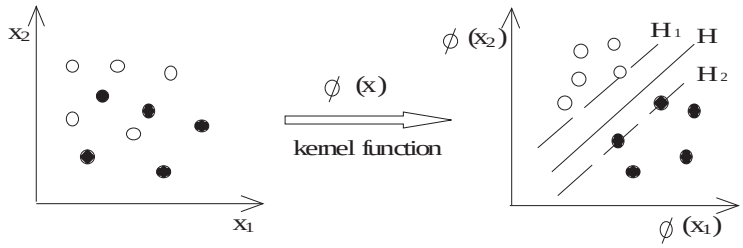

Fig. 2 Transformation to feature space from input space

This mapping is determined by the kernel function $K(x_i, x_j) = \phi(x_i) \cdot \phi(x_j)$. In fact, when applying a kernel function, the learning in the feature space does not require an explicit evaluation of ϕ. Any function that satisfies Mercer's theorem can be used as a kernel function to compute a dot product in the feature space. There are different kernel functions used in SVMs. In this work, linear, polynomial and Gaussian RBF functions were evaluated and formulated in Table 1.

Table 1 Formulation for kernel functions

Kernel function	$K(x_i, x_j)$
Linear	$x \cdot x_i$
Polynomial	$(x \cdot x_i + 1)^q$
Gaussian RBF	$\exp\{-\lVert x - x_i \rVert^2 / 2\sigma^2\}$

Upon selecting the appropriate kernel function, classification accuracy is improved, so the selection of the appropriate kernel function is very important, and influences the goal function in Eq. (17) and the decision function in Eq. (18).

$$Q(\alpha) = \sum_{i=1}^{N} \alpha_i - \frac{1}{2} \sum_{i,j=1}^{N} \alpha_i \alpha_j y_i y_j K(x_i, x_j) \tag{17}$$

$$y = sign(\omega^* \cdot x + b^*) = sign(\omega^* \cdot y_i K(x_i, x) + b^*) \tag{18}$$

SVMs' decision function is similar to that of neural networks as the output y is a linear combination of intermediate nodes, while each intermediate node corresponds to a support vector, as shown in Fig. 3. SVMs can transform non-linear data into a feature space using a kernel function. SVMs can construct an optimal classifier, which has a strong generalization capacity when only a small amount of training samples are available.

These features have an important role in the field of mechanical fault diagnosis.

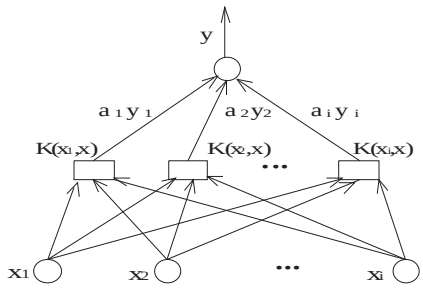

Fig. 3 SVMs' classification diagram

3.2 Intelligent Diagnosis using SVM and RRSPs

This paper presents a method using SVM and RRSPs for intelligent machine condition monitoring and fault diagnosis. The flowchart of the method is shown in Fig. 4. The data of RRSPs, as the object of follow-on process, are extracted from the vibration signals in plant for intelligent diagnosis. Put them into SVM as the training data then the optimal hyper-plane obtained. If the training data can be linearly separated by SVM, optimal hyper-plane will be obtained by linear classification. If the training data cannot be linearly separated, appropriate kernel function will be chosen to search the optimal hyper-plane using SVM. But using kernel function, the training data are mapped to higher-order feature space. It follows that the generalizing capability decreases and the computational complexity increases with the dimension becomes more. So the linear classification is used as much as possible [11]. After the optimal hyper-plane obtained, the testing data are analyzed using intelligent diagnosis method.

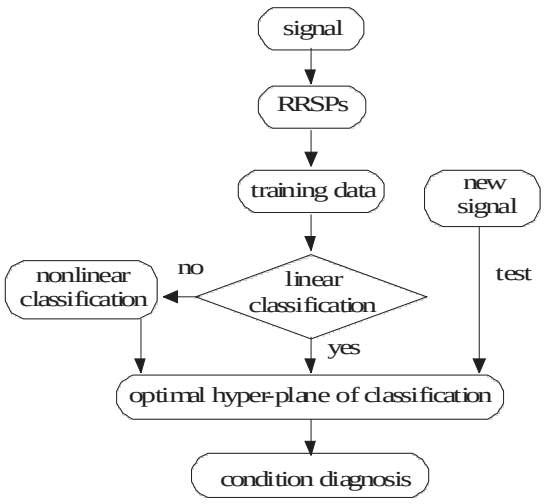

Fig. 4 Intelligent diagnosis based on SVMs and RRSPs

3.3 System of sequential Diagnosis

SVM is a 2-class classifier, however many conditions such as structural faults will be often diagnosed, and it is difficult to find the excellent SPs that can be used together. For efficient diagnosis, then using multi-SVMs, the system of sequential diagnosis is found to detect many faults and identify fault types from rotating machinery in early stage, shown as Fig. 5 [14]. The signal from the rotating machine is captured in four conditions: normal, unbalanced, looseness and misalignment. The main aim of fault diagnosis is to recognize the state of the machine. The first step is finding whether the device is normal state (N) or abnormal state (UN). If abnormal, the next step is to distinguish the state between unbalanced state (U) and other abnormal states (LM). The last step is to segregate the fault into looseness state (L) or misalignment state (M).

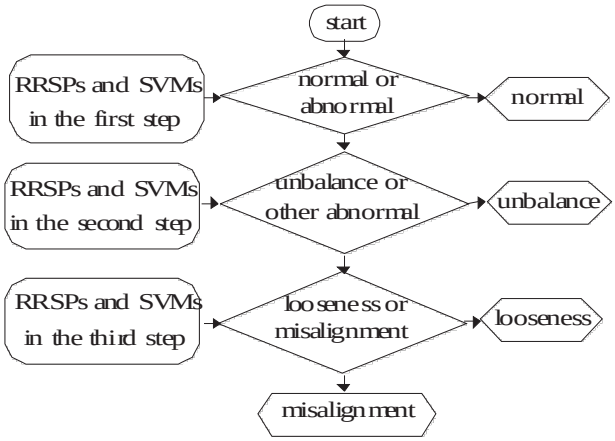

Fig. 5 System of sequential diagnosis using multi-SVMs

4. Application to an Experiment

4.1 Experimental System and Signal conditions

Fig. 6 shows the experimental rotating machine with middle rotation speed for diagnosis test, and the measuring points of accelerometers. The most commonly occurring structural faults of rotating machinery in early stage are shaft misalignment, unbalanced and looseness states. The accelerometer is used to measure vibration signals. The sampling frequency of signal measurement is 5000Hz, and the sampling time is 20s, the rotational speed is 1500rpm. The time-domain waveforms of vibration signals in each state are shown in Fig. 7. For calculating the RRSPs shown as Eq. (1) ~ (10), the vibration signals in each state are divided into 20 parts, and the spectra with 0~300Hz is obtained by a low-pass filter.

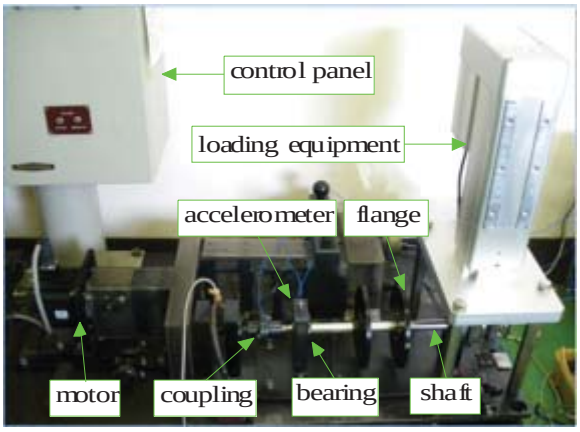

Fig. 6 Experimental equipment for intelligent diagnosis

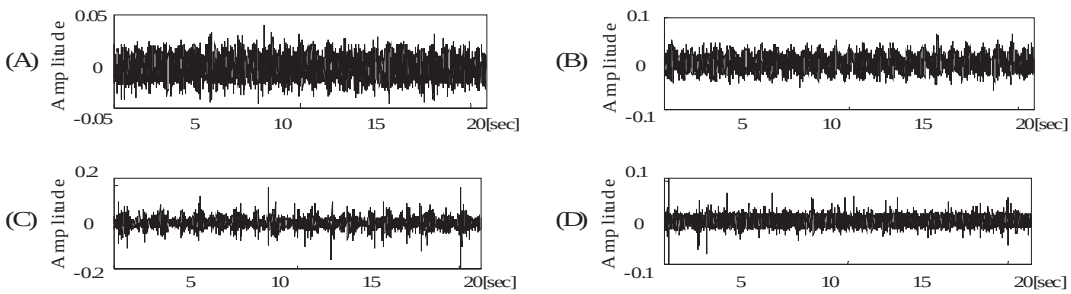

(A) Normal state (B) Unbalanced state (C) Looseness state (D) Misalignment state
Fig. 7 The time-domain waveforms of vibration signals in each state

4.2 Sensitivity of RRSPs

4.2.1 Discrimination Index (DI)

In order to evaluate the sensitivity of a SP for distinguishing two states, discrimination index (DI) is defined as follows [1].

$$DI = \frac{|\mu_2 - \mu_1|}{\sqrt{\sigma_1^{\ 2} + \sigma_2^{\ 2}}} \tag{19}$$

Here, μ_1 and μ_2 are the mean values of SP calculated by the data in state 1 and state 2 respectively. σ_1 and σ_2 are their standard deviations. When the value of DI is 1.65, discrimination rate (DR) is 95%, and when DI is 0.8, DR is 80%. Here, DR is calculated as follows.

$$DR = 1 - \frac{1}{\sqrt{2\pi}} \int_{-\infty}^{-DI} \exp(-\frac{\mu^2}{2}) d_\mu \tag{20}$$

It is obvious that the larger value of DI would get, the larger value of DR will be, and consequently, the better the SP will be. Using SVMs for diagnosis classification, when DI is more than 1.65, linear classification is usually utilized to create optimal hyper-plane, when DI is from 0.8 to 1.65, appropriate kernel function is selected to classify in feature space, but DI is less than 0.8, the sensitivity of this SP is very lower , then this SP cannot be used [2].

4.2.2 Sensitivity of RRSPs

The values of DI between the RRSPs of normal (N) and abnormal (UN), unbalanced (U) and other abnormal (LM), looseness (L) and misalignment (M) in the experiment are shown in Fig. 8. The percentage that the values DI of the RRSPs index more than 1.65, from 0.8 to 1.65, from less than 0.8 are 46.7%, 30%, 23.3% respectively, the utilization rate of the RRSPs is 76.7%.

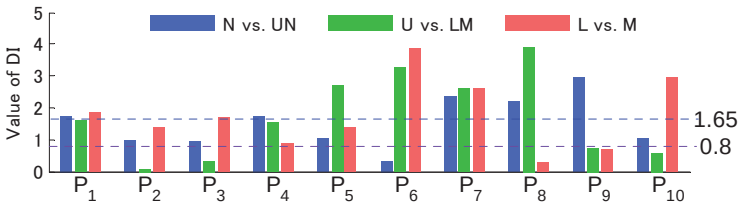

Fig. 8 Discrimination index of RRSPs

However, a large set of symptom parameters have been defined in the pattern recognition field [15, 16]. Here, 10 SPs, commonly used for the fault diagnosis of plant machinery, are shown as follows, so these parameters are called “general symptom parameters: GSPs” [1].

$$P_{11} = \sqrt{\frac{\sum_{i=1}^{N} x_i^{\ 2}}{N}} \tag{21}$$

$$P_{12} = \sigma / |\bar{x}| \tag{22}$$

$$P_{13} = \frac{\left|\sum_{i=1}^{N} (x_i - \bar{x})^3\right|}{N \cdot \sigma^3} \tag{23}$$

$$P_{14} = \frac{\sum_{i=1}^{N} (x_i - \bar{x})^4}{N \cdot \sigma^4} \tag{24}$$

$$P_{15} = P_{12}/\sigma \tag{25}$$

Here, $x_i (i = 1, 2, \cdots, N)$ is digital data of vibration signal, N is the number of data. $\bar{x}$ and σ are the mean value and the standard deviation.

$$P_{16} = \frac{\sum_{i=1}^{I} (f_i - \bar{f})^3 \cdot F(f_i)}{I \cdot \sigma^3} \tag{26}$$

$$P_{17} = \frac{\sum_{i=1}^{I} (f_i - \bar{f})^4 \cdot F(f_i)}{I \cdot \sigma^4} \tag{27}$$

$$P_{18} = \sqrt{\frac{\sum_{i=1}^{I} f_i^4 \cdot F(f_i)}{\sum_{i=1}^{I} f_i^2 \cdot F(f_i)}} \tag{28}$$

$$P_{19} = \frac{\sum_{i=1}^{I} f_i^2 \cdot F(f_i)}{\sqrt{\sum_{i=1}^{I} F(f_i) \sum_{i=1}^{I} f_i^4 \cdot F(f_i)}} \tag{29}$$

$$P_{20} = \sum_{i=1}^{I} F(f_i) \tag{30}$$

Here, I is the number of spectrum lines, f_i is the frequency from 0 Hz to the maximum analysis frequency, $F(f_i)$ is the power spectrum values at frequency f_i. $\bar{f}$ and σ are the mean value and the standard deviation of the analysis frequency, shown as $\bar{f} = \frac{\sum_{i=1}^{I} f_i \cdot F(f_i)}{\sum_{i=1}^{I} F(f_i)}$ and $\sigma = \sqrt{\frac{\sum_{i=1}^{I} (f_i - \bar{f})^2 \cdot F(f_i)}{I}}$.

The DI values of GSPs in three steps in the experiment are shown in Fig. 9. The percentage that the DI values of GSPs index more than 1.65, from 0.8 to 1.65, from less than 0.8 are 13.3%, 43.3%, 43.4% respectively, the utilization rate of the GSPs is 56.6%.

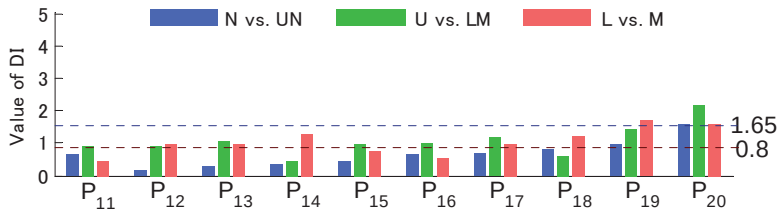

Fig. 9 Discrimination index of GSPs

It is obvious that the sensitivity and utilization rate of RRSPs are high, and it has been verified by the different structural faults experiments. Even if there will be a slight structural fault at an early stage, the sensitivity of RRSPs can be high. So it is very efficient to diagnose structural faults of rotating machinery using RRSPs.

4.3 Fault Diagnosis

According to sequential diagnosis as shown in Fig. 5, in the first step, normal state will be distinguished from three abnormal states. Firstly P_7 and P_8, the larger DI value of RRSPs (>1.65), are selected from normal state and abnormal states, to build the training data, and Y_n is defined +1 for N and -1 for UN to represent two states in Table 2. Secondly using SVM, the training data are trained to achieve Lagrange coefficient α as Table 2.

there are 3 SVs for expressing the ω and b by Eq. (15), (16), then the hyper-plane is obtained as shown in Fig. 10, and the execution time is 0.01 seconds, the margin is 0.1345. Obviously, the training data are divided correctly, so the hyper-plane is optimal for the standard of intelligent diagnosis in the first step.

Table 2 Traning data of normal and abnormal states in the first step and Lagrange coefficient

Signal state			normal state (N)						abnormal state (UN)					
Training data	X_n	No.	x_1	x_2	x_3	x_4	x_5	x_6	x_7	x_8	x_9	x_{10}	x_{11}	x_{12}
		P_7	1.06	0.99	1.06	0.99	0.96	1.01	1.39	1.62	1.68	0.81	0.74	0.90
		P_8	0.98	1.01	0.99	1.02	0.99	1.02	1.31	1.28	1.26	1.21	1.17	1.22
	Y_n		1	1	1	1	1	1	-1	-1	-1	-1	-1	-1
Lagrange coefficient			9.6E-9	6.4E-8	1.3E-8	110.5	1.7E-8	8.1E-8	5.9E-9	1.8E-8	53.52	1.7E-8	1.1E-8	57.01

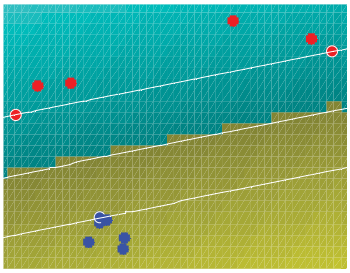

Normal state (N) **Abnormal state (UN)** **SVs**

Fig. 10 Optimal hyper-plane of normal state and abnormal state in the first step

Similarly, in the second step, unbalanced (U) and other abnormal states (LM) will be distinguished. P_4 and P_9 (0.8<DI<1.65) are selected for training data. But linear classification is used for the training data, the corresponding hyper-plane is shown in Fig. 11 (A). Obviously two states cannot be well diagnosed, so non-linear classification will be adopted and selected polynomial function and Gaussian RBF function for training. The hyper-planes are shown in Fig. 11 (B), (C), and the training results are shown in Table 3.

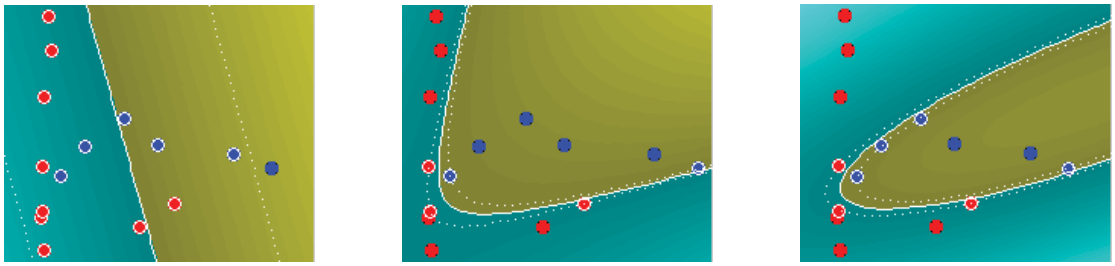

(A) Linear **(B) Polynomial** **(C) Gaussian RBF**

Unbalanced state (U) **Other abnormal state (LM)** **SVs**

Fig. 11 Optimal hyper-plane corresponding with kernel functions in the second step

Table 3 Training results corresponding with kernel functions in the second step

Kernel function	Execution Time [sec]	Margin [unit]	support vectors (SVs)
Linear	0.1	0.000007	14(93.3%)
Polynomial	0.01	0.022481	5 (33.3%)
Gaussian RBF	0.01	0.006093	7 (46.7%)

For the polynomial function and the Gaussian RBF function, execution time is same, but using the polynomial function, the margin becoming larger, and SVs being fewer, so the generalization ability goes stronger. The three functions are also applied to classify the same test data, the classification precision is 80%, 100%, 93.3% respectively. It is verified that the precision of classification is the highest using the polynomial function by the experiment results. Thus the hyper-plane shown in Fig. 11(B) is optimal for the standard of intelligent diagnosis in the second step.

In the third step, P_2 and P_9 (0.8<DI<1.65) are selected to obtain the training data for identifying looseness state (L) and misalignment state (M). Firstly the training data are trained using linear classification. However the corresponding hyper-plane is not satisfying as shown in Fig. 12 (A). Then polynomial function is selected to create the hyper-plane as shown in Fig. 11 (B). Obviously the hyper-plane is optimal for the standard of intelligent diagnosis in the third step.

(A) Linear **(B) Polynomial**

Looseness state (L) **Misalignment state (M)** **SVs**

Fig. 12 Optimal hyper-plane of looseness state and misalignment state in the third step

Then the intelligent system of sequential diagnosis has been built to detect many faults and identify fault types from structural faults of rotating machinery. In order to verify the effectiveness of the sequential diagnosis method proposed in this study, the vibration signals, which states (N, U, L, M) are known , are measured from early-stage structural faults of rotating machinery, and are calculated RRSPs for the test data. Then the test data are input to the intelligent system of sequential diagnosis, and are judged intelligently in each step. Table 4 is the results of sequential diagnosis in each step.

Table 4 Sequential diagnostic results from early-stage structural faults of rotating machinery

Test signal	Test data X_t		Output data Y_t in each step			Diagnosis result		Remarks
			1st step	2nd step	3rd step	Judge	Accuracy	
Normal state (N)	0.938	1.004	1			N	100%	1st step:
	…	…	…			…		1--normal state (N)
	0.915	1.018	1			N		-1--abnormal state (UN)
Unbalanced state (U)	0.387	1.354	-1	1		U	100%	
	…	…	…	…		…		2nd step:
	0.242	3.145	-1	1		U		1--unbalanced state (U)
Looseness state (L)	0.033	0.775	-1	-1	1	L	100%	-1--
	…	…	…	…	…	…		other abnormal state (LM)
	0.250	1.482	-1	-1	1	L		
Misalignment state (M)	0.207	2.267	-1	-1	-1	M	100%	3rd step
	…	…	…	…	…	…		1--looseness state (L)
	0.280	0.937	-1	-1	-1	M		-1--misalignment state (M)

All the testing results shown above verified that the sequential diagnosis method based on RRSPs and SVMs proposed in this paper is available in early-stage fault structural faults diagnosis.

5. Conclusions

When building an intelligent system of sequential diagnosis for rotating machinery, in order to improve the efficiency and the accuracy of the intelligent diagnosis for plant rotating machinery and distinguish fault types at an early stage, a new intelligent diagnosis method using RRSPs and SVMs was proposed, and the effectiveness was proved according to the experiment. The superiority of the method proposed in this paper can be explained by the following points:

(1) RRSPs are a new type of exclusive symptom parameters (ESPs) for detecting and identifying structural faults of rotating machinery. The sensitivity of RRSPs is very higher, even if there will be a slight fault at an early stage, it is visible that the values of RRSPs can change.

(2) The diagnosis method based on SVMs not only has a strong adaptable ability to deal with fault diagnosis with small number of training samples, but also solves the non-convergent problem that frequently occurs when traditional diagnostic methods are used.

(3) Diagnosis method using SVMs can perform a linear classification in a feature space for non-linear classification using a kernel function; therefore, when the feature of fault signal is not obvious at an early stage, the resulting identification of the equipment condition is also excellent.

(4) The efficiency of sequential diagnosis proposed here has been verified by applying it to a practical structural faults diagnosis of rotating machinery, and its performance is high. In fact, the high performance of sequential diagnosis using RRSPs and SVMs is attributed primarily to RRSPs' high sensitivity and SVMs' generalization capability.

This method will be used widely in the of condition monitoring and machinery diagnosis.

References

[1] P. Chen. *Foundation and Application of Condition Diagnosis Technology for Rotating Machinery*, Sankeisha Press, Japan, 2009.4.

[2] H. T Xue and P. Chen. Condition Diagnosis Method Based on Symptom Parameters in Time Domain and Support Vector Machine and Application to Diagnose Structural Faults of Rotating Machinery, *Japan Society of Maintenology*, Vol. 10, No. 3, pp. 51-57, 2011.

[3] P Chen, Toshio Toyota and Z. J He. Automated Function Generation of Symptom Parameters and Application to Fault Diagnosis of Machinery under Variable Operating conditions, *IEEE TRANSACTIONS ON SYSTEMS*, No. 6, pp. 775-781, 2001.

[4] S. Simani and C. Fantuzzi. Fault Diagnosis in Power Plant Using Neural Network, *Information Sciences*, Vol. 127, pp.126-136, 2000.

[5] H. MATUYAMA. Diagnosis Algorithm, *Journal of JSPE*, Vol. 75, No. 3, pp. 35-37, 1991.

[6] J. J. RICHARDSON. *Artificial Intelligence in Maintenance*, Noyes Publications, N. J., 1985.

[7] L. Zhang, L.B. Jack and A.K. Nandi.. Fault Detection Using Genetic Programming, *Mechanical Systems and Signal Processing* Vol.19, pp. 271-289, 2005.

[8] P. Chen, Tetsurou Mitoma, Noriaki Satonaga and Toshio Toyota. Condition Diagnosis Using Dimentional & Nondimentional Symptom Parameters for Rotating Machinery, *The Society of Plant Engineers Japan*, Vol. 19, No. 2, pp. 56-65, 2007.

[9] Achmad Widodo and Bo-Suk Yang. Application of Nonlinear Feature Extraction and Support Vector Machines for Fault Diagnosis of Induction Motors, *Expert Systems with Applications*, pp. 241-250, 2007.

[10] Achmad Widodo and Bo-Suk Yang.: Support Vector Machine in Machine Condition Monitoring and Fault Diagnosis, *Mechanical Systems and Signal Processing*, pp. 2560-2574, 2007.

[11] Steve R. Gunn. Support Vector Machines for Classification and Regression, *Faculty of Engineering and Applied Science Department of Electronics and Computer Science*, May 10th, 1998.

[12] B. Samanta. Gear Fault Detection Using Artificial Neural Networks and Support Vector Machines with Genetic Algorithms, *Mechanical Systems and Signal Processing*, Vol. 18, pp. 625-644, 2004.

[13] Steve R. Gunn. *Support Vector Machines for Classification and Regression*, May 10th. 1998.

[14] C. Kirkham, A. Long, O. Taylor and C. Isbell. *Adaptive Online Systems for Condition Monitoring: The Neural-Maine Project, in: Proceedings of 12th Conference Of Condition Monitoring and Diagnostic Engineering Management (Comadem)* , pp. 317-325,Coxmoor Publishing Ltd., Sunderland, UK, 1999.

[15] K. FUKUNAGA. *Introduction to Statistical Pattern Recognition*, Academic Press, 1972.

[16] P. Chen, Tetsurou Mitoma, Noriaki Satonaga and Toshio Toyota. Condition Diagnosis Using Dimentional & Nondimentional Symptom Parameters for Rotating Machinery, *The Society of Plant Engineers Japan*, Vol. 19, No. 2, pp. 56-65, 2007.

Copyright © 2012 DET Corp., Japan All Rights Reserved
International Journal of Comprehensive Engineering
Part B, 2(2), 161-171, 2013
Doi: 10.14270/IJCE2013.2.2.b161
Regular paper

ISSN 2186-2680
e-ISSN 2186-2656
www.iace-journal.org

Investigation on Machine Condition Classification by Using Multi-Scale Entropy Feature Extraction and Support Vector Machine

Hongkun Li [1, 2], Shuai Zhou [1] and Zhenggang Guo [1]

[1] School of Mechanical Engineering, Dalian University of Technology,
Dalian, 116024, China
[2] State Key Lab of Structural Analysis for Industrial Equipment, 116023, China

[#] Corresponding author: lihk@dlut.edu.cn; Tel.: +86-0411-84706561-8048

Abstract: A new condition classification method is presented which is based on wavelet packet decomposition (WPD), multi-scale entropy (MSE) and support vector machine (SVM) .Firstly, vibration signal of machine is decomposed by wavelet packet with the appropriate decomposition layer. Then, each sub-signal in different frequency band is analyzed with the multi-scale entropy. According to the multi-scale entropy distribution curves of sub-signals for different operating conditions in each frequency band, entropy of certain frequency bands and scales can be chosen to construct the feature vector for pattern recognition. In the end, SVM are used for different working conditions classification by the constructed feature vector because of its powerful performance even for small samples. In order to verify the effectiveness of this method, simulation experiment of different rolling bearing fault was implemented in the lab. According to investigation of this method on the experiment, four different operating conditions of rolling bearing can be effectively indentified using the above method. Based on the result analysis of classification, it can be concluded that this method is very effectiveness for machine fault diagnosis. Thus, this promising method will contribute to machine condition monitoring and fault diagnosis process.

Keywords: Wavelet Packet Decomposition, Multi-scale Entropy, Support Vector Machine; Condition Classification.

Received: May 25,2012 / Accepted: Feb. 20,2013 / Published: Jul. 5,2013

1. Introduction

Many methods have been investigated on machine pattern recognition and fault diagnosis. Vibration signal analysis has been broadly used on condition classification, such as Fourier transform, Wigner-Ville distribution, Empirical Mode Decomposition with support vector machine [1], machine condition identification based on support vector machine and information spectrum entropy [2], machine conditions classification by using Hilbert spectrum feature extraction and support vector machine [3], and etc. However, how to effectively extract the characteristics of the fault information is the pivotal problem.

With the development of the wavelet analysis since 1980, it is broadly used to process vibration signals and the effect is remarkable [4]. As the extension and development of wavelet transform, Wavelet Packet Decomposition (WPD) is multi-dimensioned. Entropy is very suitable for characterizing time series' complexity. With the increment of the randomization for time series, its entropy will also increase. Richman put forward sampling entropy based on the improvement of approximate entropy[5], which was presented by Pincus [6]; Costa [7,8] put forward the algorithm of Multi-scale Entropy (MSE), a novel method for measuring finite time series complexity. The classification method is also very important for accurate conditions analysis according to the constructed feature vector. Vapink has introduced support vector machine (SVM) based on statistical learning

theory, which is a relatively new approach on machine working conditions monitoring and pattern recognition [9,10]. SVM has gained acceptance in machine learning, computer vision, and pattern recognition communities for their high accuracy and good generalization capability. It will be beneficial for condition classification.

In this paper, a new method for machine operating condition classification is presented using WPD, MSE and SVM. WPD is made toward machine operating signals, and the decomposed sub-signals in different frequency bands are analyzed by MSE. In order to identify machine's operating conditions, multi-scale entropy distribution curves of different machine operating signals in a certain frequency band are compared. The feature vector for operating condition is established by entropy with proper frequency bands and scales. SVM is used for different working conditions classification by the constructed feature vector. A rolling bearing's working condition pattern recognition was carried out to testify the effectiveness of this method. This method will contribute the development of machine pattern recognition according to the classification result.

2. Theory and Method

2.1 Multi-scale Entropy

MSE has been widely used in the analysis of physiological time series [11], after firstly presented by Costa. Based on sampling entropy, it can be employed to describe the irregularity of MSE.

For $\{x_1, x_2, \cdots, x_i, \cdots, x_N\}$, which is a discrete time series with a length of N. Time series $\{y^{(\tau)}\}$ can be acquired through coarse-graining transformation of Eq.(1).

$$y_j^{\tau} = 1/\tau \sum_{i=(j-1)\tau+1}^{j\tau} x_i \quad . \tag{1}$$

where τ is time scale.

The length of coarse-grained time series is $M = \mathrm{int}(N/\tau)$. When τ =1, the coarse-grained time series is identical to the original time series. The sampling entropy for different sampling interval τ can be calculated as following. According to the time series of length *M*, which is transformed under time scale τ , a m-dimension vector can be constructed.

$$X_m(i) = \{y_{i+k} : 0 \le k \le m-1\} \quad . \tag{2}$$

For each single *i*, the distances can be calculated between $X_m(i)$ and each of the remaining vectors $X_m(j)$:

$$d\left[X_m(i), X_m(j)\right] = \max\left[\left|y_{(i+k)} - y_{(j+k)}\right|\right] \quad ,\left(0 \le k \le m-1;\ \ i, j = 1 \sim M-m+1; i \ne j\right) \quad . \tag{3}$$

Set *r* (*r*>0) as a clear threshold for the matching process. For each *i*, $B^m(i)$ which meets the condition of $d\left[X_m(i), X_m(j)\right] < r, \left(i, j = 1 \sim M-m+1; i \ne j\right)$, and define the ratio of $B^m(i)$ to the total distance as:

$$C_i^{m,\tau}(r) = B^m(i) / (M-m) \quad . \tag{4}$$

The average of $C^{m,\tau}(r)$ can be expressed as:

$$C^{m,\tau}(r) = (M-m+1)^{-1} * \sum_{i=1}^{M-m+1} C_i^{m,\tau}(r) \quad . \tag{5}$$

Increasing the dimension to m+1 and repeating the above steps:

$$C_i^{m+1,\tau}(r) = B^{m+1}(i) / (M-m+1) \quad . \tag{6}$$

The average of $C^{m+1,\tau}(r)$ is as following:

$$C^{m+1,\tau}(r) = (M-m)^{-1} * \sum_{i=1}^{M-m} C_i^{m+1,\tau}(r) \quad . \tag{7}$$

When M is finite, estimated sampling entropy of series with a length of M can be obtained following Eq.(8):

$$SampEn(m,r,M) = -\ln\left[\frac{C^{m+1,\tau}(r)}{C^{m,\tau}(r)}\right]. \tag{8}$$

Sampling entropy for different τ can be obtained by repeating the above steps.

The self-similarity of time series increases with the decrease of sampling entropy, while series' complexity increases with the increase of sampling entropy. Entropy is suitable for characterizing system complexity. Based on sample entropy, MSE has the following merits: it can be used for multi-scale analysis; sample entropy of different signals can be analyzed on different scales. The sampling entropies of various condition signals are different on different scales. Selecting entropies with big entropy difference for characteristic vector construction can be better for condition recognition. Fig.1 is the MSE of typical signals [12].

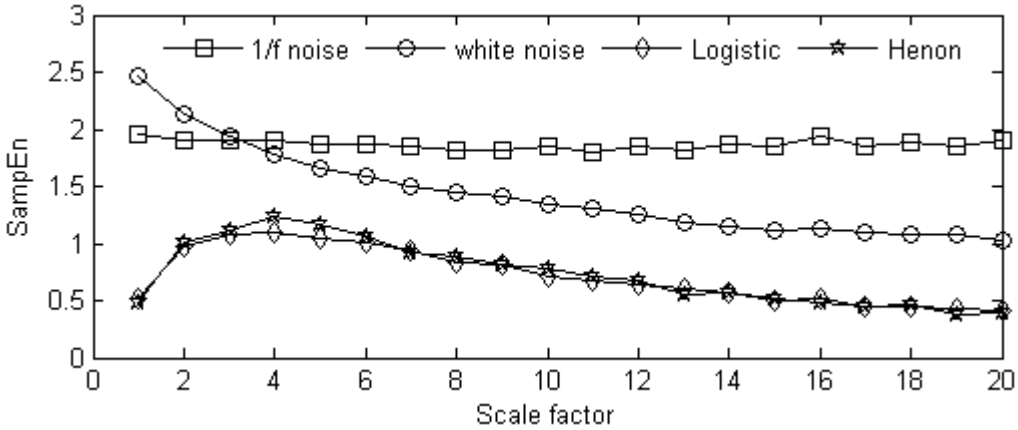

Fig. 1 MSE analysis of several typical signals

2.2 Wavelet Packet Decomposition

The core idea of WPD put forward by R.Coifman and V.Wickerhauser is used to re-decompose the wavelet subspace series after multi-resolution analysis, and re-devise the frequency window, which is wider with the reduction of dimension. Thus, the resolution of signal's high-frequency part will increase.

Set $\{h_k\}_{kez}$ and $\{g_k\}_{kez}$ as quadrature mirror filter (QMF), $\phi(t)$ and $\psi(t)$ as scaling function and wavelet basic function. Define a set of recursive functions:

$$\begin{cases} W_0(t) = \phi(t) = \sqrt{2}\sum_k h_k \phi(2t-k) \\ W_1(t) = \psi(t) = \sqrt{2}\sum_k g_k \phi(2t-k) \\ W_{2n}(t) = \sqrt{2}\sum_{k\in Z} h_k W_n(2t-k) \\ W_{2n+1}(t) = \sqrt{2}\sum_{k\in Z} g_k W_n(2t-k) \end{cases} \tag{9}$$

According to signal filter, orthogonal wavelet packet decomposition is to filter the signal through a low pass filter and a high pass filter respectively. A group of low frequency signals and a group of high frequency signals can be obtained. Actually, wavelet packet decomposition is a frequency separating method, some sub-signals in

certain frequency bands are chosen and analyzed according to actual requirement. As different types have different optimum decomposition layers，it needs further investigation. 3-layer wavelet packet decomposition is shown in Fig.2. Wavelet packet can decompose signal in the whole frequency band. It is very helpful for condition classification.

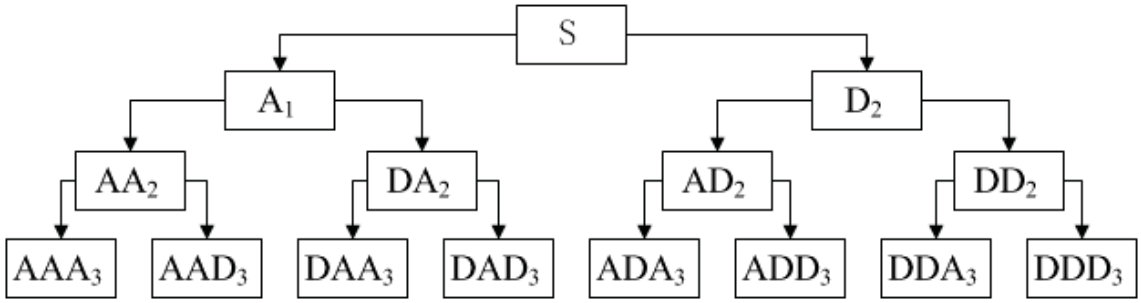

Fig. 2 Three-layer wavelet packet decomposition tree

2.3 Multi-scale Entropy

SVM is a new pattern recognition and statistical learning method which is developed in the end of last century. It has been broadly investigated and applied on pattern recognition area since it was introduced. The basic idea of the pattern recognition with SVM is to project sampling space into a high-dimensional eigenspace. In the eigenspace, optimal separating hyper-planes (or hyper-lines) of the original sample set can be found [13]. The detail description can be found in paper [14]. There are two basic classifiers for SVM. One is the binary classifier. The other is the multi-class classifier. The binary support vector classifier has been broadly applied. It uses the discriminant function $f: x \subseteq \square^n \to \square$ of the following form:

$$f(x) = \langle \alpha k_s(x) \rangle + b \quad (10)$$

where $k_s(x) = \left[k(x,s_1),\cdots,k(x,s_d)\right]^T$ is the vector of evaluations of kernel functions centered at the support vectors $S = \{s_1,\cdots,s_d\}, s_i \in \square^n$, which are usually subsets of the training data. $\alpha \in \square^l$ is a weight vector and $b \in \square$ is a bias. The binary classification rule $q: x \to y = \{-1,1\}$ is defined as:

$$q(x) = \begin{cases} 1 & for \quad f(x) > 0 \\ -1 & for \quad f(x) < 0 \end{cases} \quad (11)$$

If there is an equation, $\langle \alpha k_s(x) \rangle + b = 0$, it means there have a Hyper-plane. It divides the input vectors X into two part, corresponding to $f(x) > 0$ and $f(x) < 0$. Otherwise, there is not a Hyper-plane to divide the input data. Plane H is the Hyper-plane for two different classes shown in Fig.3.

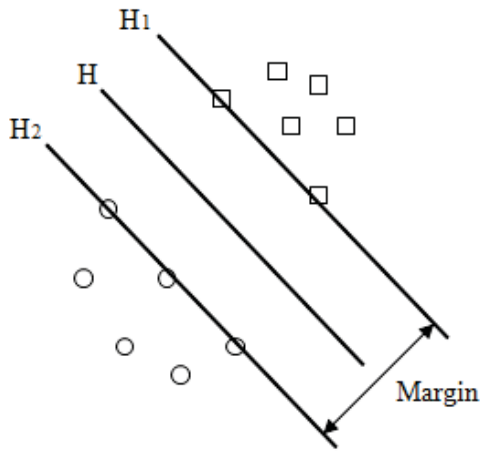

Fig. 3 Hyper-plane for SVM on pattern recognition process

In practical applications there are many kinds of machine working conditions, the binary classification is not suitable for practical applications. Thus, a multi-class classifier is developed. The multi-classifier algorithm has only one SVM classifier, but its classifying function is very complex, the calculation is very complex as well. The training and recognition is very time-consuming, and the classifying error is big when samples are large, which also limits its application. To effectively recognize engine working condition and suitable for practical application, the combination some two-class SVM classifiers for multi-class pattern recognition has been investigated, it is named as one-to-others system [15].

The algorithm of one-to-others as follows: For a data set of k classes:

$$(x_i, y_i),\ \ i = 1,\ldots,l,\ \ x_i \in R^d,\ \ y_i \in \{1, 2, \cdots, k\}. \tag{12}$$

Where l is sampling number, d is dimension of sampling vector, k is class number. First, there is a case of k classes, take a top-priority class from these k classes as a category, take the rest (k-1) classes as another category, construct a two-class SVM classifier and name it SVM1; Next, this top-priority is excluded ,and then there is a case of k-1 classes, take a top-priority class from those k-1 classes as a category, and take the rest (k-1)-1 classes as another category, and construct a second two-class SVM classifier and name it SVM2, and so on until the last two-class SVM classifier is constructed and named SVM k-1. In this way, k-1 two-class SVM classifiers can be constructed in all for a case of k classes. During the fault diagnosis, the most common or the most dangerous fault can be given top priority. The one-to-others is a binary tree composed of several two-class SVM classifiers in Fig. 4.

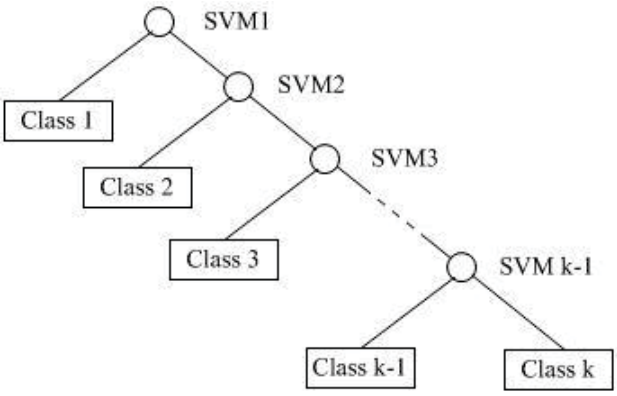

Fig. 4 Frame work of the one-to-others SVM algorithm

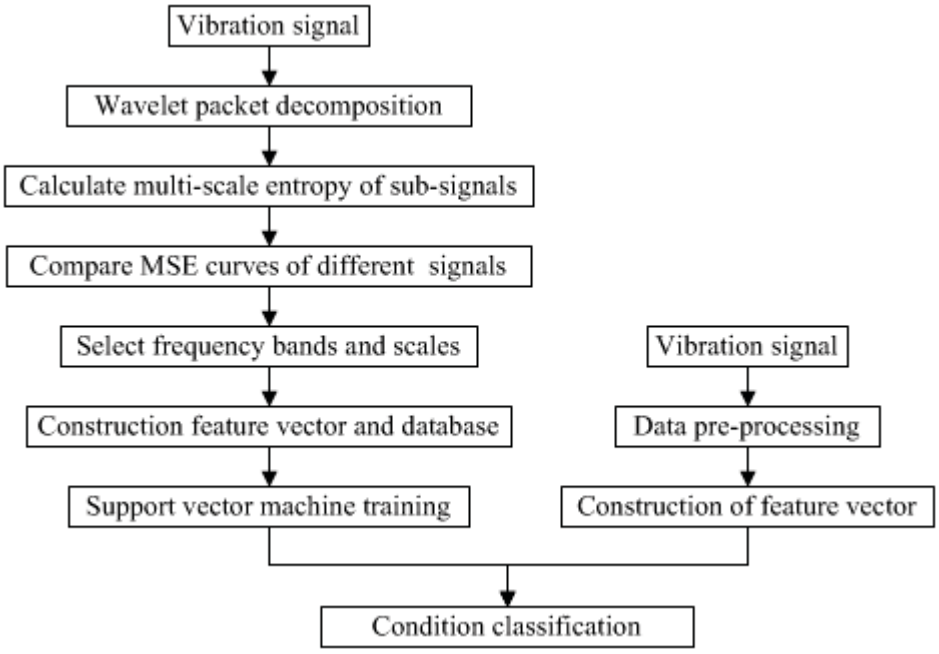

Fig. 5 Flow chart for the classification process

2.4 Condition Classification Progress

In order to classify different machine conditions, WPD is used to decompose original vibration signal. MSE analysis toward signals can provide frequency bands and scales, where entropy can effectively distinguish different machine conditions. Machine condition classification can be carried out as following: First, vibration signal is decomposed into multiple sub-signals in different frequency bands. Then, MSE of resulted sub-signals are calculated according to above equations. Scales and frequency bands are selected, where sampling entropy of different working conditions can be distinguished between each other. Entropies of the selected frequency bands and scales are used to construct original signal's feature vector for condition classification. In the end, the feature vector is input to the SVM for training and discrimination of the working conditions.

For some testing samples of vibration signal, the analyzing process is as following. First, the vibration signal need be preprocessed because of interference signal. Then, feature vectors of testing samples are calculated using above method. Compared with the result of SVM, testing samples will be classified. A flow chart of this method is shown as Fig.5. An experiment carried on in the lab is shown in detail for this method.

3. Experimental Test

In this paper, a bearing experiment is as an example to examine the effectiveness of this method in different working conditions with different speed. The type of experiment rolling bearing is N205. There are four kinds of condition, normal, outer ring wearing, inner ring wearing, and ball wearing. Rotational velocities of the motor were 600RPM，900RPM，1200RPM，and 1500RPM. Two acceleration vibration signals radical located at the bearing block were monitored by hardware produced by BK signal monitoring system and its type is 3560. **Fig.6** shows the pictures during the experiment in the lab. The sampling frequency is 65536Hz, and the sampling length is 16384.The time domain signals of four different rolling bearing operating conditions are shown in **Fig.7**.

Fig. 6 Experiment pictures in the lab

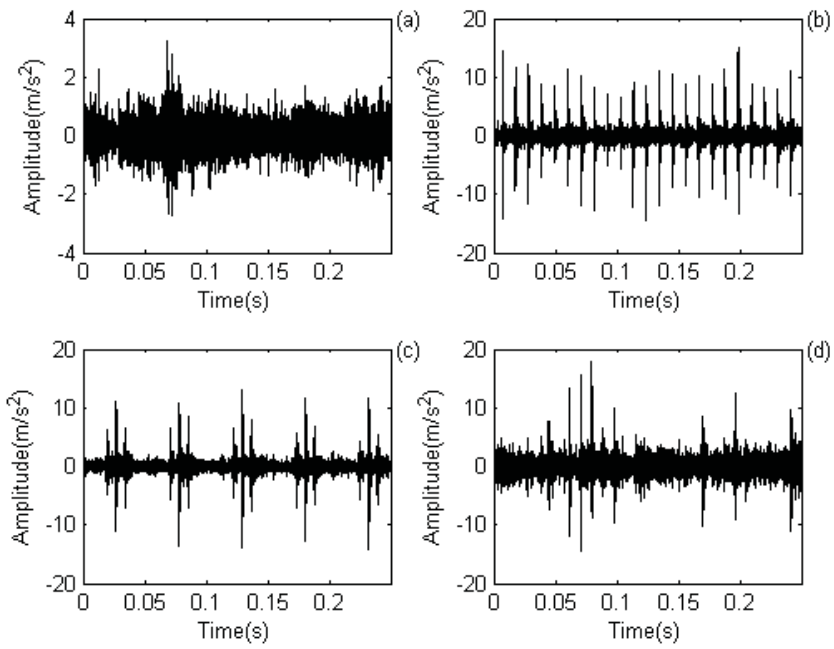

Fig. 7 Time domain signal for different working conditions with speed 1200RPM. (a)normal condition. (b) outer ring wearing. (c) inner ring wearing. (d) ball wearing.

3.1 Data Analysis

When motor speed is 900RPM, five groups of data are collected for each of the four types of conditions. The results of MSE analysis are presented in Fig. 8. From the results, only the multi-scale entropy of inner condition is obviously distinguished from other conditions, while the entropies of other three conditions are too close to be distinguished from each other on the scale from 2 to 12. The four operating conditions can't be identified just based on MSE of the original data.

The signals of rolling bearing are always mixed with noise signals from other parts. In the most circumstance, analysis of original signal will not give ideal results. In order to reduce noise disturbance and effectively distinguish the four different operating conditions, WPD is carried on original data. Because of different types of signals with different optimal decomposition level, it needs to try to select the best decomposition level. Generally, decomposition level is two to five layers for rolling bearing fault signal. In the paper, the decomposition layer is set three. The wavelet packet base is more similar to the signal, the result is better. According to the characteristics of the bearing signal, db10 is selected to be wave packet base [16, 17]. Fig.9 shows that the vibration signal of ball wearing condition decomposed into eight sub-signals frequency bands. Sub-graphs of S30, S31, … S37 are corresponding to the frequency bands from low level to high level.

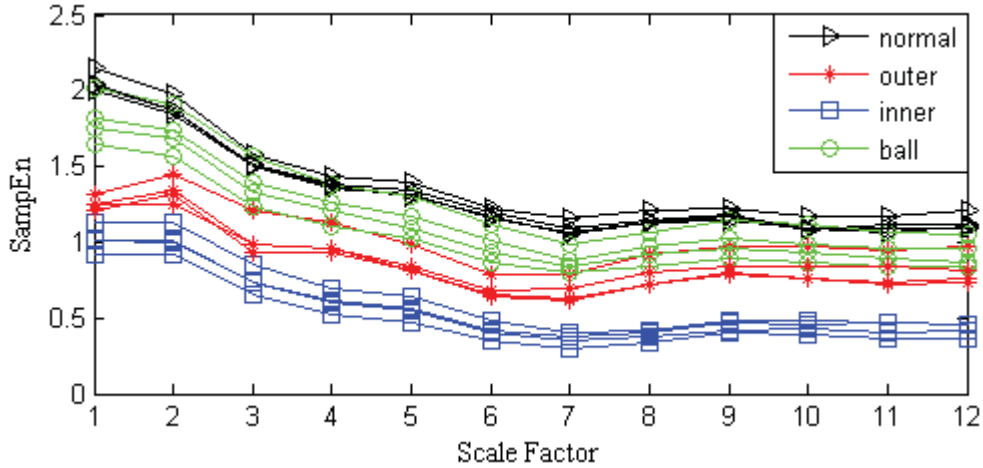

Fig. 8. MSE analysis of four rolling bearing working conditions

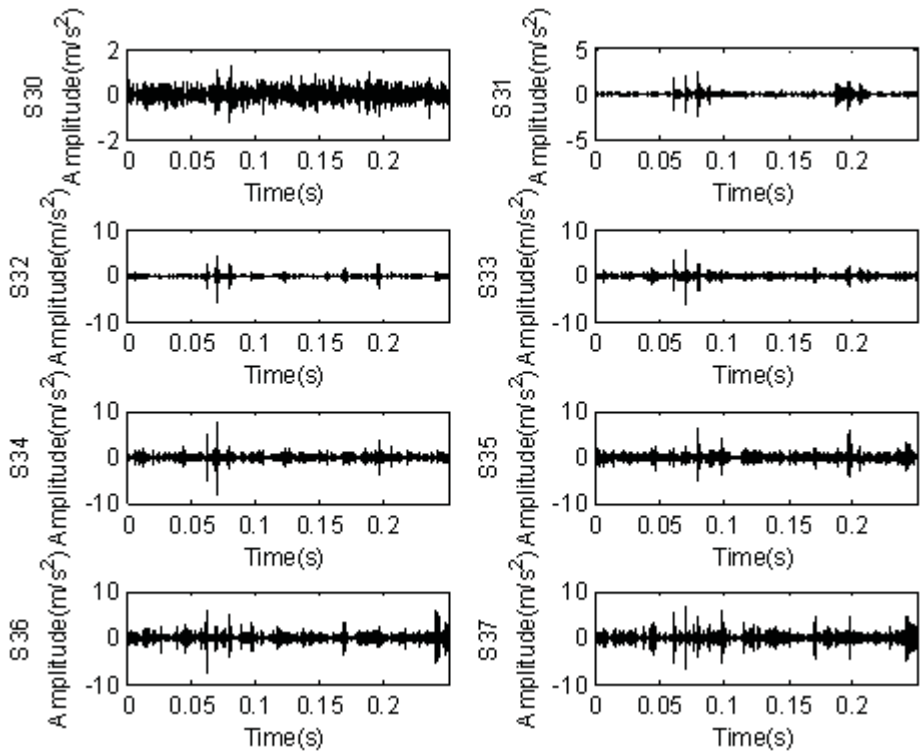

Fig. 9 Time domain of the decomposed sub-signals

3.2 Data Analysis

Each original data is decomposed into sub-signals in eight frequency bands. Then, MSE of each sub-signal will be calculated. By comparing MSE cures of sub-signals with different working condition, MSE curves of four working conditions can be effectively distinguished in the frequency band 3 and 7, while MSE curves are mixed together in the other frequency. MSE curves of four rolling bearing working conditions in third frequency bands and seventh frequency are shown in Fig.10 and Fig.11. In the frequency band 3 with scale of 4 and 8, MSE curves of inner ring wearing and outer ring wearing can be distinguished from other working conditions, but ball wearing can't be distinguished from normal condition. In the frequency band 7 with scales 1, 2, 3, 4, 6, 7, 8, 9 and11, MSE curves of normal condition can be distinguished from other obviously, but other three working conditions can't be distinguished from each other. From the above analysis, it is hard to totally distinguish the four conditions just using sampling entropies of sub-signals in one frequency band and one scale. So two sub-signals sampling entropies in different frequency bands and scales needs to be selected to construct original signal's character vector $M(x, y)$, and the detailed combination is listed in Table 1.

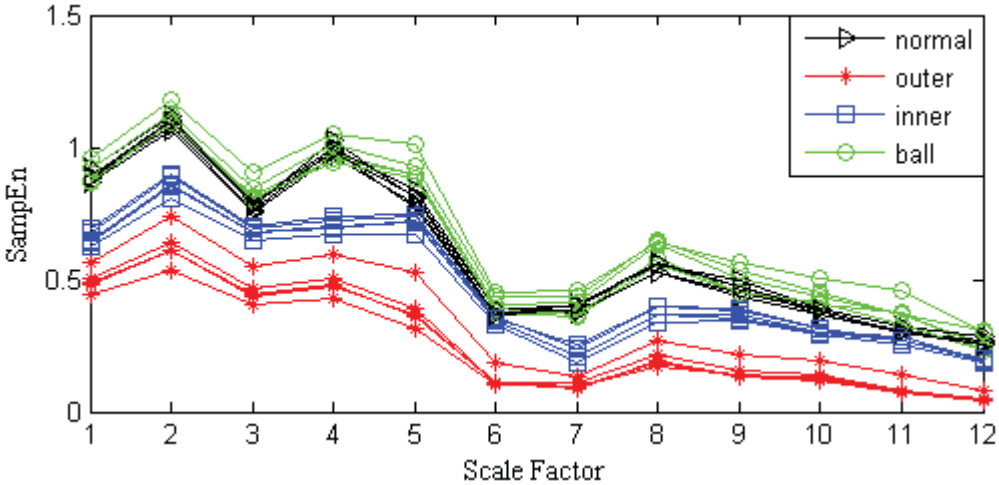

Fig. 10 MSE curves of four rolling bearing working conditions in third frequency bands

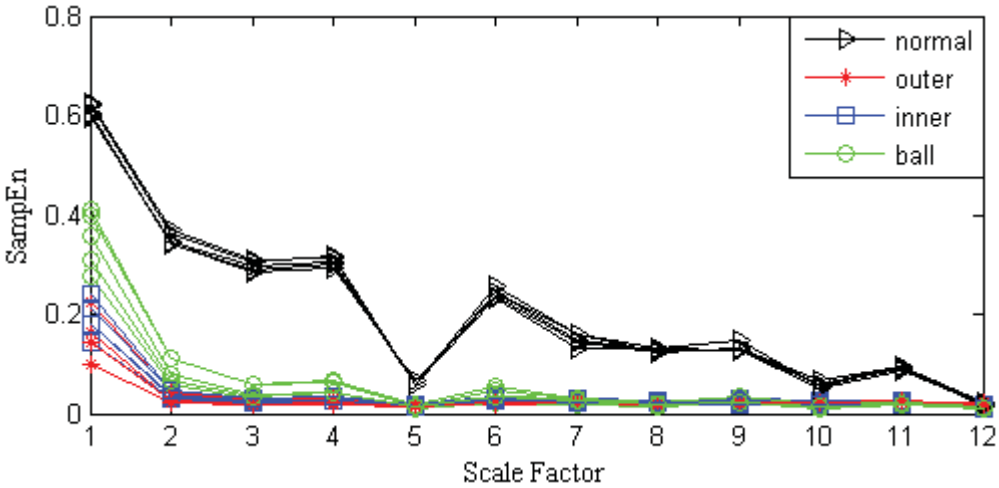

Fig. 11 MSE curves of four rolling bearing working conditions in seventh frequency band

Table 1 Combination of character vector *M*(*x*,*y*)

Sampling entropy	*x*	*y*
Frequency band	3	7
Scale	4, 8	1, 2, 3, 4, 6,7, 8, 9

3.3 Condition Classification by Using SVM

Based on overall consideration, the sampling entropies of the frequency band 3 with scale 4 and the frequency band 7 with scale 3 are selected to construct the character vector for condition classification. For each condition, 90 sets of data are collected. Feature vector $M(x,y)$ is constructed from sampling entropy x of band 3 with scale 4

and the sampling entropy *y* of band 7 with scale 3, where 3-layer wavelet packet decomposition is done toward each signal. SVM is used for different working conditions classification by the constructed feature vector. These are normal conditions, inner wearing conditions, outer wearing conditions and ball wearing conditions. Fig. 12(a) shows four kinds of working conditions classification result. The result is also expressed in the Table 2. While select the sampling entropies of scale 1 and scale 8 to construct the character vector, character vector $M(x,y)$ is constructed from sampling entropy *x* of scale 1 and the sampling entropy *y* of scale 10. Fig. 12(b) shows conditions classifications results. The result is also expressed in the Table 3. By comparing the results, this method can effectively recognize different bearing working conditions. Classification result with vector compose of sub-signals' MSE is more accurate than the result with vector compose of original' MSE.

In order to verify performance of this method, the authors have also done research with different speed condition. The result is basically similar to the speed of 900 RPM. Take conditions classification with the speed of 1200RPM as an example. Combination method of vector $M(x,y)$ is shown in Table 4. Fig. 13 shows four kinds of working conditions classification result with the speed of 1200RPM, the recognition result is accurate.

Although only bearing conditions classification is used as an example to testify the effectiveness of this method, the method presented in this article is also suitable for other mechanical recognition processed.

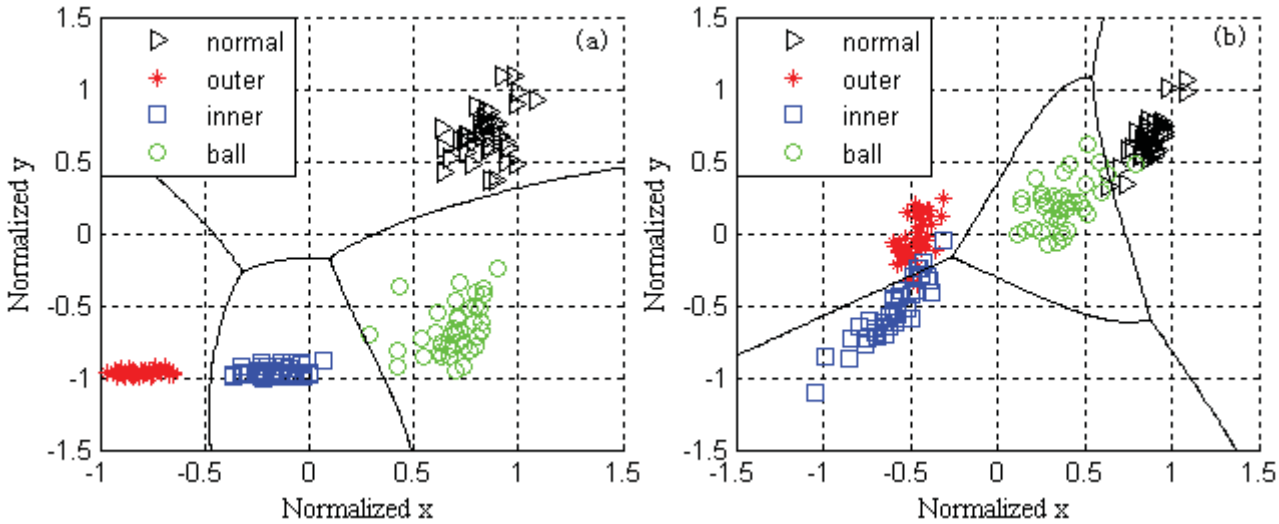

Fig. 12 2D classification result for different working condition. (a) MSE of sub-signal. (b) MSE of original signal

Table 2 Conditions' classification results based on MSE of sub-signals decomposed by WPD

	Normal	Inner	Outer	Ball
Training samples	50	50	50	50
Testing samples	40	40	40	40
Correct samples	40	40	40	40
Recognition rate (%)	100	100	100	100
Total recognition rate (%)		100		

Table 3 Conditions' classification results based on MSE of original signals

	Normal	Inner	Outer	Ball
Training samples	50	50	50	50
Testing samples	40	40	40	40
Correct samples	39	38	36	39
Recognition rate (%)	97.5	95	90	97.5
Total recognition rate (%)		95		

Table 4 Combination of character vector M(*x*,*y*)

Sampling entropy	*x*	*y*
Frequency band	6	7
Scale	1, 4	1, 2, 3, 4, 6

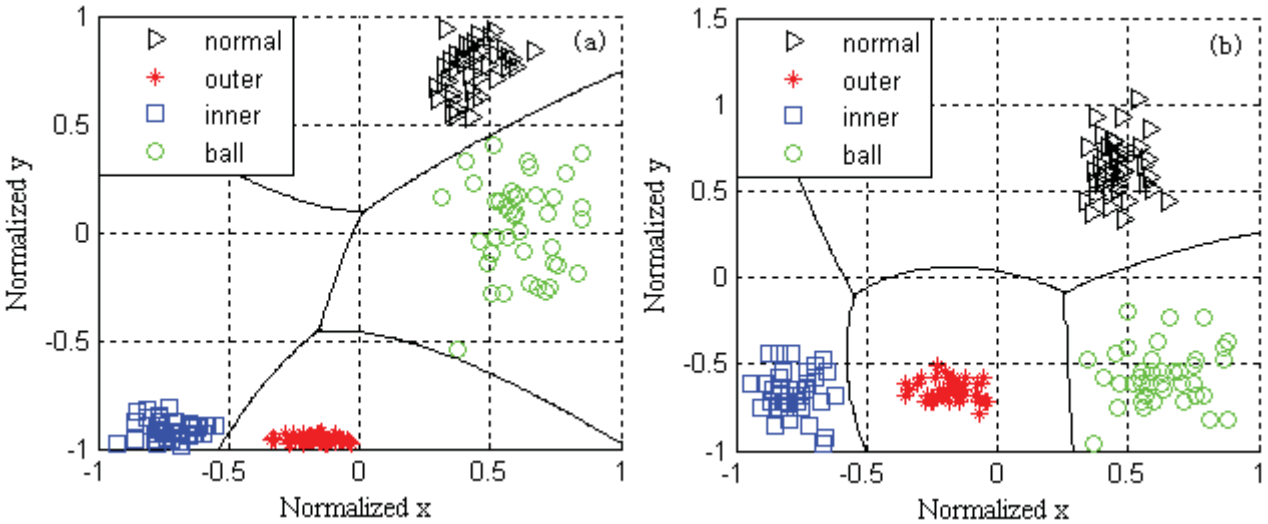

Fig. 13 2D classification result for different working condition with speed of 1200 RPM. (a) *M*(*x*,*y*) constructed by sampling entropy *x* of band 6 with scale 1 and the sampling entropy *y* of band 7 with scale 4. (b) *M*(*x*,*y*) constructed by sampling entropy *x* of band 6 with scale 4 and the sampling entropy *y* of band 7 with scale 5.

4. Conclusions

A new method for machine operating condition identification is presented based on the research of WPD-MSE-SVM. Feature extraction is very important for accurate pattern recognition. It is the basis for accurate classification. Vibration signal is decomposed by wavelet packet, in order to find difference of different working condition signals in the different frequency bands. Multi-scale entropy is used to decompose sub-signals; characteristic vector composed of entropies which can effectively distinguish different rolling bearing conditions. SVM is a very effective tool for small samples pattern recognition and is used in this study for the condition classification process. From the experiments, four different operating conditions of rolling bearing can be effectively indentified. This new approach is effective in pattern recognition of the rolling bearing. At the same time, this approach is also suitable to other components' pattern recognition of machine. Thus, this promising method will contribute to machine condition monitoring and fault diagnosis process.

Acknowledgment

The support from National Basic Research Program of China973 Program (Grant No: 2012CB026000), Chinese National Science Foundation (Grant No: 51175057) and the Fundamental Research Funds for the Central Universities (Grant No: DUT11NY04) for this research is gratefully acknowledged.

References

[1] Y. Yu. *Research on Fault Diagnosis Methods for Rotating Machinery Based on Empirical Mode Decomposition and Support Vector Machine*, Hunan University Press, 2005.

[2] M. Q Pan, X. J Zhou, C. L Yang, M Pang. Application of Support Vector Machine Based on Information Spectrum Entropy in Machine State Identification, *Chinese journal of sensors and actuators*, Vol. 18, No. 2, pp. 277-280, 2005.

[3] H. K Li. Investigation on Machine Conditions Classification by Using Hilbert Spectrum Feature Extraction and Support Vector Machine, *Journal of Vibration and Shock*, Vol. 28, No. 6, pp. 131-134, 2009.

[4] K. W Wang, Z. D Fang. Study on Application of Wavelet Transform Technique to Fault Diagnosis of Rotary Machine, *Computer Engineering and Applications*, Vol. 44, No. 8, pp. 207-209, 2008.

[5] J. S. Richman and J. R. Moorman. Physiological Time-Series Analysis Using Approximate Entropy and Sample Entropy, *Am Physiological Soc*, Vol. 278, No. 6, pp. 2039-2049, 2000.

[6] S. M. Pincus. Approximate Entropy as a Complexity Measure, *Chaos*, Vol. 5, No. 1, pp. 110-117, 1995.

[7] M. Costa, A. L. Goldberger and C. K. Peng. Multi-Scale Entropy Analysis of Complex Physiologic Time Series, *Physical Review Letters*, Vol. 89, No. 6, pp. 068102, 2002.

[8] M. Costa, A. L. Goldberger and C. K. Peng. Multi-Scale Entropy Analysis of Biological Signals, *Physical Review E*, Vol. 71, No. 2, pp. 021906, 2005..

[9] Vapnik, V. N. *The Nature of Statistical Learning Theory*, Tsinghua University Press, 2000.

[10] G. Gao, S. Z Li and K. L Chan. Support Vector Machines for Face Recognition, *Image Vis. Comput.*, Vol.19, No. 9-10, pp. 631-638, 2001.

[11] M. Costa, C. K. Peng, A. L. Goldberger and J. M. Huasdorff. Multi-Scale Entropy Analysis of Human Gait Dynamics, *Physica A*, Vol. 330, pp. 53-60, 2003.

[12] G. B Zheng, N. D Jin. Multi-Scale Entropy and Dynamic Characteristics of Two-Phase Flow Patterns, *Acta Physica Sinica*, Vol. 58, No. 7, pp. 4485-4491, 2009.

[13] P. Zhou, H. Li, and D. Clelland. Pattern Recognition On Diesel Engine Working Conditions By Wavelet Kullback–Leibler Distance Method, *Proc. IMechE, PartC: J.Mechan-ical Engineering Science*, Vol. 219, No. 9, pp. 879-888, 2005.

[14] N. E. Huang, Z. Shen, S. R Long, M. C Wu, H. H Shih, Q. N Zheng, N. C Yen, C. C Tung and H. H Liu. The Empirical Mode Decomposition and the Hilbert Spectrum for Nonlinear and Non-Stationary Time Series Analysis, *Proc. R. Soc. Lond. A,Math. Phys. Eng. Sci.*, Vol. 454, pp. 903-995, 1998.

[15] S. F Yuan and F. L Chu. Support Vector Machines-Based Fault Diagnosis for Turbo-Pump Rotor, *Mech Syst Signal Process*, Vol. 20, No. 4, pp. 939-952, 2006.

[16] C. S Zhao. Investigation on Fault Features Enhancement Method and Condition Prediction for Rolling Bearing, *Dalian Univercity of technology*, 2010.

[17] X. G Zhao. Study on The Fault Diagnosis Methods of Rolling Bearing Based on Wavelet Transform and Emprical Mode Decomposition, *Shandong University of Science and Technology*, 2009.

Copyright © 2012 DET Corp., Japan All Rights Reserved
International Journal of Comprehensive Engineering
Part C, 2(2), 172-179, 2013
Doi: 10.14270/IJCE2013.2.2.c172
Regular paper

ISSN 2186-2680
e-ISSN 2186-2656
www.iace-journal.org

Trajectory Planning and Motion Simulation on High-Speed Transplanting Bowl Seeding Robot

Chunhui Qi [1], Jianping Hu [1], Jun Ma [1], Jianbing Zhang [1] and Xuejun Yang [2]

[1] Key Laboratory of Modern Agricultural Equipment and Technology, Ministry of Education&Jiangsu Province, Jiangsu University, Zhenjiang, 212013, China
[2] Chinese Academy of Agricultural Mechanization Sciences

[#] Corresponding author: 1146804277@qq.com

Abstract: Transplanting bowl seedings is an important link of industrialized breeding system for vegetables and flowers, base on Two-DOF Five-bar parallel mechanism, adopt pneuncatic manipulator to fetching seeding and planting seeding, in order to transplanting bowl seedings from high density to low density potted trays. The movable needs of the transplanting robot was studied, the formula of inverse kinematics of transplanting robot was deduced by using the theory of inverse kinematics of the parallel mechanism. Considered the demand of the "fetch and plant" operations, made an important research on the desired trajectory of the moving platform, the virtual prototype of this mechanism is created in Pro/E software and verified the rationality of structure design and trajectory planning through the ADAMS kinematics simulation, provided theory basis for optimal design of physical prototype.

Keywords: Transplanting Bowl Seeding, Inverse Position, Trajectory Planning, Virtual Prototype Technology.

Received: May 10,2012 / Accepted: Feb. 20,2013 / Published: Jul. 5,2013

1. Introduction

Vegetables and flowers industrialized breeding is represented by light matrix potted tray seeding, bowl seedings transplanting is an important link in the process of production[1].Potted tray seedling transplanting machine technology research and development began in the 1980s,Kutz designed a nursery plant transplanting machine with Puma 560 robot as body in 1987[2],it could transplant seedings from 392 to 36 holes potted tray; K.C.Ting and Y.Yang developed a transplanting robot with Four-DOF industrial robot ADEPT—SCARA as body in 1992,in the case of trays adjacent to transplant a single seedling need time of 2.60 ~ 3.25s.However, transplanting machines with the industrial robot as body have many shortcomings, such as many freedoms (usually more than three),complicated structure, low working efficiency and so on, have many difficults to fit for greenhouse automatic assembly line working facilities, so the type of automatic potted tray seedling transplanting machine fails to get promotion.

The article will put forward a Two-DOF high-speed parallel transplanting robot of independent mechanical and electrical system, as shown in Fig. 1, the driving motors fixed on the frame, driven arms are made into light bars, so can make the moving platform achieve high speed and acceleration, to meet the potted tray bowl seedlings transplanting demand of high speed and short to medium distance.

2. Trajectory planning of bowl seeding transplanting robot

2.1 Sketch of robot movement

Two-DOF high-speed parallel mechanism used to pick up and placed the objects, its main job is pick up objects in the initial position, then move to target position placed the objects[3], sketch of movement is shown in Fig. 2.

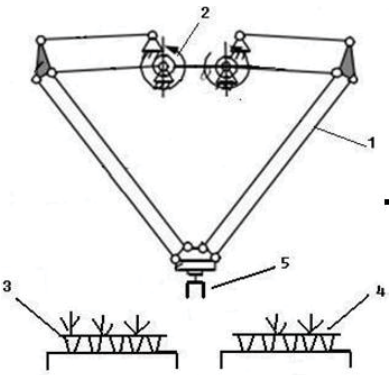

Fig. 1 Sketch map of parallel transplanting robot
1. parallel mechanism 2.motor 3.seeding tray
4.plant seeding tray 5. manipulator

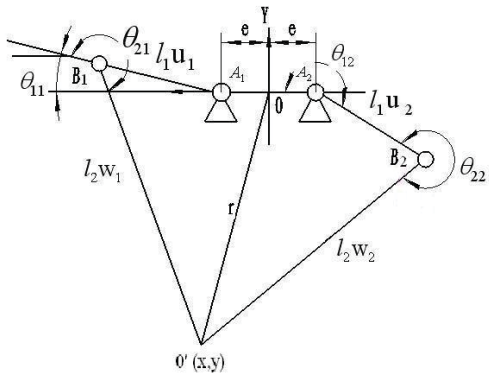

Fig. 2 Sketch of parallel mechanism

The mechanism consists of a five-bar parallel mechanism and two groups parallelogram chain, driven by the arms which connected with the frame, pneuncatic manipulator could achieve two-dimensional translational.

2.2 Trajectory planning

In the process of transplanting bowl seedings, manipulator required two motion process of forward(fetch seeding),return(plant seeding)for each seeding transplanting. While each process, the manipulator would pass through rising, translation, decline three stages. Transplanting assignment requires the manipulator on the rise and decline section must keep a certain distance of straight-line movement, as *AB* and *CD* section shown in Fig. 3, this is because:

1) When fetching seeding in decline, taking seeding rising, planting seeding in decline, return to fetch seeding rising, in order to prevent manipulator and bowl seeding occur interference, need to keep its trajectory and positioning axis parallel.
2) In planting seedling decline section, need to keep the final movement direction downward, make the seeding drop into the hole of plant seeding tray.
3) In return process after manipulator loosen bowl seeding, should maintain a paragraph of vertical rise process, in order to prevent manipulator and falling bowl seedling occur interference.

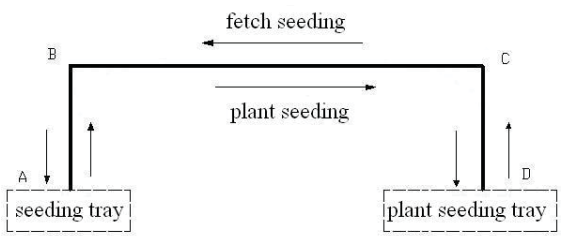

Fig. 3 Manipulator trajectory of transplanting process

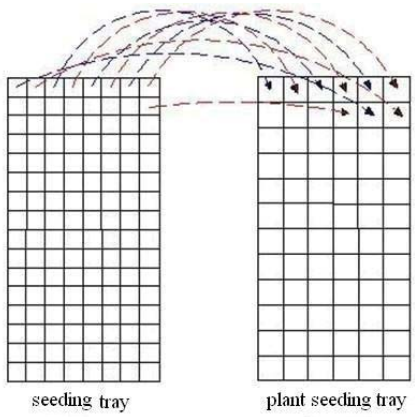

Fig. 4 Transplanting strategic plan

For each straight line track, set motion law of the manipulator is cease, speed up, speed down,cease. So to achieve this rule, must meet the following points:

1) Moving platform velocity and acceleration at the start and end of the trajectory is zero;
2) First and second derivatives of displacement motion law must be continuous;
3) The third-order derivative of the displacement motion law f (the derivative of acceleration) is limited; otherwise it will cause shock; to ensure that the manipulator avoid to be impacted.

2.3 Movement Law Design

In less than a given maximum acceleration condition, base on the movement theory, there are many motion laws to meet the above requirements, such as sine law, cycloidal law, trapezoidal law, quintic polynomial motion law, septic polynomial motion law and so on[4]. Because quintic and septic polynomial are more likely to achieve above motion requirements accurately, therefor, only conduct analysis on them. They are under the condition of known the displacement S and the maximum acceleration $a_{\max}$, the calculation formula is as follows:

1) Quintic polynomial motion law

$$s = \frac{a_{\max}}{5.7735} T^2 \left[10\left(\frac{t}{T}\right)^3 - 15\left(\frac{t}{T}\right)^4 + 6\left(\frac{t}{T}\right)^5 \right] \tag{1}$$

$$v = \frac{ds}{dt} = \frac{30a_{\max}}{5.7735} T \left[\left(\frac{t}{T}\right)^2 - 2\left(\frac{t}{T}\right)^3 + \left(\frac{t}{T}\right)^4 \right] \tag{2}$$

$$a = \frac{d^2s}{dt^2} = \frac{60a_{\max}}{5.7735} \left[\left(\frac{t}{T}\right) - 3\left(\frac{t}{T}\right)^2 + 2\left(\frac{t}{T}\right)^3 \right] \tag{3}$$

$$j = \frac{d^3s}{dt^3} = \frac{60a_{\max}}{5.7735} \left(\frac{1}{T}\right) \left[1 - 6\left(\frac{t}{T}\right) + 6\left(\frac{t}{T}\right)^2 \right] \tag{4}$$

$$T = \sqrt{\frac{5.7735S}{a_{\max}}} \tag{5}$$

2) Septic polynomial motion law

$$s = \frac{a_{\max}}{7.51} T^2 \left[35\left(\frac{t}{T}\right)^4 - 84\left(\frac{t}{T}\right)^5 + 70\left(\frac{t}{T}\right)^6 - 20\left(\frac{t}{T}\right)^7 \right] \tag{6}$$

$$v = \frac{ds}{dt} = \frac{140a_{\max}}{7.51} T \left[\left(\frac{t}{T}\right)^3 - 3\left(\frac{t}{T}\right)^4 + 3\left(\frac{t}{T}\right)^5 - \left(\frac{t}{T}\right)^6 \right] \tag{7}$$

$$a = \frac{d^2s}{dt^2} = \frac{420a_{\max}}{7.51} \left[\left(\frac{t}{T}\right)^2 - 4\left(\frac{t}{T}\right)^3 + 5\left(\frac{t}{T}\right)^4 - 2\left(\frac{t}{T}\right)^5 \right] \tag{8}$$

$$j = \frac{d^3s}{dt^3} = \frac{840a_{\max}}{7.51} \left(\frac{1}{T}\right) \left[\left(\frac{t}{T}\right) - 6\left(\frac{t}{T}\right)^2 + 10\left(\frac{t}{T}\right)^3 - 5\left(\frac{t}{T}\right)^4 \right] \tag{9}$$

$$T = \sqrt{\frac{7.51S}{a_{\max}}} \tag{10}$$

2.4 Simulation Analysis of Motion Law

According to the tray size and seedling size, define the seedling picking mechanical hand horizontal movement distance is 336mm, the up and down movement height is 100 mm, the maximum speed for mobile 3m/s, the maximum acceleration is 30m/s^2, apply the mathematical software MATLAB, get the simulation curves of motion low as Fig. 5 to Fig. 8 shown.

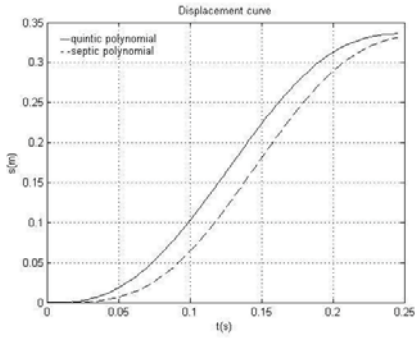

Fig. 5 Displacement curve

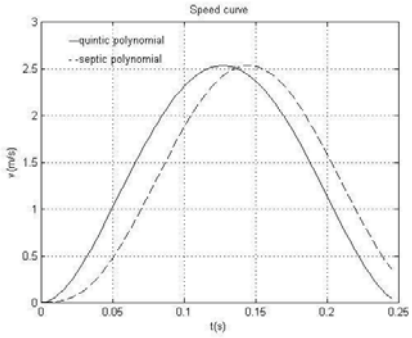

Fig. 6 Speed curve

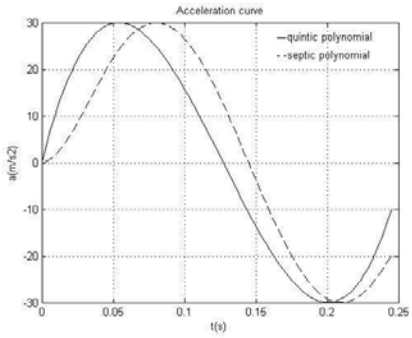

Fig. 7 Acceleration curve

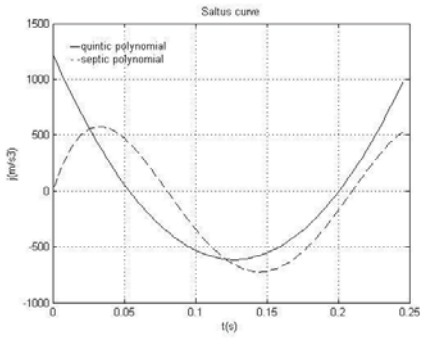

Fig. 8 Saltus curve

From the above charts we can see, quintic polynomial motion law arrive the maximum displacement, velocity, acceleration, spent shorter time, more stable saltus, indicating the saltus of acceleration is smaller;under the condition of the motion laws have the same size of displacement and the maximum acceleration, quintic polynomial motion law uses a shorter time of 0.04s.

In the case of ensure the moving platform smooth operation, select the quintic polynomial motion law as the trajectory function, can greatly reduce the time used in transplanting, improve transplanting efficiency.

2.5 Transplanting strategy

Taking seedling claw from the seedling disc catching seedling, seedling disc movement to the corresponding position placed seedling, again from the seedling disc movement back to the seedling disc 's next target position, such an iterative process, a complete transplanting period, we need to determine transplanting strategy, which determine the path of transplanting.

Based on past experience, tray seedling transplanting path has a variety of options, the mechanism by which a key, as shown in Fig. 4.

The transplanting scheme, seedling transplanting robot on the seedling disc of seedling were progressive transplanting, from right to left, up and down, followed by transplanting to planting after the corresponding position when placed one by one, also with progressive manner, tray spacing between the manipulator, the rise and fall of displacement for 100mm, this 128 holes (8×16) to 72 holes (6 × 12). For example, the 128 hole for the seedling disk disk each row has 8 hole, 72 hole planting trays each row has 6 holes, for the seedling disc every 3 lines just fill the seedling disc 4 lines, as a transfer cycle to study.

Use 5 polynomial motion as taking seedling claw motion control function, send a seedling process bowl Miao Neng bears the maximum acceleration is 30m/s^2, the return of seedling fetching manipulator no-load, maximum acceleration is 60m/s^2, the first mechanical hand transplanting seedling displacement and time as shown in Fig. 1: displacement mm, time s.

Table 1 The first tree transplanting seedling displacement and time

Planting Rise/mm	Planting Level/mm	Planting Fall/mm	Fetch Rise/mm	Fetch Level/mm	Fetch Fall/mm	Periodic Time/s
100	336	100	100	368	100	0.914

And so on, the transplanting time in a cycle is 21.533s, the average of single seedling transplanting time is 0.897s.

3. Active parts of transplanting robot numerical simulation based on the inverse position solution

3.1 Inverse position solution model

Refer to Fig. 2, in a fixed reference system O-xy, build the equation as follows， r represents the dynamic platform vector, $l_1 u_i$ represents active part unit vector, and $l_2 w_i$ represents follower part unit vector, e represents eccentticity, θ_{1i} represents active angle.

$$r - \mathrm{sgn}(i) e e_1 - l_1 u_i = l_2 w_i \tag{11}$$

in which, $u_i = (\cos\theta_{1i} \quad \sin\theta_{1i})^T$, $w_i = (\cos\theta_{2i} \quad \sin\theta_{2i})^T$

$e_1 = (1 \quad 0)^T$, $\mathrm{sgn}(i) = \begin{cases} 1 & i = 1 \\ -1 & i = 2 \end{cases}$

get that: $A_i \sin\theta_{1i} + B_i \cos\theta_{1i} + C_i = 0$

so,

$$\theta_{1i} = 2\arctan\frac{-A_i + \mathrm{sgn}(i)\sqrt{A_i^2 - C_i^2 + B_i^2}}{C_i - B_i} \tag{12}$$

in which,

$$A_i = -2l_1 y$$
$$B_i = -2l_1(x - \mathrm{sgn}(i)e)$$
$$C_i = x^2 + y^2 + e^2 + l_1^2 - l_2^2 - 2\mathrm{sgn}(i)ex$$

3.2 Active part speed and acceleration numerical simulation curves

As Fig. 4 the first tree seedling transplanting is an example, the parameter conditions, procedures for the use of MATLAB inverse simulation, get the following two active numerical parametric curves:

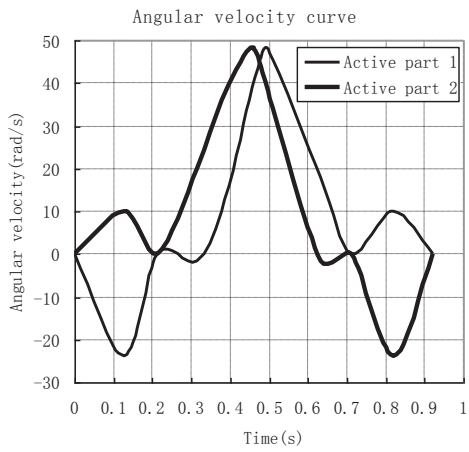

Fig. 9 Angular velocity curve

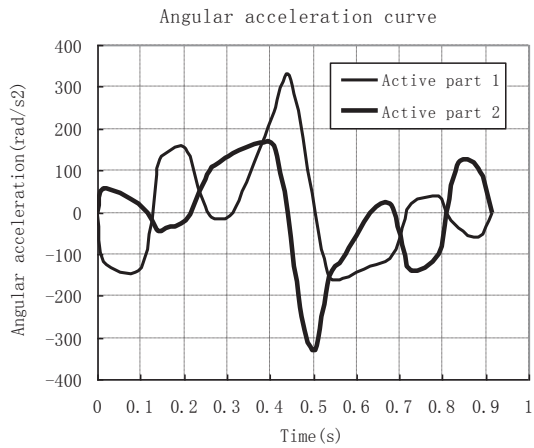

Fig. 10 Angular acceleration curve

Obtained numerical parameters from the above curves, for the control of manipulator prototype, offer the theoretical foundation for optimization design.

4. Base on position inverse for trajectory simulation and verification

4.1 Establish simulation model

In order to verify the rationality of the trajectory planning, conduct kinematic simulation on the key mechanism of the transplanting robot. Mechanical system dynamics analysis software ADAMS is a widely used mechanical motion simulation software, using it to conduct simulation analysis, in order to improve the calculation efficiency, and ensure that the simulation can go smoothly, based on the actual situation to conduct model simplification before the model establishment. In the simplifying process, try to keep the geometry appearance similar with real mechine, and to ensure the quality of the components, centroid position and the accuracy of the moment of inertia. Here establish model by Pro/e software, then import them into ADAMS, add constraints in ADAMS environment, a fixed pair and 16 rotating pair, establish bowl seedlings high-speed parallel transplanting robot simulation model. As shown in Fig. 11:

4.2 Inverse simulation

According to the position inverse solution model，in Adams simulation, using the provided step5 function to achieve the 5 polynomials are created, function $step5(x, x_0, h_0, x_1, h_1)$ is defined as follows:

$$step5 = \begin{cases} h_0 & x \le x_0 \\ h_0 + a\Delta^3(10 - 15\Delta + 6\Delta^2) & x_0 \le x \le x_1 \\ h_1 & x \ge x_1 \end{cases}$$

in which, $a = h_1 - h_0$, $\Delta = (x - x_0)/(x_1 - x_0)$.

As Fig. 4 the first tree transplanting seedling transplanting for example, moving platform in the center of origin at the beginning of transplantation, finally returns to the zero point for a simulation cycle, the moving platform selects a reference point P, impose, direction the displacement constraint of x, y, the constraint functions are established. According to the quintic polynomial motion law, obtain the following simulation parameters, as Table 2 shown.

Table 2 Simulation parameters

Horizontal distance	Vertical distance	Half of the horizontal distance	Horizontal moving time	Vertical moving time	Half of the horizontal distance moving time
336mm	100mm	168mm	0.25s	0.09s	0.15s

So the displacement function of x direction:

step5(time,0,0,0.15,-168)+step5(time,0.33,0,0.58,336)+step5(time,0.76,0,0.91,-168) (13)

The displacement function of y direction:

step5(time,0.15,0,0.24,-100)+step5(time,0.24,0,0.33,100)+step5(time,0.58,0,0.67,-100)

+step5(time,0.67,0,0.76,100) (14)

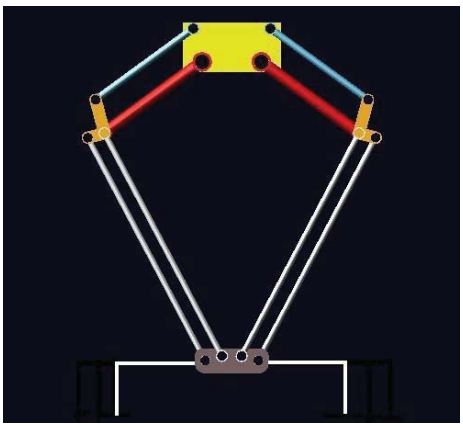

Fig. 11 Moving platform trajectory simulation curve

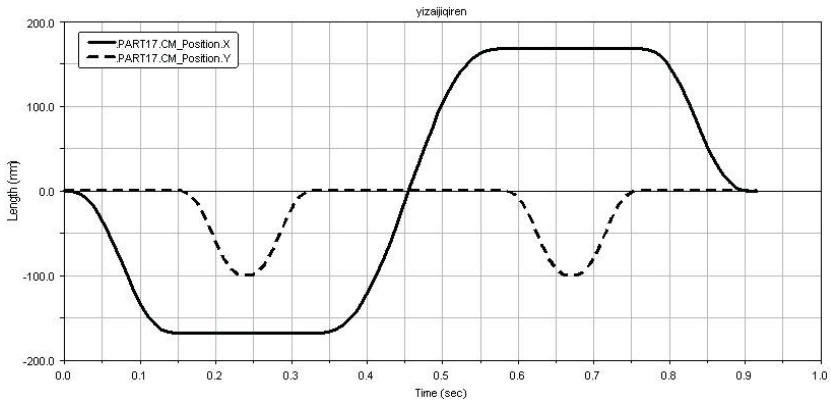

Fig. 12 Transplanting moving platformX, Y direction displacement curve

So far, motion function is established.

Set the simulation time is 1s, the simulation step number step for the 100 steps, a motion simulation, motion of the moving platform trajectory as shown below Fig11 and Fig12.

By the graph can be seen, the seedling picking mechanical hand horizontal movement distance is 336mm, the up and down movement height is 100 mm, the trajectory planning and desired trajectory consistency, illustrate the trajectory planning in the process of get moving platform main input movement rule is correct and reliable, transplanting manipulator according to the planning path to planning, motion stability, embodies the rationality of trajectory planning.

5. Conclusions

(1)The movable needs of the transplanting robot was studied, the formula of inverse kinematics of parallel mechanism was deduced by using the theory of inverse kinematics of the parallel mechanism.

(2)Considered the demand of the “fetch and plant” operations, made an important research on the desired trajectory of the movable platform, and inverse solution simulation by ADAMS, analysis results and planning trajectory are exactly the same.

(3)Inverse solution avoid a lot of calculation and programming work, greatly shorted cycle from virtual prototype to produce product, improve the production efficiency.

(4)Apply quintic polynomial motion law, under a certain condition of motor motion law, the operating cycle to be shorter, meet the requirement of high-speed robot for transplanting, can reduce the transplanting time of 0.04s, improve the transplanting efficiency.

Acknowledgment

This work was financially supported by the Priority Academic Program Development of Jiangsu Higher Education Institutions((Su financial teacher(2011)no.8)，973 Project(2010CB735707), Qing Lan Project of Jiangsu Province (Su teacher (2010)no.27) and Three Engineering of Agricultural Machinery(NJ2008-34).

References

[1] L. C Qiu, S. B Tian, G. H Wang et al. A Seedling Transplanting Autokinetic Machine, China, *Patent of invention*, CN 101663972 A, 2010.3.10.

[2] H.S Yu, T.Z Zhang, L. Yang. Seedling Transplanting Machine Research and Development Prospects, *China Academic Journal Electronic Publishing House*, Vol. N407B, pp. 44-45, 2008.

[3] S.Q Zhang, Y. B Ni, S. F Zong . Trajectory Planning of a High-speed Parallel Manipulator and Numerical Value Simulation, *Design and Research*, Vol. 8, pp. 37-40, 2007.

[4] Z. X Li. The Key Technologies and Prototype Development of a High-speed and Light-weight Parallel Manipulator, *doctoral dissertation*, Beijing, China Agricultural University, 2004.

[5] Z. H Guo, L. S Li, S.H Sun. Trajectory Planning and Simulation on 3-RPC Parallel Mechanisms, *China Mechanical Engineering*, Vol. 18, No. 9, pp. 1036-1038, 2007.

[6] Miller K. Dynamics of the new UWA robot, Proc. *2001 Australian Conference on Robotics and Automation*, pp. 1-6, 2001.

[7] Lallemand J. P, Goudali A and Zeghloul S. The 6 DOF 2 - Delta Parallel Robot, *Robotica*, Vol. 15, No. 4, pp. 407-416, 1997.
[8] Pierrot F and Company O. Parallel Mechanism Machining Device, EP1084802A2, 2000.
[9] Tsai L W. The Enumeration of a Class of Three-DOF Parallel Manipulators, *The 10th World Congress on the Theory of Machine and Mechanisms*, pp.1121-1126, 1999, Oulu, Finland.
[10] Ceccarelli, M., A new 3 D.O.F. Spatial Parallel Mechanism, *Mechanism and Machine Theory*, Vol. 32, No. 8, pp. 895-902. 1997.
[11] Liu X.J., Kim J. and Wang J.S.. Two Novel Parallel Mmechanisms with less than Six DOFs and the Applications, *Proceedings of the WORKSHOP on Fundamental Issues and Future Research Directions for Parallel Mechanisms and Manipulators*, pp. 172-177. 2002, Quebec, Canada.
[12] Ghorbel F.. Modeling and PD Control of Closed-chain Mechanical Systems, *Proc. of IEEE Conference on Decision and Control*, pp. 540-542. 1995, *New Orleans*.
[13] K.C.TING. Automate Flexibly with Robots, *Greenhouse Grower* , Vol. 5, No. 11, pp. 24-28, 1987.
[14] Ji Z.M. Dynamics Decomposition for Stewart Platforms, *Mechanical Design*, Vol. 116, pp. 67-69, 1994.
[15] BorubakisN and KydonasG. An Autonomous Hybrid Robot, *Walking and Climbing. IEEE Robotics and Automation Magazine*, Vol. 11, No. 6, pp. 52-59 , 1998.
[16] W C Choi, D C Kim, I H Ryu, et al. Development of a Seeding Pick-up Device for Vegetable Transplanters, *Transactions of the ASAE*, Vol. 45, No. 1, pp.13-19 , 2002.

Copyright © 2012 DET Corp., Japan All Rights Reserved
International Journal of Comprehensive Engineering
Part C, 2(2), 180-188, 2013
Doi: 10.14270/IJCE2013.2.2.c180
Regular paper

ISSN 2186-2680
e-ISSN 2186-2656
www.iace-journal.org

Shrinkage During Microwave-vacuum Drying for Carrot Slices

Chunfang Song [1,#], Zhengwei Cui [1], Chunyang Li [2], Gelan Qian [1]

[1] Food Engineering & Machinery Group, School of Mechanical Engineering, Jiangnan University, Wuxi, 214122, China
[2] The Institute of Agro-products Processing, Jiangsu Academy of Agricultural Science, Nanjing, 210014, China

[#] Corresponding author: gracecf927@163.com; Tel.: +86-510-8591-0390; Fax: +86-510-8591-0390

Abstract: The effects of microwave-vacuum (MWV) drying on shrinkage and moisture content of carrot slices at various thicknesses were investigated, and the parameters were optimized by response surface methodology. In MWV drying, drying rate improved with the increase of microwave power density and vacuum, and with the decrease of thickness. Shrinkage decreased with the raising of thickness. Both higher or lower microwave power influenced the final quality of carrots. The optimal parameters were obtained as following: 2.55W/g microwave power density and 7mm thickness is fit for high shrinkage and low energy consumption. The shrinkage is 47.347% correspondingly. It proves that MWV drying is very effective for improving quality of carrots and shortening the drying time.

Keywords: Shrinkage, Moisture Content, Carrot, Microwave-vacuum Drying.

Received: May 22,2012 / Accepted: Feb. 20,2013 / Published: Jul. 5,2013

1. Introduction

Shrinkage of food stuffs is a common physical phenomenon occurred during different dehydration processes. It usually has a negative consequence on the quality of the dehydrated product. Changes in shape, loss of volume and increase of hardness give a bad impression to the consumer. The high-quality dehydrated food should preserve the primal nutritional and physical properties of the initial fresh product farthest. Therefore, a thorough understanding of the factors responsible for degradation in the physical quality of the product during the drying process is thus of major relevance.

Shrinkage is one of the most important physical changes, resulting in the stresses in the cellular structure of the food, alteration of the shape and decrease in dimensions. All the non-puffing dehydration processes will create a more or less collapsed dried product. Shrinkage varies according to the type of process and process conditions. Furthermore, the degree of shrinkage and bulk density is usually correlated with the firmness and external appearances which are also important to the consumer. The freeze-dried products have little shrinkage or no loss in sensory qualities, therefore it may avert the shrinkage problem. However, freeze-drying under non-optimal conditions also lead to collapse [1]. Because not all products are economically feasible to freeze-dry, it is essential to be able to modify the physical properties of dehydrated foods by using other dehydration methods.

Conventional hot-air drying (fluid bed drying, tray drying, etc.) is one of the most frequently used operations for food dehydration. Besides the poor-quality of products, low energy efficiency and lengthy drying time, the final products are characterized by small porosity and high apparent density values. The mathematical models for shrinkage in convective drying of food materials were divided into empirical models (including linear models and exponential models) and fundamental models [2-3]. Linear models are adequate to describe materials and process conditions leading to negligible porosity development during the drying process, or to uniform development of porosity, corresponding to a linear decrease of volume in the whole range of humidity. If the development of porosity increases sharply during the final stage of drying, linearity is lost and the behavior is best described by

exponential models. The fundamental models are based on the mass balances, density, porosity definitions and volumes of the different phases in the system. The mathematical model of fruits and vegetables dehydrating has been established before [4].

Microwave-vacuum (MWV) drying is one of many advanced drying techniques that have been used to preserve perishable fruits and vegetables. Quality characteristics of MWV drying products have been reported comparable to those of freeze-dried products [5-11].

Little information and data currently exist on shrinkage of MW drying of vegetables or fruits. Therefore, the objective of this study is to investigate the effect of main process variables such as sample thickness, microwave power density and vacuum, on shrinkage and moisture content of carrot slices. Experimental results will provide some theoretical basis for drying of carrots.

2. Materials and methods

2.1 Drying equipment

The MWV dryer of lab scale(Fig.1) in which the materials to be dried can be rotated in the cavity was developed by the authors [9]. The actual measured full-power output of magnetron was 360 W. The microwave-vacuum dryer was operated at 2.5 kPa (absolute pressure), and the rotation. Speed of the turntable was 5 rpm.

Fig. 1 MWV dryer of lab scale

2.2 Materials

Fresh carrots and apples were purchased from the local market in Wuxi, China. The carts were trimmed, scraped, washed and cut into 4-8 mm slices with the diameter of about 40 mm. The initial moisture content of the carrot was 11.21 (dry basis) measured according to the vacuum oven method [12]. Before drying, the carrot samples were weighed by an electronic balance (Model MP2000D, Shanghai Electronic Balance Instrument Co. Ltd., Shanghai, China). Each sample was spread in a single layer in a dish made of tetrachloroethylene.

2.3 Shrinkage capacity

2.3.1 Specific volume measurements

Shrinkage or collapse was defined as the decrease in specific volume or increase in bulk density, and was measured using the glass beads displacement method of Levi & Karel [1] with some modification. An empty 50 ml beaker was weighed using an electric balance. The vial's beaker was filled with water (20℃) and weighed, assuming water density, ρ , to be 1 g/ml, the additional weight gave the volume of the empty vials. The average of the beaker volume and weight was determined. An empty beaker, filled to the brim with glass beads (Lab Glass, 200 μm), was weighed, maintaining a flat surface, and leveled off using a glass rod. Then, 3-4 pieces of samples were embedded into the beaker and leveled off again. The removed beads were collected and weighed. The volume measurements were done in triplicate.

Bulk density of the glass beads in the vial was calculated as:

$$\frac{W_B - W_V}{V_V} = \rho_B \tag{1}$$

Where W_B is the weight of the beaker filled with beads (g), W_V is the weight of the empty beaker (g), W_W is the weight of the beaker filled with water (g), V_V is the volume of the vial (ml) $= W_W - W_V$, ρ_B is the bulk density of the beads (g/ml).

Matrix samples were weighed, and their volumes were determined using the following equation:

$$\frac{W_B - (W_T - W_s)}{\rho_B} = V_S \tag{2}$$

Where W_T is the total weight of the beaker, the sample and the beads (g), W_S is the weight of the sample [weight of (vial+sample)- W_V] (g), V_S is the volume of the sample (ml).

2.3.2 Shrinkage capacity

Volume changes due to sample shrinkage were measured by beads' displacement method as described above., area or thickness. The shrinkage/volume change of the samples was expressed as a bulk shrinkage ratio of sample volume at any time to initial volume [13].

$$S_v = \frac{V_s}{V_0} \tag{3}$$

2.4 Drying procedure

(1)MWV drying

The spread slice rotated with the turntable and then the appropriate experimental conditions (vacuum and microwave power) were imposed. For each experiment, the vacuum was interrupted and the sample was taken out and then weighed by electronic balance every 10 min and the sample was dried until the moisture content was less than 0.33-0.40 (dry basis) (continuous drying experiment on similar weight was conducted to examine the effect of this interruption during drying on weight loss and it was found the effect was negligible). All the measurements were taken within 1 min. The moisture of the dried sample at the end of every drying period was calculated according the loss of weight and value of initial moisture content. Compared to the evaporation heat, the sensible heat loss due to the above interruption was small and could be neglected.

Microwave–vacuum drying experiments were carried out for five levels of microwave power density(2.1 w/g, 2.4 w/g, 2.7 w/g, 3.0 w/g. 3.3 w/g) and three levels of vacuum pressure (-0.085 MPa, -0.090 MPa, -0.095 MPa). The lower power levels were obtained with the magnetron being cycled between on and off. Three replicates were carried out for each experiment, and the mean value moisture content and shrinkage at each experimental point were determined.

3. Results and discussion

3.1 Parameter's analysis of MWV drying

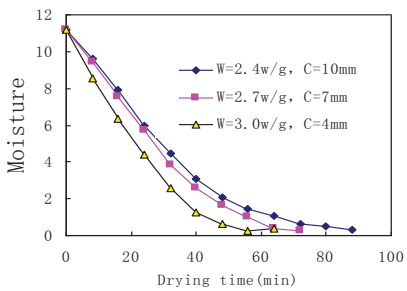

Fig. 2 Drying of carrots in different microwave power density and different sizes(-0.95MPa vacuum degree)

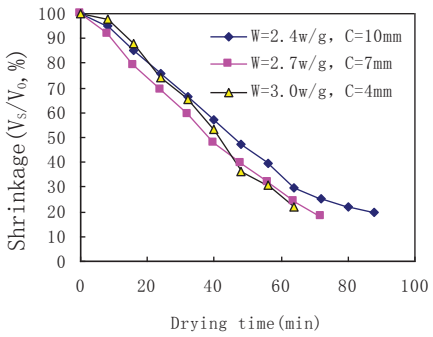

Fig. 3 Shrinkage of carrots in different microwave power density and different sizes(-0.95MPa vacuum degree)

There are three factors for MWV drying, microwave power intensity, vacuum and slice size (thickness) of carrots respectively. Drying and shrinkage of carrots with different sizes in different microwave intensities can be seen from Fig. 2 and Fig. 3 with the vacuum degree as -0.95 MPa. The changes in shrinkage and moisture with the drying time show the same trend. There is an intersection of the shrinkage curves in the middle of drying time, which shows that effects of technological parameters may be different under varied conditions on the shrinkage of carrots.

In the initial stage of drying carrots, moisture content of carrots fell sharply and most of the water quickly evaporated in a short time. Only small amount of water was lost later. According to the moisture curve, dry process is divided into constant speed drying stage and falling rate drying stage. Before 45 minutes, it was in the constant speed drying stage for straight line down the slope. 45 minutes later, carrot moisture content declined gently as in the falling rate drying stage.

In constant speed drying stages, moisture content of carrots is high. Solid skeleton of material is soft and in the viscoelastic state, which is prone to deformation. During this stage, the volume of material shrinkage tend to compensate for loss of water. Shrinkage and moisture content is homogeneously in the linear correlation. The length, area and volume of carrots are reduced uniformly to the proportion. In falling rate drying stage, drying process is affected by vacuum, microwave power and size and shape of materials. Solid materials are turned to glass state from viscoelastic state [14]. In the vacuum state, drying rate is higher on the surface layer of carrot which dries more quickly than in the center. Thin film is formed accordingly. When the center is dried and contracted, interior part of carrots will separate from dry film, cracks inside material, the gap and the honeycomb structure will appear.

3.2 Effects of factors on drying of carrots in MWV drying

3.2.1 Effects of different microwave intensity on drying of carrots

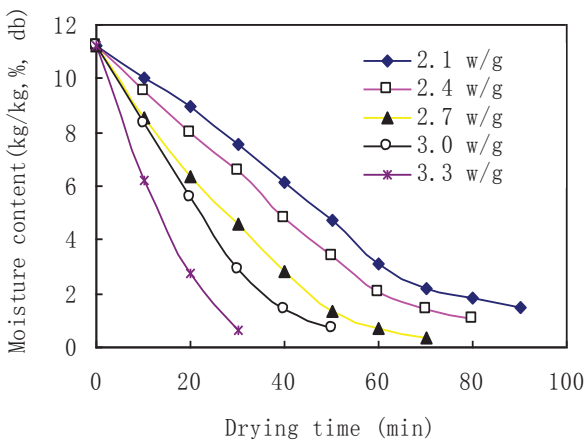

Fig. 4 Moisture content of different microwave power density for carrots slice (4 mm thick and 0.95MPa vacuum)

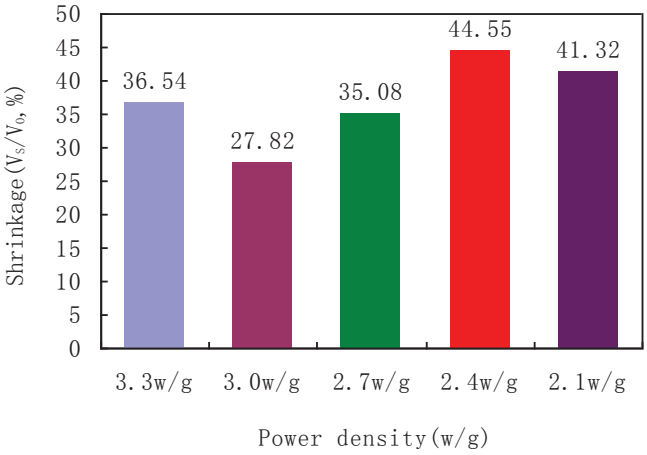

Fig. 5 Shrinkage of carrots slices in different microwave power density (4 mm thick and 0.95MPa vacuum)

In the drying process of carrots, there are two kinds of water diffusion, inside diffusion and outside diffusion respectively. The two moisture transfer forms in the drying process usually exist at the same time. Speed of inside and outside diffusion is different for drying time, shape of materials and drying intensity. For the thin slice of fruits and vegetables, the diffusioning spread of insterior water is usually higher vaporizing rate of surface's water. Drying rate is determined by vaporizing rate of surface water, called the external control phenomenon. The vaporizing rate of water in surface is mainly affected by drying intensity. As a result, drying rate can be improved by increasing drying intensity.

Source of heat for microwave vacuum drying is microwave energy only, so drying intensity depend on the value of microwave power density. Moisture content changed with different microwave density was given in Fig.3. The drying time was reduced with the increase of microwave power density. Less than 30 minutes drying time was required under the condition of 3.3 w/g power density. It took more than 90 minutes drying time when power density is 2.1W/g. Shrinkage of carrots in different microwave power density was compared in Fig.4. If power density is too high, the quality of carrots will be severely influenced.

When power density was 3.3W/g, deformation, puffing and burnt phenomenon appeared. During the later drying stage, a layer of hard film arose on surface of carrots, which prevent further moisture evaporation. Though lower density power was helpful to keep carrots' shape, it was difficult to achieve the safe moisture content required. Both higher or lower microwave power would influence the final quality of carrots.

3.2.2 Effects of different vacuum on drying of carrots

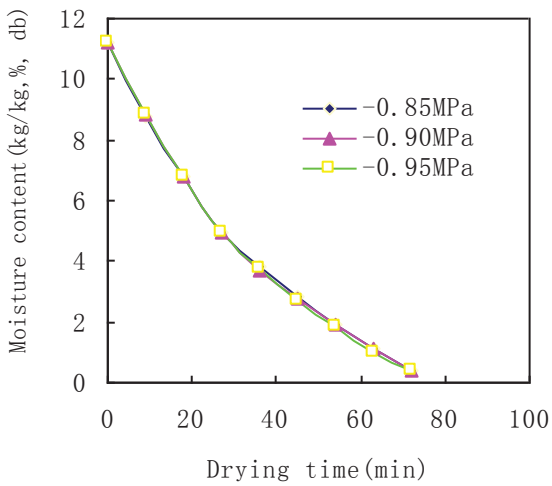

Fig. 6 The influence of different vacuum degree(4mm thickness. and 2.7w/g power density)

It can be seen from Fig. 6 that the drying rate was only slightly higher with the increase of vacuum of MWV rig. Vacuum had not significant effects on drying of carrots. Consequently, vacuum could be neglected in this study, and 0.95 MPa vacuum degree was fixed in the later experimental study.

3.2.3 Effects of different sizes on drying of carrots

As shown in Fig.7, shrinkage decreased with the increased thickness. Drying rate was improved with the decrease in the thickness of carrots, whereas thick carrots took long time to dry. In the process of drying carrots, proper power density should be chosen to dry carrots of different thickness so as to dry carrots quickly to the safe moisture content in a short time.

In drying carrots by MWV drying method, the resistance to mass transfer is related to the thickness of slices and drying stage. Resistance of inside and outside mass transfer could be inadvertent when the thickness of carrots slice was less than the critical thickness. The temperature inside the sample was uniform until the critical moisture content was achieved. From the experimental result, critical thickness of carrots was 8 mm. Moreover, 8 mm thickness of carrots showed to be best for deceasing shrinkage and maintaining the shape in drying stage.

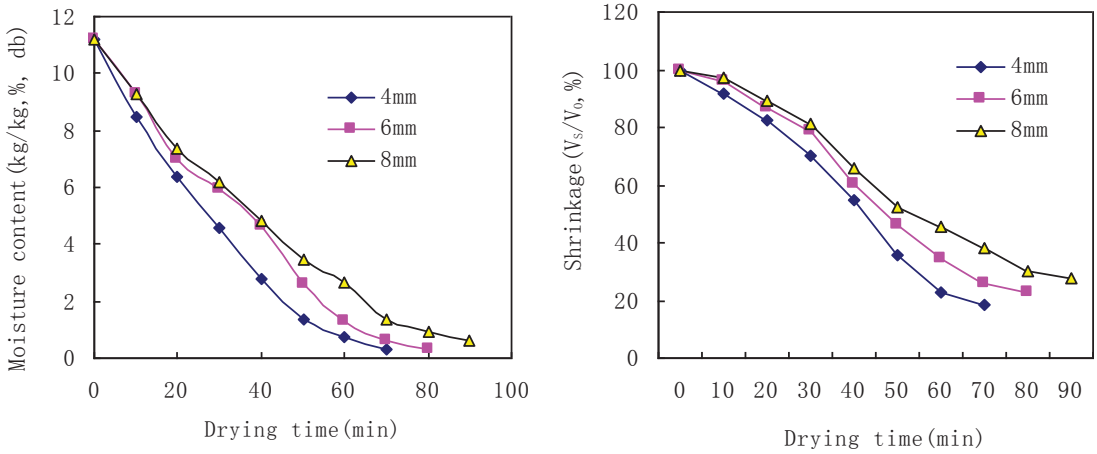

Fig. 7 Effects of different thickess on drying of carrots(-0.95MPa vacuum degree, 2.7w/g power density)

3.3 Combined effect of factors by RSM

In conclusion, Shrinkage is the function of microwave power density, size of material and mosture contents, while the moisture content is also the function of time.

3.3.1 Experimental design

Response surface methodology (RSM) was used to analyze the shrinkage of carrots in VMM drying. Experimental design and statistic analysis was conducted using SAS software. The variable factors with the coded and actual values are presented in Table 1. An orthogonal-central composite design was chosen to evaluate the combined effect of two independent variables, microwave power density and sizes of carrots, coded as X_1 and X_2 respectively. The maximum and minimum values for microwave power density were set at 2.4w/g and 3.0 w/g, while the sizes of carrots were at 4mm and 8mm. The responses measured were shrinkage of carrots. The complete design consisted of 10 combinations (Table 2). All experiments were carried out in a randomized order to minimize the effect of unexplained variability in the observed responses due to extraneous factors [15].

The responses function (Y) was partitioned into linear, quadratic and interactive components (Mengal & Mompon, 2006).

$$Y = \beta_0 + \sum \beta_i X_i + \sum \beta_{ii} X_i^2 + \sum \beta_{ij} X_i X_j \tag{4}$$

Where β_0 is defined as the constant, β_i the linear coefficient, β_{ii} the quadratic coefficient and β_{ij} the interactive coefficient ; X_i and X_j are levels of the independent variables. The analysis of variance (ANOVA) tables were generated and the effect and regression coefficients of individual linear, quadratic and interaction terms were determined. The significances of all terms in the polynomial were judged statistically by computing the F-value at a probability (p) of 0.01 or 0.05. The regression coefficients were then used to make statistical calculations to generate contour maps from the regression models.

3.3.2 Experimental Analysis

R^2 is defined as the ratio of the explained variation to the total variation and is a measure of the degree of fit. It is also the proportion of the variability in the response variables, which is accounted by the regression analysis. The more R^2 approaches' unity, the better the empirical model fits the actual data [16].

From the variance analysis，the R^2 value was 0.9792, the regression model was highly significant (P <0.01) (Table 4), showed the model fit well. It means that the regression equations can replace the actual experimental data for analysis of the result.

From the ANOVA of the regression equation (Table 3), linear item in the equations was highly significant (P<0.001).. Effects of microwave power density (P<0.001) on shrinkage of carrots was greater than that of thickness (P<0.01) (Table 4). The regression model relating to the effects of microwave power density and thickness on the shrinkage of carrots was correspondingly obtained as follows:

$$S_{V1} = 32.157143+5.85X_1-7.98333X_2+0.235714X_1^2+2.035714X_2^2-1.175X_1X_2 \quad (R^2=0.9792) \quad (5)$$

Table 1 Factors and levers of RSM

Level factor	-1	0	1
Thickness X_1 （mm）	4	6	8
Microwave power density X_2 (W/g)	2.4	2.7	3.0

Table 2 Test design and results of RSM

Number	Thickness X_1	Microwave power density X_2	Shrinkage S_V（%）
1	0	-1	42.9
2	0	0	30.3
3	0	1	27.7
4	-1	-1	35.5
5	-1	0	26.7
6	-1	1	21.5
7	1	-1	48.6
8	1	0	40.3
9	1	1	29.9
10	0	0	31.8

Table 3 Variance analysis of carrot's shrinkage

Source	SS	DF	MS	F value	P value
Linear item	587.736667	2	293.868	91.45	0.0005 ***
Square item	5.522500	1	5.5225	1.72	0.3039
Interactive term	10.463143	2	5.2315	1.63	0.2601
Regression	603.722310	5	120.744	37.58	0.0019 **

SS = sum of squares, DF = degrees of freedom, MS = mean square.

*** P<0.001，** P<0.01，* P<0.1

Table 4 Estimated value of regression coefficient in regression equation

Source	coefficient	Standard error	T Value	Possibility bigger than | T |
intercept	32.157143	1.071285	30.02	<.0001
X_1	5.850000	0.731827	7.99	0.0013
X_2	-7.98333	0.731827	-10.91	0.0004
$X_1 X_1$	0.235714	1.173534	0.20	0.8506
$X_1 X_2$	-1.175000	0.896301	-1.31	0.2601
$X_2 X_2$	2.035714	1.173534	1.73	0.1578

R^2 =0.9792

By analysis of the regression equation, Matlab software was run to get response surface and contour map for shrinkage of carrots(Fig.7).

From Fig.8, there is a negative correlation between shrinkage of carrots and microwave power density in MWV drying, while a positive correlation between shrinkage of carrots and thickness. Shrinkage is higher with the decreased microwave power density and the increased slice thickness. The maximum value is achieved at the point with 2.4W/g microwave power density and 8 mm thickness, coded as minimum level of microwave power density and maximum level of thickness. From the analysis of single factor experiment, the drying time becomes too much longer when the microwave power density is too small and the thickness is too big. Therefore, the maximum point is unsuitable. 2.55W/g microwave power density and 7mm thickness (the orange section in Fig.7) is fit for high shrinkage and low energy consumption. The shrinkage is 47.347% correspondingly. Actual shrinkage of carrots in the experiment was 46.693%. The relative error between theoretical and actual value is 0.0144%.

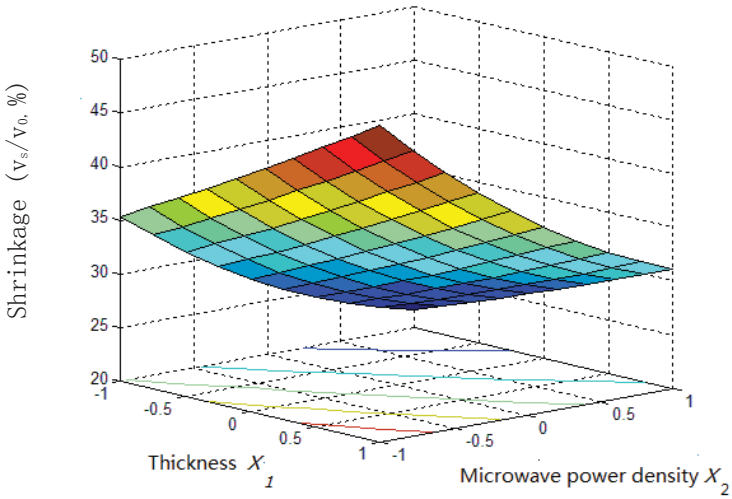

Fig. 8 Response surface of shrinkage for carrots slice
(red: highest value, blue:lowest value From red to blue, the value decrease.)

4. Conclusions

For the MWV drying, drying rate improved with the increase of microwave power density and vacuum, and with the decrease of thickness. Shrinkage decreased with the raising of thickness. Vacuum did not have significant effects on drying of carrots. Both higher or lower microwave power would influence the final quality of carrots. 0.95 MPa vacuum level was suitable for MWV drying.

Optimization results showed the maximum point is unsuitable. 2.55W/g microwave power density and 7mm thickness fit for high shrinkage and low energy consumption. The shrinkage is 47.347% correspondingly, while the ctual shrinkage of carrots measured was 46.693%. The relative error between theoretical and actual value is 0.0144%. It can be concluded that the MWV drying is very effective for improving quality of carrots and shortening the drying time.

Acknowledge

This work is financially supported by Program for Innovative Research Team of Jiangnan University (PITJiangnan), the Fundamental Research Funds for the Central Universities （JUSRP211A14）and 2010 Mechanical Engineering College's own project of Jiangnan University.

References

[1] G. Levi and M. Karel. Volumetric Shrinkage (Callapse) in Freeze-Dried Carbohydrates Above Their Glass Transition Temperature, *Food Research International*, Vol. 28, No. 2, pp. 145-151, 1995

[2] M.K Krokida, V.T Karathanos and Z.B Maroulis. Effect of Freeze-Drying Conditions on Shrinkage and Porosity of Dehydrated Agricultural Products, *Journal of Food Engineering*, Vol. 35, 369-380, 1998.

[3] L. Mayor and A. M Sereno. Modelling Shrinkage During Convective Drying of Food Materials: A Review, *Journal of Food Engineering*, Vol. 61, pp. 373-386, 2004.

[4] J. E Lozano, E Rotstein and M.J Urbicain. Total Porosity and Open-Pore Porosity in the Drying Of Fruits, *Journal of Food Science,* Vol. 45, pp. 1403-1407, 1980.

[5] T. M Lin, T. D Durance and C. H Scaman. Characterization of Vacuum Microwave, Air and Freeze Dried Carrot Slices, *Food Research International,* Vol. 31, No. 2, pp. 111-117, 1998.

[6] A. N Yousif, T. D Durance, C. H Scaman and B. Girard. Headspace Volatiles and Physical Characteristics of Vacuum-Microwave, Air, and Freeze-Dried Oregano (Lippia Berlandieri Schauer), *Journal of Food Science,*Vol. 67, No. 6, pp. 926-930, 2000.

[7] P. W. Sham, C. H. Scaman and T. D Durance. Texture of Vacuum Microwave Dehydrated Apple Chips as Affected by Calcium Pretreatment, Vacuum Level, and Apple Variety, *Journal of Food Science,* Vol. 66, No. 9, pp. 1341-1347, 2001.

[8] T. D Durance and J. H Wang. Energy Consumption, Density, and Rehydration Rate of Vacuum Microwave- and Hot-Air Convection-Dehydrated Tomatoes, *Journal of Food Science,* Vol. 67, No. 6, pp. 2212-2216, 2002.

[9] Z. W Cui, S. Y Xu and Z W Sun. Effect of Microwave-Vacuum Drying on the Carotenoids Retention of Carrot Slices and Chlorophyll Retention of Chinese Chive Leaves, *Drying Technology,* Vol. 22, pp. 563-575, 2004.

[10] M. K Krokida and Z. B Maroulis. Effects of Microwave Drying on Some Quality Properties of Dehydrated Products, *Drying Technology,* Vol, 17, pp. 449-466, 1999.

[11] M. A. M Khraisheh, T. J. R. Cooper and T. R. A Magee. Shrinkage Characteristics of Potatoes Dehydrated under Combined Microwave and Convective Air Conditions, *Drying Technology,* Vol. 15,No. 3/4, pp. 1003-1022, 1997.

[12] AOAC. *Official Methods of Analysis of AOAC International (16th ed.),* Association of Official Analytical Chemists, 1995.

[13] M.Maskan. Drying, Shrinkage and Rehydration Characteristics of Kiwifruits During Hot Air and Microwave Drying, *Journal of Food Engineering* , Vol. 48, pp. 177-182, 2001.

[14] M. K Krokida and Z. B Maroulis. Effect of Drying on Shrinkage and Porosity, *Drying Technology,* Vol. 15, pp. 2441-2458, 1997.

[15] U. N Wanasundara and F. Shahidi. Antioxidant and Pro-oxidant Activity of Green Tea Extracts in Marine Oils, *Food chemistry,* Vol. 63, No. 3, pp. 335-342, 1998.

[16] T. M Little and F. J Hills. *Agricultural Experimental Design and Analysis,* John Wiley, 1978.

Copyright © 2012 DET Corp., Japan All Rights Reserved
International Journal of Comprehensive Engineering
Part C, 2(2), 189-195, 2013
Doi: 10.14270/IJCE2013.2.2.c189
Regular paper

ISSN 2186-2680
e-ISSN 2186-2656
www.iace-journal.org

Identifying Weeds in Cotton Field with Morphological Skeleton

Hanping Mao [1, #], Bo Hu, Shicha Zheng [1], Zhongping Xiang

Key Laboratory of Modern Agricultural Equipment and Technology，Ministry of Education & Jiangsu Province, Jiangsu University, Zhenjiang 212013, China

#Corresponding author: maohp@ujs.edu.cn

Abstract: Studies that identify weeds with machine vision are being encouraged by concern over reducing herbicide use in precision farm. Some researches have been claimed as successful weeds identification with leaf shape features, but apparently have only been tested against concrete plant without serious overlapped leaves. A novel method based on morphological skeleton for identifying nature weeds images including serious overlapped leaves is proposed. The images of weeds are firstly segmented by colour index, secondly the binary image is divided into the plant area and weed area with erosion operation, and then identified by the ratio of skeleton length and leaf area. Images include cotton, common crabgrass, shepherd's-purse and so on. A comparison of the identification precisions whose segmentations are processed via three different indexes was conducted. It has been found that segmentation precision does not concern identification precision deeply. The new method can give an active effect on identifying weeds from plants even with the serious overlapped leaves.

Keywords: Identification, Weed, Morphological Skeleton, Overlapping.

Received: May 12,2012 / Accepted: Feb. 20,2013 / Published: Jul. 5,2013

1. Introduction

Using machine vision to identify weed and develop weeding system has been important in modern agriculture to improve environment. Among the existing researches, the main identification feature is the plant leaf shape. In 2005, Søgaard identified weed using shape models(S¢gaard, 2005)[1]. In 2006, Jo˜ao Camargo Neto used Elliptic Fourier and discriminant analysis to identify weeds in soybean field（Neto et al.,2006）[2]. The above methods are conducted based on leaf outline; however, the overlapping of leaf can change its outline, which will directly affect the extraction of shape feature. And the effects will become more and more serious when weeds and plants are growing up. There is a method using the differences of leaf edge to figure out the outline of un-overlapped leaves, but the resulting shape index greatly differs the real value, and reduces the precision of identification. In 2000, Chapron identified the accompanying weeds from corn by syncretizing multiple features, and it showed a satisfactory result when the overlapped leaves are less than 5%, however this method does not work well when the leaves are seriously overlapped(Chapron et al.,2000)[3]. In 2002, R.D.Lamm identified gramineous weeds in cotton field by morphological operators of erosion and dilation, and gave sound precision, but not well adapted to plant with serious overlapped leaves(Lamm et al.,2002)[4]. In 2010, Li X.F. segemented cotton and crabgrass images by opening operators when the leaf shapes of weed and crop are quite different, and small overlapped. But also not segemented the serious overlapping leaves by the general morphological operators(Li et al.,2010)[5].

In cottons production, weeds can grow rapidly at several growing stages, and plants do not grow better than weed. So generally, it is more necessary to weed when leaves are seriously overlapped in cotton fields.

While classifying species of plants, the authors always analyze the whole plant instead of complete leaves. It will be more practicable to identify weed at the whole plant (i.e. above-ground plant parts) than to leaves on certain growing stages. And the new shape features will be extracted on the base of the differences of plants. This paper introduces morphological skeleton feature to identify the accompanying weeds from cottons that have overlapped leaves.Trajectory planning of bowl seeding transplanting robot.

2. Morphological feature extraction

Cotton is Malvaceae, Gossypium L, simple leaf alternated. It is hard to identify cotton and weed by the conventional shape features, such as the ratio of width to length and the completeness because of overlapping. When the cottons grow to a certain stage, the area of leaves becomes larger than weed, and the spans between overlapped leaves are getting smaller. Moreover, the weeds accompanying cotton are Common Crabgrass, Setaria Viridis and Portulaca Oleracea, etc, although they are overlapped, there always are spans among them and the overlapped edges are of no regularity. It shows that the images of weed plants are more complicated than those of the cotton within the same area. This can be demonstrated by leaf area index that is the multiple of total leaf area to its growing soil area. The leaf area index of cotton generally ranges from 2 to 4; while weed much less than 1. In mathematical morphology, skeleton is a key feature to reflect such differences between cotton and weed.

The two basic operators of mathematical morphology are erosion and dilation, X is the processed image and S is the structure element, and it is shown that:

$$E = X\Theta S = \left\{ x, y \middle| S_{xy} \subseteq X \right\} \tag{1}$$

$$D = X \oplus S = \left\{ x, y \middle| S_{xy} \cap X \neq \varnothing \right\} \tag{2}$$

where E is erosion, D is dilation, x, y is pixel position coordinates.

Skeleton can be expressed in terms of erosions and dilations, it can be shown that[6]:

$$Z(X) = \bigcup_{k=0}^{K} Z_k(X) \tag{3}$$

$$Z_k(X) = \bigcup_{k=0}^{K} \left\{ (X\Theta kS) - \left[(X\Theta kS)\Theta S \right] \oplus S \right\} \tag{4}$$

Where k is the times of iteration; when K is the last iterative step, X erodes to an empty set; the symbol indicates that X is successively eroded by S for k times. The structure element is S= $\begin{bmatrix} 1 & 1 & 1 \\ 1 & 1 & 1 \\ 1 & 1 & 1 \end{bmatrix}$.

The binary skeleton images of cotton and Common Crabgrass are as shown in Fig. 1.

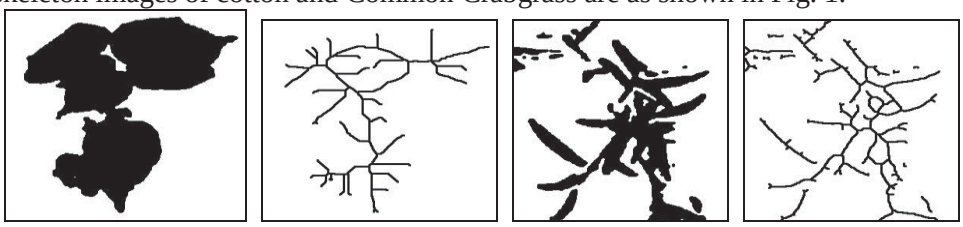

(a)Cotton (b)Cotton skeleton(c) Common Crabgrass (d) Common Crabgrass skeleton

Fig. 1 Morphological skeleton

Obviously, within the same leaf area, the length of Common Crabgrass skeleton is much longer than that of cotton, so we take the ratio of skeleton length to leaf area as an identification feature.

3. Identification

The original image is acquired from field, including cotton, weed and background, at first, it is necessary need to segment background. The original color digital image is an RGB image; each RGB color pixel is a combination of tristimuli R (red), G (green) and B (blue), which are usually called tree primary colors. The range of the value of tristimuli relies on the memory pattern. Within one full- color image, each pixel is said to have a depth of 24bits, and each color component has 8 bits, therefore each component has a grayscale of 256 (28). To segment is to find a decent feature. In 1995, Woebbecke proposed an excessive green index (2g-r-b) to segment weed images, and he also analyzed other color indexes of r-b、g-b、(g-b)/(r-g) and H, and finally among

them, the index (2g-r-b) was found to be the optimum one(Woebbecke et al.,1995)[7]. Among the existing researches, this index has been widely accepted as the most major feature to segment weed image. In 2002 and 2003, Yang developed an auto-weed system in which green color G was taken as the index to segment weed images. Namely, pixels that have its green value G higher than 40 are regarded as the plant, others are the background(Yang et al.,2002,2003)[8,9], this method is pretty simple, but the threshold is not always 40, it has bearing on the environment. So the author finds an optimal index that is -149R+218G-73B by doing lots of experiments using a genetic algorithm(Mao et al.,2007)[10]. This paper utilizes the above three indexes to segment the weed image and analyzes the segmentation errors, as well as their effects on identification.

The operator of skeleton is based on binary image, so herein we suppose that plant area is as 1, and background 0. Erosion is applied to divide the cotton and weed in order to get both skeleton images, and then identify the weed and cotton by the ratio of skeleton length to leaf area. The skeleton length is approximately equal to the total number of skeleton pixels. Similarly, the leaf area is equal to the total number of leaf pixels. The identification algorithm is as the followings:

Step1: segment background to get a binary image;

Step 2: erode the binary image to divide areas of plants and weeds

Step3: morphological skeleton

Step4: figure out the ratio of skeleton length to leaf area, and to identify cotton from weed

4. Results and conclusions

The images of cotton and its accompanying weeds are acquired by Sony DSC-V1 in the greenhouse in Jiangsu University, Zhenjiang city in Jiangsu province in 7th, Oct 2005. The digital camera has a vertical distance about 110cm from the ground. The main accompanying weeds in the images are Digitaria sanguinalis (L.) Scop., Capsella bursa-pastoris (L.) Medic, Trigonotis peduncularis (Trev.) Benth.ex Baker et Moore, and Oxalis corniculata L, of which the Digitaria sanguinalis and Capsella bursa-pastoris are major accompanying weed. The Fig. 2 shows a weed and cotton image; Fig. 3 shows segmentation results via three indexes (white pixels indicate background; plant remains the same color as in Fig. 2); Fig. 4 shows skeleton image (black pixels indicate skeleton; and white others); and Figure 5 shows the identification result (where pixels identified to be weeds are red colored; and the plant pixels remain the same color as in Fig. 3).

As shown in the Fig. 3(a), an excess green index will take parts of background pixels as plant; In Fig. 3(b) quite few pixels of background are taken as plant, but a few pixels of plant are taken as background, which will affect the completeness of plant; In Fig. 3(c) the segmentation is relatively better. The authors find all the three features can almost identify weed but there are certain identification errors from Fig. 5. The areas marked with the black circle in Fig. 5(a) and Fig. 5(b) indicate that several cotton leaves are identified as weed; and the

Fig. 2 Cotton and weeds

(a) Excess green index (b) G index (c) Optimal index

Fig. 3 Segmentation results via different indexes

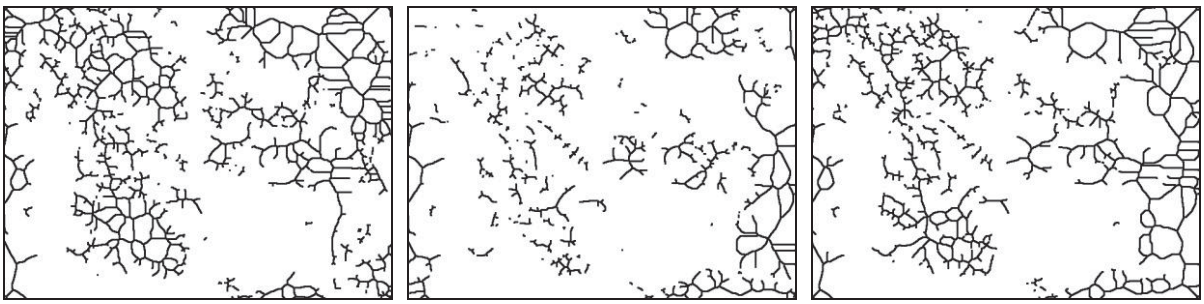

(a) Excess green index (b) G index (c) Optimal index

Fig. 4 Skeleton of segmentation results with different indexes

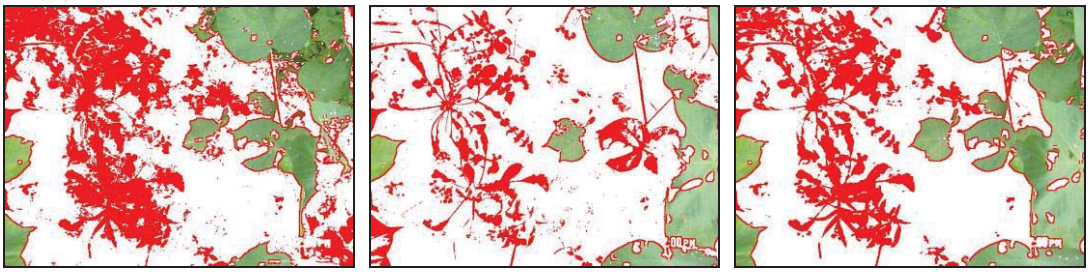

(a) Excess green index (b) G index (c) Optimal index

Fig. 5 Identification of segmentation results with different indexes

weeds in left-bottom of Fig. 5(b) are not identified since they are segmented as background at Step1. Generally, the identification result of Fig. 5(c) is better than that of Fig. 5(a) and Fig. 5(b). In order to quantify the identification results and to analyze the effects of segmentation precision to identification rates, studies are made for the identification precision using the new method proposed in this paper, as listed in Table 1:

Table 1 Parameters

	Cotton pixels in original image	Weed pixels in original image	Soil pixels in original image
Number of Pixels identified as cotton	N1	N4	N7
Number of Pixels identified as weed	N2	N5	N8
Number of Pixels identified as soil	N3	N6	N9
Total number	N1+N2+N3	N4+N5+N6	N7+N8+N9

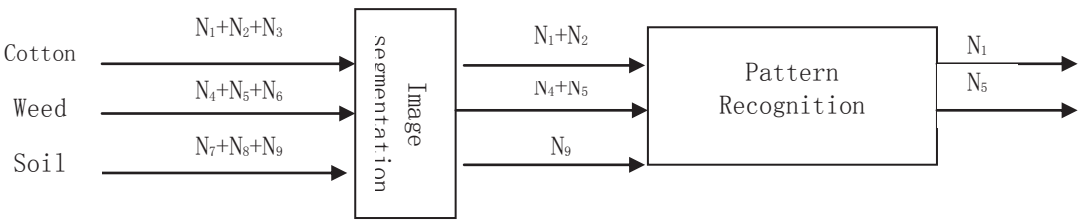

Fig. 6 The difference of pixels' number in segmentation and identifying

Apparently, it can be found out that there are errors both with segmentation and identification. In order to analyze the identification results, the authors define as the followings:

Segmentation precision: the ratio of the number of object pixels in segmented image to the number of object pixels in original image. Therefore, the segmentation precisions of cotton, weed and soil are: (N1+N2)/(N1+N2+N3), (N4+N5)/(N4+N5+N6) and N9/(N7+N8+N9), respectively. And the total segmentation precision and the vegetable (including cotton and weed) segmentation precision are: (N1+N2+N4+N5+N9)/ Σ Ni and (N1+N2+N4+N5)/(N1+N2+N3+N4+N5+N6).

Identification precision: the ratio of the number of object pixels after pattern recognition to the number of object pixels before pattern recognition. Therefore, the identification precisions of cotton and weed are: N1/(N1+N2) and N5/(N4+N5).

Identification rate: the ratio of the number of object pixels after image segmentation and pattern recognition to the number of object pixels of original image. Therefore, the identification rates of cotton and weed are: N1/(N1+N2+N3) and N5/(N4+N5+N6).

The segmentation precision, pattern recognition precision, and identification rate are as shown in Fig. 7, Fig. 8 and Fig. 9. Different segmentation features will result in different precision in the process of weed identification, and here the authors apply F-test to analyze it and obtain significant probability of the three features. The average value of all precisions and the significant probabilities of the three features are listed in Table 2.

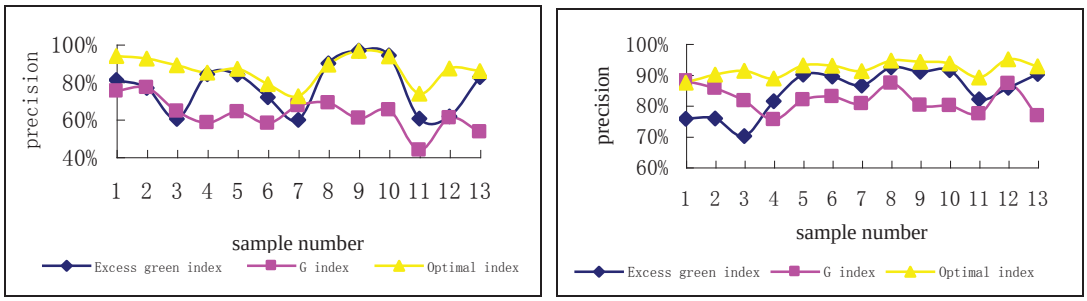

(a) Vegetation segmentation precision (b) Weed segmentation precision

Fig. 7 Precision in segmentation

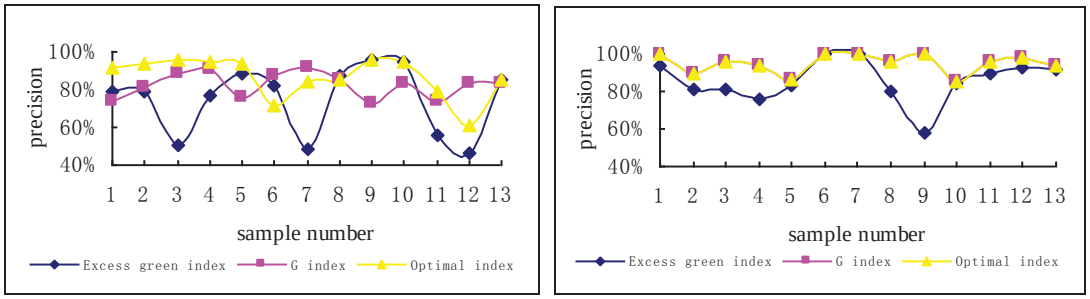

(a) Plant identifying precision (b) Weed identifying precision

Fig. 8 Precision in segmentation

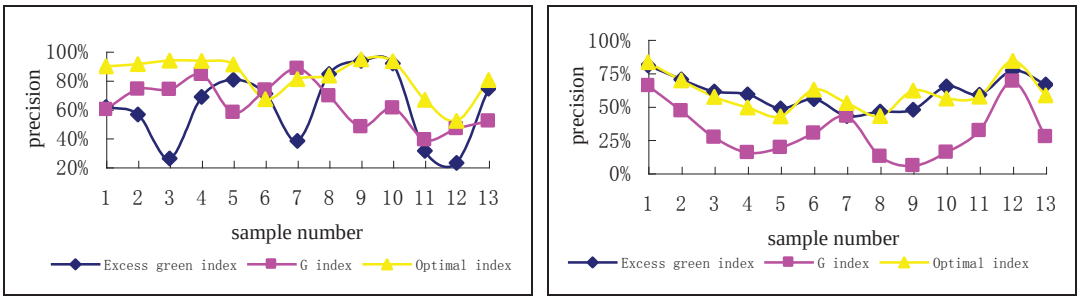

(a) Plant identification probability (b) Weed identification probability

Fig. 9 Identification probability

It can be conclude from Fig. 7 and Fig. 8 that there is no direct relationship between segmentation precision and identification precision; the segmentation precision of optimal index is higher than that of the other two methods, while the identification precision is not always higher than that of the other two methods. Obviously, high segmentation precision cannot guarantee high identification precision. Such as No.4 image, the segmentation precision of G index is markedly lower than that of the other two methods, but its identification precision is much higher than excess green index and is approximate to the optimal index.

The significant probability of cotton and weed segmentation precision listed in Table 2 are both less than 0.01, which indicates that the segmentation precision using the three indexes has markedly difference. While the significant probability of cotton identification precision is more than 0.05, weed significant probability ranges in [0.01,0.05], which indicates that segmentation has no real effect on identification, and the significance probability of differences among weed identification precision is reducing. Apparently, the differences of

Table 2 Precision and probability in segmentation and identifying

	Excess green index	G index	Optimal index	Significant Probability
Cotton identification precision	74.41%	82.37%	86.60%	0.0566
Cotton segmentation precision	79.30%	76.39%	95.13%	0.0016
Cotton identification rate	61.45%	63.41%	82.77%	0.0093
Weed identification precision	85.35%	94.84%	88.62%	0.0244
Weed segmentation precision	70.86%	32.77%	67.33%	0.0000
Weed identification rate	59.84%	31.30%	59.69%	0.0000
Soil segmentation precision	88.38%	95.61%	94.64%	0.0146
Vegetable segmentation precision	77.08%	62.71%	86.40%	0.0000
Segmentation precision	84.69%	75.01%	91.76%	0.0000

indexes in segmentation do not exist in pattern recognition, so the new method in this paper indicates a satisfactory identification precision less affected by segmentation precision.

The identification rate is segmentation precision of weed and cotton multiply by identification precision, as shown in Fig. 9. The differences of identification rate using different indexes are basically the same as segmentation precision differences. The average segmentation precisions of weed using the three indexes are: 70.86%、32.77%、67.33%, while the average identification rates are: 59.84%、31.30%、59.69%. The identification precisions are almost more than 80%, some even with 100%, which makes it possible to neglect the effects of pattern identification errors. Besides, even with a low segmentation precision, the identification precision using the new method still remains high. As shown in Table 2, the average segmentation precision of weed using G index is only 32.77%, however its average identification precision is as high as 94.84%. All in all, to use the ratio of skeleton length to leaf area is much better to distinguish cotton with weed.

It can be seen from Table 2 that the average identification precisions of cotton and weed are both more than 70% using all the three indexes, where the highest is 94.84%. There are two aspects error: one is that erosion operator does not definitely divide the cotton and weed into the areas where the both are mixed together. The other is the error segmenting of cotton to soil. Due to the accumulation of segmentation error and pattern identification errors, the average identification rates of weed and cotton are reduced to less than 70%, except the average identification rate of cotton using the optimal index reaches 82.77%. These caused with low average segmentation precisions of cotton, which are less than 80%, expect that using the optimal index 95.13%; As a result, if taking the better segmentation to identify, the identification rate using the ratio of skeleton area to leaf area can meet basically the practical requirement.

The ratio of the skeleton area to leaf area can better identify weed in field if the processing objects are the whole plant. Because the morphological features would not change with the field natural conditions and the plant itself conditions.

5. Conclusions

A new identification feature is proposed in this paper that the ratio of skeleton area to leaf area is utilized based on the whole plant to better identify weeds in cotton field in the circumstance that the plant leaves are seriously overlapped. This new method has an identification rate less dependent on segmentation precision, and can better deal with the overlapping. It is more practicable.

Acknowledgment

This work was financially supported by the Priority Academic Program Development of Jiangsu Higher Education Institutions(Su financial teacher(2011)no.8)

References

[1] Søgaard H. T. Weed Classification by Active Shape Models, *Biosystems Engineering*, Vol. 91, No. 3, pp. 271-281, 2005.

[2] Neto C. J, Meyer G. E, Jones D. D and Samal A. K. Plant Species Identification Using Elliptic Fourier Leaf Shape Analysis, *Computers and Electronics in Agriculture*, Vol. 50, No. 2, pp. 21-134, 2006.

[3] Chapron M, Boissard P and Assemat L. A Multiresolution Based Method For Recognizing Weeds in Corn Fields, *Pattern Recognition* , Vol. 2, pp. 303-306, 2000.

[4] Lamm R. D, Slaughter D. C and Giles D. K. Precision Weed Control System for Cotton, *Transaction of the ASAE*, Vol. 45, No. 1, pp. 231-238 , 2002.

[5] X. F Li, W. X Zhu, B Ji,et al. Shape Feature Selection and Weed Recognition Based on Image Processing and Ant Colony Optimization, *Transactions of the CSAE*, Vol. 26, No. 10, pp. 178-182, 2010.

[6] Rafael C, Gonzalez and Richard E.Woods. *Digital Image Processing(Third edition)*, Prentice Hall, 2007.

[7] Woebbecke D. M., Meyer G. E., Bargen K. V. and Mortensen D.A. Color Indices for Weed Identification Under Various Soil, Residual, and Lighting Conditions, *Transactions of the ASAE* , Vol. 38, No. 1, pp. 259-269, 1995.

[8] Yang C. C., Prasher S. O., Landry J. A. and Robert K. A Vegetation Localization Algorithm for Precision Farming, *Biosystems Engineering*, Vol. 81, No. 2, pp. 137-146, 2002.

[9] Yang C. C., Prasher S. O., Landry J. A. and Ramaswamy H.S.. Development of an Image Processing System And a Fuzzy Algorithm for Site-Specific Herbicide Applications, *Precision Agriculture* , Vol. 4, No. 1, pp. 5-18, 2003.

[10] Mao H. P., Hu B., Zhang Y.C., et al. Optimization of Color Index and Threshold Segmentation in Weed Recognition, *Transactions of the CSAE*, Vol. 23, No. 9, pp. 154-158, 2007

.

Copyright © 2012 DET Corp., Japan All Rights Reserved
International Journal of Comprehensive Engineering
Part C, 2(2), 196-207, 2013
Doi: 10.14270/IJCE2013.2.2.c196
Regular paper

ISSN 2186-2680
e-ISSN 2186-2656
www.iace-journal.org

Review on Rotating Stall in Pumps

Shouqi Yuan [1,#], Wei Liu [1], Zhongyong Pan [1] and Xiaojun Li [1]

[1] Research Center of Fluid Machinery Engineering and Technology, Jiangsu University, Zhenjiang, 212013, China

[#] Corresponding author: shouqiy@ujs.edu.cn; Tel.: +86-0511-88780007; +086-15252900569

Abstract: Rotating stall, which is perhaps more comprehensive to be called propagating stall or revolving stall, in mixed flow pumps and low specific speed centrifugal pumps are reviewed. Stall displays various patterns of rotating stall, alternate blade stall, or asymmetric stall, and in which rotating stall can appear in centrifugal impellers, mixed impellers, radial diffuser passages or axial diffuser passages and propagates at a fraction of the impeller rotational speed to cause flow instabilities and pressure hysteresis. Pressure transducers flush mounted in the diffuser passages can be used to determine the number of rotating stall cells and propagation speed of rotating stall according to the pressure signal peaks and cross spectrum. Both DPIV and time resolved PIV can be used to visualize the flow patterns of rotating stall. Alternate jet flow and reverse flow appear in the passage of a diffuser or an impeller when rotating stall occurs. The Reynolds averaged Navier-Stokes equations accompanied with the standard k-ε turbulence model or SST k-ω turbulence model can be used to simulate the behavior of rotating stall. No LES was reported to describe the rotating stall though it was reviewed that LES can simulate a steady nonrotating stall phenomenon and predict the positive slope curve of a mixed flow pump very well. A kind of method of J-groove was also introduced to suppress the instabilities that the rotating stall related. In spite of considerable efforts devoted to the study of rotating stall in pumps, the mechanics of this phenomenon are not yet well understood. The propagation mechanism and onset of rotating stall is more complicated than the classical explanation. Not only effected by the inlet flow, but also influenced by the outlet flow as well as the pressure gradient in the flow passage. It is mentioned that the pressure phase determine the stall propagation, a further problem is that what determine the pressure phase. In addition, the life of rotating stall through a single passage can not be determined.

Keywords: Rotating Stall, Pump, Propagation Speed, Instability.

Received: May 12,2012 / Accepted: Feb. 20,2013 / Published: Jul. 5,2013

1. Introduction

The trend toward higher speed, higher power pump has inevitably increased the potential for fluid-structure interaction (FSI) problems, and the severity of those problems. The occurrence of these problems both in boiler feed pumps and process pumps has been recognized to be significant contribution to downtime in conventional power and hydrocarbon processing plants. The FSI problems incorporate a variety of pump instabilities that have yet to be properly identified. The pump instabilities seem to be crudely divided into the following categories as shown in Table 1[1, 2].

The complete analysis of the FSI problems must be combined with an unsteady fluid flow analysis in order to accurately predict the interface contents. Furthermore, the advanced diagnostics for the pump performance and failure needs to get more details about the flow fields and their responses [3]. We have made some efforts in these issues[2-6], and in this paper we review the rotating stall in pumps.

2. Classical Comments

Rotating stall is a phenomenon which may occur in a cascade of blades when these are required to operate at a high angle of incidence close to that at which the blades will stall. In a pump this usually implies that the flow rate has been reduced to a point close to or below the maximum in the head characteristic. The cascade in Fig. 1 will represent a set of blades (a rotor or a stator) operating at a high angle of incidence. Then, if blade B were stalled, this generates a separated wake and therefore increased blockage to the flow in the passage between blades B and A. The static pressure inside the stall region is smaller than in the surrounding flow; vortices can therefore appear with the same rotating direction as the impeller. In the outlet of the passage a second vortex can be formed with an inverse rotational direction (exchange vortex). These vortices can grow until the complete passage is blocked. Then, the medium has to pass through the following passage. This, in turn, would tend to deflect the flow away from this blockage in the manner indicated in the figure. The result would be an increase in the angle of incidence on blade A and a decrease in the angle of incidence on blade C as shown in Fig. 1. Thus, blade A would tend to stall while any stall on blade C would tend to diminish. Consequently, the stall "cell" would tend to propagate anticlockwise in the figure or in a direction away from the oncoming flow. Of course, the stall cell could consist of a larger number of blades with more than one exhibiting increased separation or stall. The stall cell will rotate around the axis and hence the name "rotating stall". Moreover, the speed of propagation will clearly be some fraction of the circumferential component of the relative velocity, either $v\theta 1$ in the case of a stator or $w\theta 1$ in the case of a rotor. In addition, in the case of a rotor, the stall rotates in the same direction as the rotor but with 50%-70% (some reported is of 50%-90%) of the rotor angular velocity, and in the case of a stator, the fraction is between 10%-25% [1, 7, 8]. Consequently, the phenomenon possesses one vortex with the same rotating direction as the impeller and confined by a separated flow upstream and a reattached flow downstream, a propagating velocity against the shaft rotational direction, and an accompanied vortex appeared downstream which rotates also against the shaft rotational direction. This is the case in rotating impeller, while that in stationary component is somewhat different. Therefore, it should be noted that the term of "propagating stall" or "revolving stall" maybe more comprehensive to define this phenomenon than "rotating stall" as stationary stall also rotates around axis of itself yet it does not propagate around the shaft axis.

Table 1 Categories of Pump Instabilities

Category	Type
Flow instabilities	Rotor-stator interaction, rotating stall or rotating cavitation, partial cavitation or super cavitation, vortex shedding, inlet distortion flow, inlet backflow, tip leakage flow
Structural instabilities	Blade flutter, axial balance resonance
Operation instabilities	Start up or close up conditions
Hydraulic system instabilities	Surge, cavitation surge, choked surge
System instabilities	System vibration or noise induced by resonance with cavitation noise or blade passing frequencies
Radial and rotordynamic forces	
Accelerating reference frame	POGO instabilities, pumping systems aboard a ship, or the fuel and hydraulic systems on an aircraft

Though the coherent explanation of propagating stall in compressors was first provided by Emmons et al. in 1955[9], the mechanism of this phenomenon is not yet understood up to now. Rotating stall is most frequently observed and most widely studied in compressors with large numbers of blades. An important issue of which is to predict both the onset and consequences of rotating stall. A useful approximate criterion is that rotating stall in the rotor occurs when one approaches a maximum in the total head rise as the flow coefficient decreases. This is, however, no more than a crude approximation and Greitzer quotes a number of cases in which rotating stall occurs while the slope of the performance curve is still negative [10]. A more sophisticated criterion that is widely used is due to Leiblein, and involves the diffusion factor, *Df*, defined as

$$Df = 1 - \frac{w_2}{w_1} + \frac{v_{\theta 2} - v_{\theta 1}}{2sw_1} \tag{1}$$

where *s* is solidity. Experience indicates that rotating stall may begin when *Df* is increased to a value of about 0.6. Rotating stall has not, however, been reported in axial pumps with a small number of blades perhaps because *Df* will not approach 0.6 for typical axial pumps or inducers with a small number of blades.

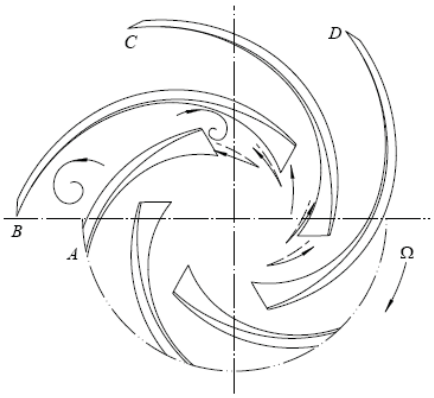

Fig. 1 Rotating stall phenomenon in a centrifugal impeller

As to centrifugal pumps, there have been a number of studies in which rotating stall has been observed either in the impeller or in the diffuser/volute. The earlier study focuses on the rotating and the propagating speed, and their geometry dependent.

Hergt and Benner observed rotating stall in a vaned diffuser and conclude that it only occurs with some particular diffuser geometries [11]. Lenneman and Howard examined the blade passage flow patterns associated with rotating stall and present data on the ratio, Ω_{RS}/Ω, of the propagation velocity of the stall cell to the impeller speed, Ω. They observed ratios ranging from 0.54 to 0.68 with, typically, lower values of the ratio at lower impeller speeds and at higher flow coefficients [12]. Even in the absence of blades, it is possible for a diffuser or volute to exhibit a propagating rotating "stall". Jansen first described this flow instability and indicated that the flow pattern propagates with a speed in the range of 5%−25% of the impeller speed [13].

Yoshida et al. made observations on a 7-bladed centrifugal impeller operating with a variety of diffusers with and without vanes. Rotating stall with a single cell was observed to occur in the impeller below a certain critical flow coefficient which depended on the diffuser geometry. In the absence of a diffuser, the cell speed was about 80%−90% of the impeller rotating speed; with diffuser vanes, this cell speed was reduced to the range 50%−80%; with vaneless diffuser, a four-cell rotating stall was observed over a large range of flow coefficients and its velocity was measured as about 20% of the impeller speed. When impeller rotating stall was present, they also detected the presence of some propagating disturbances with 2, 3 and 4 cells rather than one. These are probably due to nonlinearities and an interaction with blade passage excitation. Rotating stall was also observed to occur in the vaned diffuser with a speed less than 10% of the impeller speed. It was most evident when the clearance between the impeller and diffuser vanes was large. As this clearance was decreased, the diffuser rotating stall tended to disappear [14].

Thanks to the advanced CFD technologies and the precision test measurements, distinct progresses on rotating stall in pumps were made during the last decade and were listed in the following sections in detail.

3. Experimental Investigations

Ogata and Ichiro report on measurements of pressure fluctuations and velocity fields, using hot wire measurements, in a vane diffuser of a centrifugal compressor [15]. They conclude that the presence of a volute casing causes circumferentially nonuniform conditions at the outlet from the diffuser and that this nonuniformity is a large factor in the inception of rotating stall. Their velocity measurements indicate the existence of reverse flow in the vane passages with the lowest pressure field, but being point measurements, they cannot provide details on the flow structure and onset mechanisms. They also suggest that the propagation mechanism of a stall cell from one vane passage to another is more complex than the conventional explanation. Additional relevant reference material on stall and instabilities, including empirical correlations for the behavior of impellers and diffuser vanes can be found in 1990s'. In spite of these efforts, there is still very little experimental data on the detailed flow structures within a stalled centrifugal turbomachine, the mechanism causing the onset of stall as well as on the effects of blade orientation and flow rate on the flow structure within a stalled pump.

Recently, PIV technology is widely used to visualize the unsteady flow fields in pumps. In addition, piezoelectric pressure transducers are flush mounted to record the pressure amplitude and phase. Some new features were discovered.

3.1 Piezoelectric pressure transducer application and results

Piezoelectric pressure transducers (PCB 105B02) were first flush mounted on the static component of a diffuser centrifugal pump of n_s=95 by M Sinha et al. to investigate rotating stall within the vaned diffuser [16]. The positions of the transducers are shown in Fig. 2. The performance curve of the pump was first presented and the authors believe that the pump is close to the onset condition of rotating stall where there is a change in the slope of the performance curve at flow coefficients below 0.06.

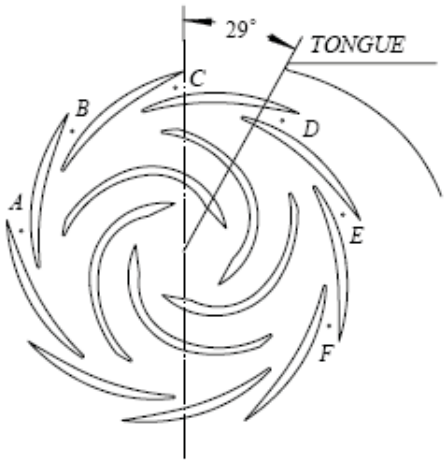

Fig. 2 Locations of piezoelectric pressure transducers

The power spectrum of the signals acquisitioned by the transducers were analyzed under design and a stalled condition, and those under a stalled condition yields an additional peak at 0.93Hz (6.2% of the impeller speed) in passage A, B, C, D and E, but not in F. Unlike passages A-E, it has no distinct spectral peak at frequencies below 15 Hz in passage F.

Cross-spectrum analysis between each pair of transducer signals was performed. The peaks are at frequencies that are common to the two signals and the phase is indicative of the time lag/lead between them. The authors obtain data at 0.93 Hz for passages A-E, since there is no peak in the spectra involving passage F. The phase angles by which the pressure signal of sensor A leads the signals in the other passages are tabulated in Table 2. Clearly, the time delay (hysteresis) varies as the phenomenon moves from one passage to another. The propagation speed initially increases as the tongue is approached. The time lag between sensor A and B is 0.145s, whereas the lag between B and C is 0.06s. Between C and D the lag increases only slightly to 0.076s, but then it increases substantially to 0.436s between D and E and disappears completely in F. The decaying propagation speed suggests the influence of the non-uniform flow conditions (circumferential pressure gradients) that exist, according to Ogata and Ichiro[15], in the volute casing outside the diffuser, or in the gap between the impeller and the diffuser, as the present velocity measurements indicate. Since the propagation speed is not uniform, the number of stalled cells that exist at a given instant of time cannot be estimated.

Table 2 Phase and Time Lead at 0.93Hz

Transducer	Angular separation/°	Phase lead/°	Time lead/s
A&B	40	48.49	0.145
A&C	80	68.59	0.205
A&D	120	94.06	0.281
A&E	160	258.0	0.717
A&F	200	not stalled	not stalled

Recently, Stefan Berten et al. performed pressure fluctuation measurements synchronously in the impeller and in the diffuser of a high-energy centrifugal pump of n_s=78 at different flow rates and various rotational speeds. During these measurements stationary and rotating stall in the diffuser had been observed[17]. 48 piezo-resistive miniature pressure sensors were flush mounted in the impeller eye, the impeller passages, the hub and throud side wall at the impeller outlet, the impeller blade close to the trailing edge, the diffuser passage throat and outlet sections. Fig. 3 shows a pressure transducer and an impeller blade trailing edge implemented

with a pressure transducer.

Fig. 3 Pressure transducer implemented in impeller blade[17]

The pump has a 7 blades impeller and a 12 vanes diffuser. At the best efficiency flow rate (q^*=1), the phase-averaged, non dimensional fluctuating pressure measured close to the impeller blade trailing edge in the pressure surface is a periodic pattern with 12 maxima and 12 minima. After reducing the flow rate to 90% of the best efficiency flow rate, a singular high pressure peak is superposed to the periodic pattern due to the diffuser vane passage. The authors attribute this local increase of the pressure to a flow separation (stall) in one of the diffuser passages. This separation yields an increased diffuser throat pressure due to the reduced flow velocity in the separated diffuser passage. The pressure peak is followed by a pressure minimum, which is caused by the local increase of the flow velocity for the diffuser vane suction surface following the separated diffuser passage in the rotational direction of the impeller. At the best efficiency flow rate, the non disturbed pressure distribution with the 12 minima and 12 maxima can be identified. At q^*=0.9, the stationary separation of one diffuser passage is visible as a high pressure peak (stationary stall). At a flow rate reduced to q^*=0.8, this high pressure peak starts to propagate with a propagation speed of less than 0.7% of the impeller rotational speed (rotating stall). The peak is steadily propagating in the same direction as the impeller rotation direction. At further reduced relative flow rates, the number of pressure peaks, which are regarded as the number of stall cell and are propagating in the impeller direction, increases until no real organization of the pressure peaks can be identified at flow rates lower than 50% of the best efficiency flow rate. FFT analysis was further performed to affirm that the number of the pressure peaks is that of the stall cell.

On the other hand, the pressure fluctuations as well as the frequency contents in the vaned diffuser at a position close to the rotor-stator interface at q^*=0.8 were displayed. When the rotating stall is present, pressure fluctuations at a very low frequency get visible, but the resolution of the spectra is not sufficient to use this information for further analysis. Neither the number of rotating stall cells nor their rotation direction can be easily detected by the analysis of only one pressure transducer signal in the stationary domain. The identification of the number of stalled diffuser passages and their propagation direction can be achieved by the analysis of the pressure transducer array in the diffuser throat by means of cross-correlation based analysis or 2D-FFT. The authors depicted that this is foreseen for their future analysis. It is interesting and important to note here that the contents discussed above as shown in Fig. 2 and Table 2 is just their expectation. At last, the influence of the rotational speed of the pump on the pressure fluctuations has been investigated. When the rotating speed changes from 1500 r/min to 5000r/min, it is found that the number of stalled diffuser passages has increased from one to two and its circumferential position has changed. These work at variable rotational speeds unveiled a speed dependant of the separation development, which can not be explained yet in a systematic order and which will be subject of further research. Before leaving the issue of this section, it is should to note that the authors did not present the performance curve of the pump, consequently whether the positive slope curve dependent or independent is not sure.

Incidentally, piezoelectric pressure transducer is also an efficient instrument used to investigate other flow instabilities, for example, cavitation, in pumps and turbines [18, 19].

3.2 Flow field features of rotating stall captured by PIV

In the past, a variety of measurement techniques, particularly one-point techniques such as pressure probes, hot-wire anemometry, and laser Doppler velocimetry (LDV) have been applied to turbomachines in the strive for accurate quantitative flow descriptions. These mean methods have provided much fundamental knowledge of flow phenomena occurring in centrifugal impellers. However, the quest for more flexible pumps that maintain high efficiencies at a broader range of operating conditions raises the need for a more detailed knowledge of the local and instantaneous features of the impeller flow. For this purpose, the particle image velocimetry (PIV) technique is a powerful alternative or supplement to LDV which offers both more

information on the instantaneous spatial flow structures and, at the same time, considerably reduced acquisition times.

Before proceeding to a discussion of the rotating stall visualized by PIV, it may be valuable to illustrate that Johnson et al. reported stationary stall with respect to the rotating frame of reference in a volute centrifugal pump impeller of n_s=75 with the data from LDV probe [20], as it is mentioned that point measurements can not provide details on the flow structure and onset mechanism. The pressure distribution contours displayed by the authors are similar to that of Yuan et al. under both design and off design conditions of a volute centrifugal pump [4].

M Sinha et al. further investigated the flow structures of the geometry shown in Fig. 2 by PIV which was trigged during maximum, minimum and zero-crossing (growth or decay) phases of the low-pass-filtered signal of the transducer located at *C*, as these signals are indicated to be associated with the stall by the authors[16]. Figure 4a-c shows the sample instantaneous vector sketch at different phases of the stall, when the low-pass-filtered transducer signal at *C* is minimum, zero-crossing and maximum, respectively. At minimum pressure, there is a reverse flow in vane passage *C*. The magnitude of reverse velocity is only about 10 percent of the impeller tip speed. There is also clear evidence of flow separation at the trailing edge of the vane. During zero crossing, as the pressure in *C* is rising, the flow in passage *C* is in the process of recovering from the reverse flow, whereas there is still backward flow in passage *D*. Interestingly, in Fig. 4b there is a negative radial velocity on the pressure side of the impeller blade, i.e., there is a backward flow into the impeller. At a pressure-maximum phase, there is a strong outward flow through passages *C* and *D*. The velocity at *D* is higher, presumably due to the lower mean pressure at the beginning of the volute when the pump operates below design conditions. The outflow from passage *C* separates from the convex side of the vane and is aimed directly toward the exit. In all cases there is a strong leakage flow in the gap between the impeller and the diffuser from the exit side to the beginning of the volute. The leakage velocity exceeds 50 percent of the impeller tip speed. The secondary flow downstream of the diffuser is complex but is significantly slower. Subsequently, the effect of both blade orientation and flow rate is analyzed. The velocity distribution in the gap between the impeller and diffuser depends, but not to a great extent, on the orientation of the impeller. The velocity is typically higher, exceeding 50 percent of the tip speed, on the pressure side of the impeller blade, and decreases as much as 40–45 percent in other regions. It is shown that the phase-averaged flow structure under stalled conditions shows some, but not substantial, dependence on the impeller orientation. Most of the effects are confined to the immediate vicinity of the blade and there is limited impact on the flow within the diffuser during maximum pressure phase. A probable cause for this limited effect is the high speed circumferential leakage flow that separates between the impeller and the diffuser. The authors illustrated the transition, with decreasing flow rate, from a flow that is not stalled to conditions of massive stall that covers more than one blade passage simultaneously at last and mentioned that the separation of leakage flow from the diffuser vane causes the onset of the stall, and with decreasing flow-rate the magnitudes of leakage and reverse flow within a stalled diffuser passage increase, and the stall-cell size extends from one to two diffuser passages. However, the authors particularly note that their efforts is limited as all the velocity measurements are performed in the same central plane while the flow is three dimensional.

The rotating stall mentioned above mainly appears in diffuser passage while Krause et al. and N Pedersen et al. focus their attention on those in centrifugal impellers [8, 21]. Measurements of the instantaneous flow inside the rotating impeller passages themselves are very scarce. Though N Pedersen et al. did not find rotating stall in their PIV investigations of an n_s=96 impeller, yet we address their test equipment here because it is very important for us to illustrate our opinions later. Fig. 5 is their compact closed-loop test rig specially designed. A flow straighten device was used as inlet pipe to the impeller, and the impeller discharge the flow directly into the outer annulus of the cylindrical tank. So it can be presumably that both the inlet and the outlet of the

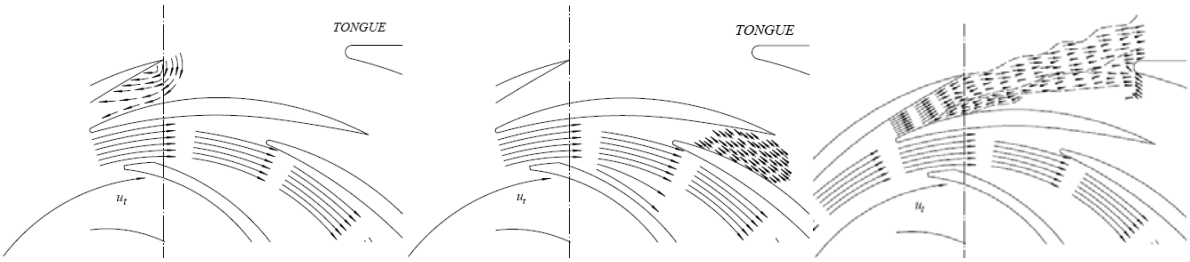

(a) at minimum pressure phase (b) at zero-crossing pressure phase (c) at maxium pressure phase

Fig. 4 Sample instantaneous velocity sketch of low-pass-filtered pressure signal at passages shown in Fig. 2

impeller are of uniform pressure distributions. Therefore, it is not surprised that the authors discovered a stall phenomenon was steady, non-rotating (non-propagating) and not initiated via the interaction with stationary components.

Krause et al. get a conclusive evidence for the rotating stall in a centrifugal pump impeller as they used time-resolved PIV which has the following two advantages[8], one is that this technology is able to investigate the complete flow field of the stall cell while most of the previous measurements are intrusive techniques,the other one is that it can be performed with a high temporal and spatial resolution while the previous measurements applied phase averaging which means the stochastic character of the phenomenon and all significant characteristics that are not exactly periodic are lost. The impeller investigated is followed by a circular diffuser with 12 drain pipes that a rotationally symmetric pressure distribution can be obtained. With the help of time-resolved PIV, the authors observed a standing stall cell in one passage of the impeller at Q/Q_0=0.5. This result shows that before rotating stall starts, stall cells can exist in particular passages of the impeller without propagating (stationary stall). At a flow rate of Q/Q_0=0.41 the stall cells could not only be observed in one, but in several passages of the impeller, and the stall cell moves through the impeller with an angular velocity different from that of the impeller. The stall cell appears to be rotating in the inverse sense of the impeller movement. During 102 revolutions of the impeller, the existence of stall cells in the different blade passages recorded shows that the stall cells stay in two specific passages during several revolutions of the impeller. The authors concluded that, in spite of the computer-aided manufacturing of the parts of the pump, irregularities must exist in the geometry of the pump. These irregularities are very small, but apparently sufficient to induce small unsymmetrical flow distributions in the passages, which are at the origin of the stall cell. From a flow rate of Q/Q_0=0.35 downwards, a continuous rotation of the stall cells was observable. In addition, the authors gave two equations to determine the frequency of rotating stall and the number of revolutions of the impeller for one revolution of the stall cell in the impeller, respectively. At last the authors admitted that it was impossible to get the “life” of a stall cell through a single passage over the complete measurement series with the time resolved PIV system they used.

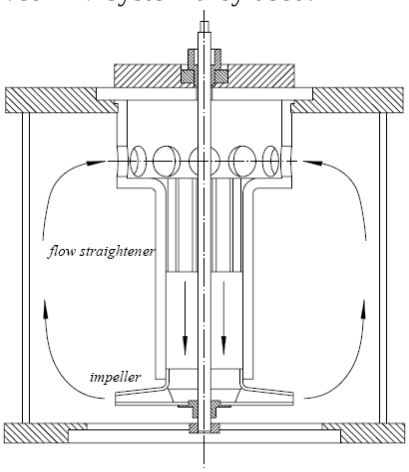

Fig. 5 Closed-loop test rig specially designed[21]

We are very fortunate that the three cases we cited above can identically demonstrate the origin that causes the stall propagating, and which will be further demonstrated by the following two sections. It is just the non-uniform pressure distributions which is appeared in the impeller/diffuser outlet or inlet cause the stall to propagate, the conclusion coincide with that of Ogata and Ichiro [15]. As a conclusion, N Pederson et al. uniformed both the inflow and discharge flow with specially designed device as shown in Fig. 5, therefore no rotating stall elsewhere was discovered [21]. M Sinha used a converging nozzle and a flow straightener (honeycombs and screen) at the entrance of the pump to smooth the inflow, therefore no rotating stall was found in the impeller while that in the diffuser due to pressure non-uniformity in volute and leakage flow was studied [16]. Krause et al symmetry designed the discharge flow of the impeller, and only the rotating stall in impeller

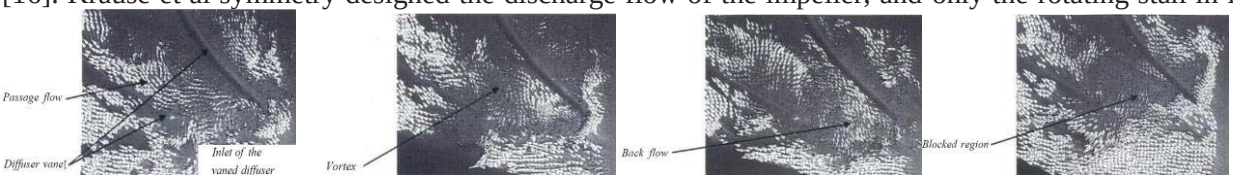

Fig. 6 Instantaneous velocity vectors by DPIV at low flow rate[25]

exists [8]. Yet the author attribute the onset of the rotating stall to manufactured irregularities, we do not agree with them as we have found non-uniformity whirl strip occurred in the inlet pipe in our earlier studies [22].

Rotating stall can also appear in mixed flow pumps [23-25]. In order to investigate the instabilities of positive slope of head-flow performance curves of two mixed flow pumps with vaned diffuser of n_s=162 and n_s=332, M Miyabe et al. visualized the unsteady internal flow in diffuser with Dynamic PIV[24, 25]. The authors clarified that the diffuser rotating stall causes the positive slope of a head-flow characteristic and the backflow (i.e. a stall cell or a vortex) at hub side of the vaned diffuser plays an important role on the onset of the diffuser rotating stall, and they presumed the inception of the characteristic instability as follows. As shown in Fig. 6, at the partial flow rate, low energy fluids are accumulated in the corner between the hub surface and the convex surface of the diffuser vane. As the flow rate further decreased, the low energy fluids region at the corner axis-asymmetrically expands along hub and became unstable due to the adverse pressure gradient. Then, strong backflow occurs and impinges against passage flow from the impeller at the inlet of the vaned diffuser. In addition, the backflow blocks the passage flow from impeller and the inlet flow angle at the leading edge of the adjacent diffuser vane is reduced. Therefore, flow separation occurs near the inlet of convex surface of the vaned diffuser, and a strong vortex is generated there. After that, the vortex develops and becomes a stall cell. Actually, the authors engaged in the suppression of the back flow mentioned above in these studies and they did not pay attention to the hysteresis feature of rotating stall. They attributed the stall propagating to the axis-asymmetrical flow yet not explain why the adverse pressure gradient can make the flow axis-asymmetrically expand.

In addition, pressure characteristic by pressure transducer flush mounted in the diffuser is also investigated, and the typical pressure signals of stall (not rotating stall) are similar to that of section 3.1 and Yuan et al [4] discussed above.

4. Application of Numerical Simulations

The application of CFD code is becoming popular for the investigation of the detailed 3-D flow and unsteady phenomena in pumps. Takeshi Sano et al. carried out numerical analyses of the flow instabilities in a centrifugal pump vaned diffuser by using commercial software focusing on the effects of diffuser pressure performance and the impeller/diffuser clearance to compare with their former visualizing of the flow field under stalled conditions [26]. During their efforts, the transport equations are discretized using a finite-volume method. The code solves the Reynolds averaged Navier-Stokes equations in primitive variable form. The effects of turbulence were modeled using the standard k-ε turbulence model. To make the simulation timely economical, a wall function is used to resolve the wall flows. The authors first simulated a vaned diffuser without impeller and observed asymmetric stall, alternate blade stall and rotating stall. The authors regard the symmetric stall as a kind of rotating stall with zero propagation speed (stationary stall). Alternate blade stall was also observed and it takes the nature that the inlet pressure varies high and low in alternate passages (Its blade number should be surely even). Cross spectrum was also used to calculate the hysteresis. The authors further investigated the diffuser with some centrifugal impellers and find both rotating stall and asymmetric stall while the latter is less than that in the diffuser with no impeller. The flow patterns of rotating stall is shown in Fig. 7, it is interesting that the structure matches satisfied with that in Fig. 4. According to the authors, as the clearance between the impeller and the diffuser increases, the diffuser rotating stall occurs more easily caused by the decoupling of impeller/diffuser flow. In case of smaller clearance, the impeller/diffuser coupled rotating stall was observed at low flow rate. In case of wider clearance with smaller interaction between the impeller and diffuser, the impeller rotating stall occurs independently from the diffuser rotating stall at low flow rate. M Miyabe also used commercial software to calculate rotating stall behavior. Because it is said that SST k-ω turbulence model has a merit for good behavior in adverse static pressure gradient and separated flow, they adopted this model and

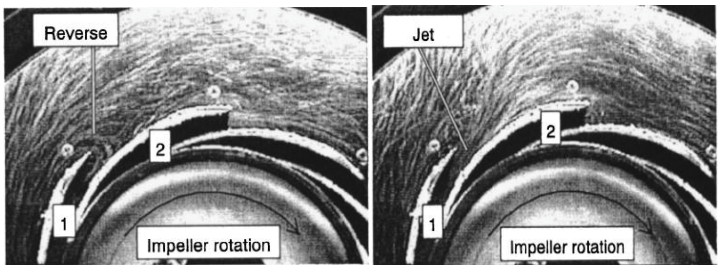

Fig. 7 Flow structures under rotating stall[26]

obtained good results that well agree with the experimental result of Fig. 6[25]. Because they focus on the positive slope of the head-flow characteristic, no more details in flow structures other than Fig. 6 are discussed.

Large eddy simulation (LES) is a promising alternative or supplement to standard Reynolds averaged Navier-Stokes (RANS) turbulence modeling. R K Byskov et al. used LES to simulate the flow field in a shrouded six-bladed centrifugal pump impeller as shown in Fig. 5, and as expected only a steady nonrotating stall phenomenon is observed in the entrance of one passage and a relative eddy, which is somewhat similar to the exchange vortex shown in Fig.1 and has high positive values of the relative velocity along the blade suction side and flow reversal along the dominant part of the blade pressure side, develops in the remaining part of the passage[27]. The authors also found that the two RANS models do not reproduce the stall phenomenon observed at quarterload and are incapable of detecting the differences between the two passages. Y Yamade et al. also used LES calculated the internal flow of a mixed flow pump with different grid resolutions [28]. They focus on the performance curve instability to understand the mechanism of the instability. The highlight of their study is that they pay their attention mainly on the impeller while the former investigations almost attribute the instabilities to the flow separation in diffuser. As shown in Fig. 8, the authors clarified that the instabilities of the performance curve due to the drastic changes of flow structures as follows: When flow rate decrease from Q^*>70% to Q^*<60%, the spanwise pressure gradient decreases at the hub and increases at the tip of the impeller outlet. As a result, local high-pressure regions appear at the suctions-tip side of the impeller blades trailing edge. This local high pressure leads to flow separations. Parts of separated flows return to the neighboring blades. This direction change of the streamlines implies the separation of the flows at the suction-tip side of the impeller blade. The separation is due to an adverse pressure gradient on tip-suction side. As a result, effective diameter becomes smaller due to the returned flow which leads to total pressure drop. Velocity profiles change at both the inlet and outlet of the impeller. Reverse flows take place at the inlet-tip and outlet-hub. Flow pattern changes from the axial-type to centrifugal-type, since inflow to the impeller shift to the hub side and outflow shift to the tip side. Similar with reference [27], the efforts herein pay no attention on the detail of rotating stall though the instabilities are related with the stall behavior. In other words, the unsteady phenomenon needs to be further studied.

H Wang et al. mentioned that there exist the following difficulties in employing the unsteady RANS solver: (1) mesh generation problem in the gap between the impeller and the diffuser, (2) turbulence model problem in the complicated unsteady flow, and (3) convergence problem in grid and iteration number per time step [29]. Therefore, they extended vortex methods to calculate the rotating stall in a diffuser pump as the method can be easily applied to flow around complex geometry because of its grid free nature. Interestingly, the authors find two separated range where stall would occur. As the emphasis of the investigation is the overall instabilities under of design conditions, more details on rotating stall did not be presented. However, a heuristic idea may be useful for us that the reason of which the stability exists between the two unstable areas.

5. Rotating Stall Control and Suppression

Similar with that the investigations of rotating stall earlier focus on compressor, the control and suppression of rotating stall are also first presented in the field of compressor[30]. Other than their efforts on compressors, the investigators also extend their J-grooves to suppress the instabilities of a mixed flow pump [23]. The J-grooves of proper dimension mounted on the diffuser wall/walls had been able to suppress rotating stall perfectly in both a vaneless diffuser and a vane diffuser for the entire flow range. Even though the grooves were very shallow, the increase in the flow angle was significant. A strong groove flow on the upper wall of the diffuser flows against the main flow. Experimental findings and theoretical considerations revealed that the remarkable efforts of J-groove are caused by the following two mechanisms: one is a remarkable decrease in tangential velocity at the diffuser inlet owing to mixing between the main flow and the groove reverse flow, and

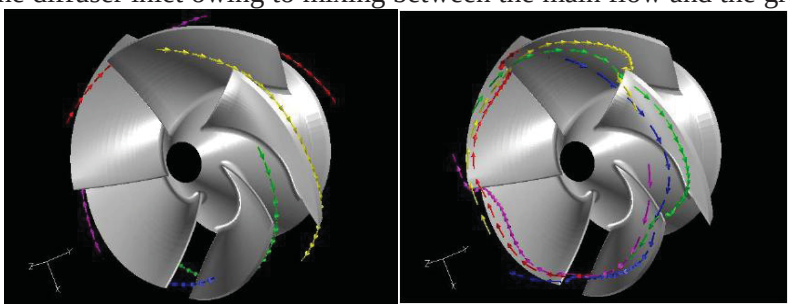

(a) Q^*=70% **(b) Q^*=55%**

Fig. 8 Streamlines on the surface of impeller blades [28]

the other is a remarkable increase in radial velocity due to the groove reverse flow. Both effects have the same contribution to increase the flow angle.

After the behavior of rotating stall in a diffuser mixed flow pump investigated, M Miyabe et al. enlarge the inlet of diameter diffuser hub to suppress the rotating stall [23]. This method is also a mean to increase the flow angle. But in this way, whether the rotating stall moves to lower flow rate or not is not mentioned in the issue. Combined with the idea mentioned in the finally of section 4, this suspension would be answered by further study.

6. Conclusions and Discussions

(1) Apart from CFD and PIV technologies, pressure transducers flush mounted are new instruments which can be used to efficiently detect and explore the unsteady contents of flow fields, especially those in diffuser can determine the number of stall with uniform propagation speed. Time-resolved PIV offers the possibility of deepening previous knowledge and clarifying the structure of the stall cell. Cross spectrum can be used to calculate the hysteresis of the rotating stall.

(2) At low flow rate, stall will appear in pumps and takes the types of asymmetric stall (rotating stall with zero propagation speed or stationary stall) or rotating stall. Though alternate blade stall was reported both in diffuser and impeller passages, actually it seldom appear in turbomachinery as it can not be both completely axis-symmetrical in practice and even blade number. No rotating stall was reported in high specific speed centrifugal volute pumps, the nature of the impeller passage and the volute may gave us some new ideas to suppress the rotating stall of pumps in design stage.

(3) The propagation mechanism and onset of rotating stall is more complicated than the classical explanation. Not only effected by the inlet flow, but also influenced by the outlet flow as well as the pressure gradient in the flow passage. It is mentioned that the pressure phase determine the stall propagation, a further problem is that what determine the pressure phase.

(4) Due to asymmetry of volutes, rotating stall in diffuser will not finish one complete circle of propagation. In this case, the propagation process is unsteady and it is difficult to calculate its speed.

(5) Alternate jet flow and reverse flow appear in the passage of a diffuser or an impeller when rotating stall occurs. There exist lower identical frequencies dependent on the flow rate and rotational speed. There is also a discrepancy in the performance curve and as a result it is believed that the pump is closed to the onset condition of rotating stall. No rotating stall was reported at the negative slope area while such cases were extensively found in compressor.

Acknowledgment

The study was supported by National Natural Science Foundation for Distinguished Young Scholars of China, No.50825902 and the Priority Academic Program Development of Jiangsu Higher Education Institutions (PAPD). These supports are greatly acknowledged.

References

[1] Ref Brennen C E. *Hydrodynamics of Pumps*, Oxford University Press, 1994.

[2] Z.Y Pan, J. J Li, S. Li and S.Q Yuan. Study on Radial Forces of Centrifugal Pumps with Various Collectors, *Proceedings of ASME-JSME-KSME Joint Fluids Engineering Conference*, pp. 24-29, 2011.7, Hamamatsu, Japan.

[3] Yamamoto T, Jinyama H and Z. Y Pan. Development of Pump Performance Monitor (Part I), *Symposium on Evaluation and Diagnosis (Section 5)*, pp. 105-112, 2005.11. 27, Japan.

[4] S. Q Yuan, Y. Y Ni, Z. Y Pan and J. P Yuan. Unsteady Turbulent Simulation and Pressure Fluctuation Analysis for Centrifugal Pumps, *Chinese Journal of Mechanical Engineering*, Vol. 22, No. 1, pp. 64-69, 2009.

[5] Z.Y Pan, Y. Y Ni, Jinyama H and S. Q Yuan. Structures and Pressure Fluctuations in a Centrifugal Pump at Design and Off-Design Conditions, *ASME Fluids Engineering Division Summer Meeting (FEDSM2009)*, pp. 2-5, 2009, Vail, CO, USA.

[6] Z. Y Pan, Y. Y Ni, S. Q Yuan, H. Li. Experiment and Mechanism of Centrifugal Pumps Rotation Speed Measurement Based on Rotor-stator Interaction, *Transactions of the Chinese Society for Agricultural Machinery*, Vol. 41, No. 3, pp . 81-85, 2010.

[7] Gülich J F. *Centrifugal Pumps*, Springer Berlin Heidelberg , New York, 2007.

[8] Krause N, Zahringer K, Pap E. Time-resolved Particle Imaging Velocimetry for the Investigation of Rotating Stall in a Radial Pump, *Experiments in Fluids*, Vol. 39, pp. 192-201 , 2005.

[9] Emmons H W, Pearson C E and Grant H P. Compressor Surge and Stall Propagation, *Transactions of ASME*, Vol. 79, pp. 455-469, 1955.

[10] Greitzer E M. The Stability of Pumping Systems – the 1980 Freeman Scholar Lecture, *ASME Journal of Fluids Engineering*, Vol. 103, pp. 193-242, 1981.

[11] Hergt P and Benner R. Visuelle Untersuchung der Strömung in Leitrad einer Kreiselpumpe, *Schweizerische Bauzeitung*, Vol. 86, No. 40, pp. 716-720, 1968.

[12] Lenneman E and Howard J H G. Unsteady Flow Phenomena in Centrifugal Impeller Passages, *ASME Journal of Engineering for Power*, Vol. 92,No. 1, pp. 65-72, 1970.

[13] Jansen W. Rotating stall in a radial vaneless diffuser, *ASME Journal of Basic Engineering*, Vol. 86, pp.750-758, 1964.

[14] Yoshida Y, Murakami Y, Tsurusaki T and Tsujimoto Y. Rotating Stalls in Centrifugal Impeller/Vaned Diffuser Systems, *Proceedings of First ASME/JSME Joint Fluids Engineering Conference*, FED-107, pp. 125-130, Portland.

[15] Ogata M and Ichiro A. An Experimental Study of Rotating Stall in a Radial Vaned Diffuser, *Unsteady Aerodynamics and Aeroelasticity of Turbomachines*, pp. 625-641, 1995.

[16] Manish Sinha, Ali Pinarbasi and Joseph Katz. The Flow Structure during Onset and Developed States of Rotating Stall within a Vaned Diffuser of a Centrifugal Pump, *ASME Journal of Engineering for Power*, Vol. 123, pp. 490-499, 2001.

[17] Stefan Berten, Maher Kayal, Philippe Dupont, Francois Avellan, Laurent Fabre and Mohamed Farhat. Experimental Investigation of Flow Instabilities and Rotating Stall in a High-Energy Centrifugal Pump Stage, *ASME Fluids Engineering Division Summer Meeting (FEDSM2009)*, pp. 2-5, 2009, Vail, CO, USA.

[18] Y.Y Ni, S. Q Yuan, Z. Y Pan, J. P Yuan. Detection of Cavitation in Centrifugal Pump by Vibration Methods, *Chinese Journal of Mechanical Engineering*, Vol. 21, No. 5, pp. 46-49, 2008.

[19] Tomaž Rus, Matevž Dular, Marko Hocevar, Igor Kern. An Investigation of the Relationship between Acoustic Emission, Vibration, Noise, and Cavitation Structures on a Kaplan Turbine, *ASME Journal of Fluids Engineering*, Vol. 129, pp. 1112-1122, 2007.

[20] Johnson D A, Pedersen N, Jacobsen C B. Measurements of Rotating Stall inside a Centrifugal Pump Impeller, *ASME Fluids Engineering Division Summer Meeting and Exhibition*, pp. 19-23, 2005, Houston, TX, USA.

[21] Pedersen N, Larsen P S, Jacobsen C B. Flow in a Centrifugal Pump Impeller at Design and Off-Design Conditions—Part I: Particle Image Velocimetry (PIV) and Laser Doppler Velocimetry (LDV) Measurements , *ASME Journal of Fluids Engineering*, Vol. 125, pp. 61-72, 2003.

[22] R. Xie, Z. Y Pan, J. J Li, J. R Liu. Influences of Various Inlet Flow Structure on the Pump Performance, *Third International Conference on Information and Computing*, Vol. 86-89, Wuxi, Jiangsu, China, June 4-6, 2010.

[23] Sanker L Saha, Junichi Kurokawa, Jun Matsui and Hiroshi Imamura. Suppression of Performance Curve Instability of a Mixed Flow Pump by Use of J-Groove, *ASME Journal of Fluids Engineering*, Vol. 122, pp. 592-597, 2000.

[24] Masahiro Miyabe, Hideaki Maeda, Isamu Umeki and Yoshinori Jittani. Unsteady Head-Flow Characterisic Generation Mechanism of a LowSpecific Speed Mixed Flow Pump, *Journal of Thermal Science*, Vol. 15, No. 2, pp. 115-120,2006.

[25] Masahiro Miyabe, Akinori Furukawa, Hideaki Maeda and Isamu Umeki. Rotating Stall Behavior in a Diffuser of Mixed Flow Pump and Its Suppresion, *ASME Fluids Engineering Conference*, pp.10-14, 2008, 8, Jacksonville, FL, USA.

[26] Takeshi Sano, Yoshiki Yoshida, Yoshinobu Tsujimoto, Yuki Nakamura and Tatsuhito Matsushima. Numerical Study of Rotating Stall in a Pump Vaned Diffuser, *ASME Journal of Fluids Engineering*, Vol. 124, pp. 363-370, 2002.

[27] Byskov R K, Jacobsen C B and Pedersen N. Flow in a Centrifugal Pump Impeller at Design and Off-Design Conditions—Part II: Large Eddy Simulations, *ASME Journal of Fluids Engineering*, Vol. 125, pp. 73-83, 2003.

[28] Yoshinobu Yamade, Chisachi Kato, Hayato Shimizu and Takahide Nagahara. Large Eddy Simulation of Internal Flow of a Mixed-Flow Pump, *ASME Fluids Engineering Division Summer Meeting (FEDSM2009)*, pp. 2-5, August, 2009, Vail, CO, USA.

[29] Wang H, Tsukamoto H. Experimental and Numerical Study of Unsteady Flow in a Diffuser Pump at off-design Conditions, *ASME Journal of Fluids Engineering*, Vol. 125, pp. 767-777, 2003.

[30] Saha S L, Kurokawa J, Matsui J and Imamura H. Passive Control of Rotating Stall in a Parallel-Wall Vaned Diffuser by J-Grooves, *ASME Journal of Fluids Engineering*, Vol. 123, pp. 507-515, 2001.

Copyright © 2012 DET Corp., Japan All Rights Reserved
International Journal of Comprehensive Engineering
Part C, 2(2), 208-214, 2013
Doi: 10.14270/IJCE2013.2.2.c208
Regular paper

ISSN 2186-2680
e-ISSN 2186-2656
www.iace-journal.org

Non Destructive Estimation Method about the Texture of Raw Puffers Meat on its Frequency Response

-- Identification of Optimum Discriminati on Sensitivity by Discrimination Index--

Hiromitsu Ohta [1,#], Keiji Sasada [2], Shintaro Shiota [2] and Makoto Nakamura [1]

[1] Department of Ocean Mechanical Engineering, National Fisheries Univerisity,
2-7-1, Nagatahon-machi, Shimonoseki, Yamaguchi, 759-6595, Japan
[2] Graduate Student, Graduate School of Fisheries Science, National Fisheries University

[#] Corresponding author: ohta@fish-u.ac.jp; Tel.: +81-83-286-5111; Fax: +81-83-286-7433

Abstract: Delicious taste of raw puffer meat in the seafood has been fundamentally determined by the texture and its degree of freshness in Japan market. If more exact and quantitative estimation method on delicious taste of puffer meat is desired, the method associated with non destructive, convenient and prompt one is most suitable. The texture of raw puffer meat is defined as its stiffness associated with mechanical dynamics. This paper proposes a novel non destructive estimation method on stiffness of raw puffer meat. The proposal method has been exercised by the evaluation based on frequency response function using a wide frequency obtained from the vibration test on the target puffer meats. Furthermore, an optimum narrow band excitation frequency to obtain the optimum discrimination sensitivity on the stiffness that is one of the texture between Tiger puffers meats and Sirosaba puffer ones is identified by applying the Discrimination Index (DI) which is derived by the statistical theory of probability and Young's modulus experimentally obtained by the destructive compression test. The proposed method is characterized by non destructive, quantitative, speedy and concise procedure more than conventional destructive method such as compression test.

Keywords: Texture, Frequency Response Function, Raw Puffer Meat, Nondestructive Testing, Stiffness, Discrimination Index.

Received: May 25,2012 / Accepted: Feb. 20,2013 / Published: Jul. 5,2013

1. Introduction

In Japan fisheries industry, the quality of raw fish meat is evaluated from many factors which are its freshness, texture, visual effect and chemical components including meat. However, most important factor to decide delicious taste of fishery products is known as depending on kind of fishery products. For example, delicious taste of raw tuna meat is obviously depended on the quantity of fat including the tuna one [1,2]. Japanese has quite an appetite for raw puffer meat since early times. The delicious taste of raw puffer meat has been mostly evaluated from the texture (stiffness) on account of ingenious taste compared with other fishery products [3], because the delicious taste of puffer meat don't depends on the quantity of chemical abundance including puffer meat such as fats. The quality evaluation of raw puffer meats has been generally carried out by the cognoscenti in marketplaces. The precision of quality evaluation is dependent on skill level of the cognoscenti in the market. Consequentially, the quality evaluation method which is independent on individual shill level has been desired in fisheries industry. Additionally, to deal with fishery products which are important associated with freshness, speedy, convenient, quantitative and non destructive method has been especially desired. As mentioned above, in our research, a novel texture (stiffness) estimation method on raw puffer meat based on frequency response function has been proposed [4,5], to be more precise, so called stiffness [6] correspond to the texture can be estimated from frequency response function obtained by an excitation experiment added in a wide sweep signal.

Proposed stiffness value is evidenced by young's modulus of raw puffer meat measured by compression test. Tendency between proposed value and evidenced one agrees well, however, sensitivity of both methods is difference. So it would appear that sensitivity correlation of both values. Consequentially, sensitivity agreement excitation frequency between each puffer meats is identified by Discrimination Index (DI) which can be derived by the statistical theory of probability and average and standard deviation values of Young's modulus obtained from the compression test targeting puffer meats.

2. Experimental and Analytical Equipments & Theorem of Discrimination Index

2.1 Experimental and Analytical Equipments

Applied experimental setup and a measurement bed can be shown in Fig.1and Fig.2 respectively. A puffer meat is located on the measurement bed to measure the frequency response, additionally, poisonous bowels of raw puffer can be removed, the raw puffer meat of the removal state is usually regarded as "migaki" in Japanese. The puffer meat of migaki state is fixed in the aluminium plate by using a suction pump. A shaker located in the bottom of measurement bed includes the frequency modulated sweep signal (0～300[Hz]) in the raw puffer meat in "migaki" state, a force transducer located in the center of the measurement bed can estimate empty weight of the raw puffer meat and a sucking force by the suction pump. A three dimensional acceleration pickup is fixed on the raw puffer meat using an adhesive disc sucked in the suction pump, additionally, an acceleration pickup is located on the top of the force transducer, and can measure the acceleration value in the

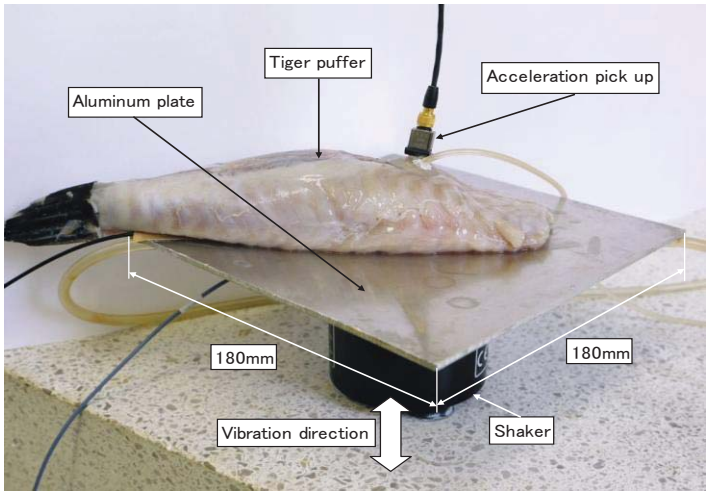

Fig. 1 Applied experimental setup

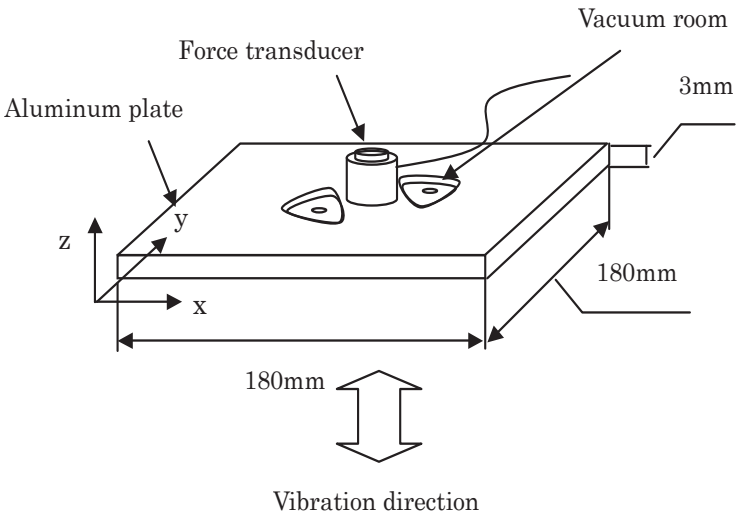

Fig. 2 The measurement bed

vertical direction which is equal to the excitation one. The frequency response function of the raw puffer meat can be estimated from above force transducer and acceleration pick up shown in Fig.1 and Fig.2. At the same time, in the case of evidenced stiffness value applied by young's modulus, the dimension of all puffer meats applied by the compression test are unified at the size 30×30×10[mm] shown in Fig.3. The Young's modulus of the raw puffer meat can be obtained from elongation of elastic region between the applied stress 30[kPa] and 60[kPa] shown in Fig.4, kind of applied raw puffers are typical two kinds in Japan, so called Tiger puffer and Sirosaba puffer and the number of applied each puffers are 17 and 23 respectively.

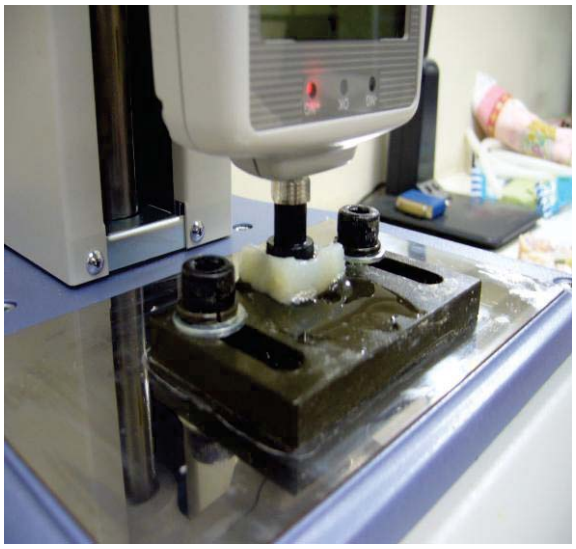

Fig. 3 The compression test view of a puffer meat

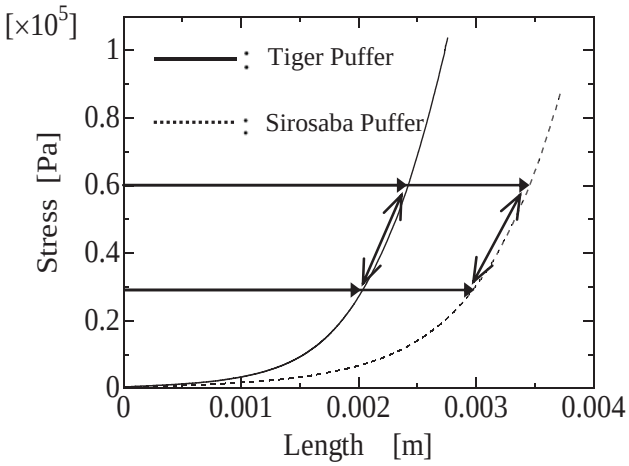

Fig. 4 The Stress-length diagram of puffer meats

2.2 Derivation of Discrimination Index

Discrimination Index (DI) decides the sensitivity agreement excitation frequency to agree the sensitivity of estimation and evidence values. DI has been fundamentally used for attempting the quantitative evaluation of the sensitivity among two parameters. If the respective distributions of parameter p_1 and p_2 shown in Fig.5 obey Gaussian distribution, the probability density function of parameter p_2-p_1 can be obtained by Eq.(1)

$$f(p_2 - p_1) = \frac{1}{\sqrt{2\pi(\sigma_2^2 + \sigma_1^2)}} \exp\left(-\left(\frac{(p_2 - p_1 - (\mu_2 - \mu_1))^2}{2(\sigma_2^2 + \sigma_1^2)}\right)\right. \tag{1}$$

Here ,μand σin the Eq.(1) show the average and the deviation values of the parameter p_1 and p_2,respectively. μandσvalues can be expressed by below Eq.(2) and (3). Additionally, constant N represents the data number of value x_s(i).

$$\mu_i = \frac{1}{N}\sum_{i=1}^{N} x_s(i) \tag{2}$$

$$\sigma_1 = \sqrt{\frac{1}{N-1}\sum_{i=1}^{N}\{x_s(i) - \mu_1\}^2} \tag{3}$$

If the average values μ_1 and μ_2 of the parameter p_1 and p_2 are $\mu_1 > \mu_2$, indiscernible area in Fig.5 is $P_1 > P_2$. The smaller the area is, the more the discrimination sensitivity of the parameter p increases.

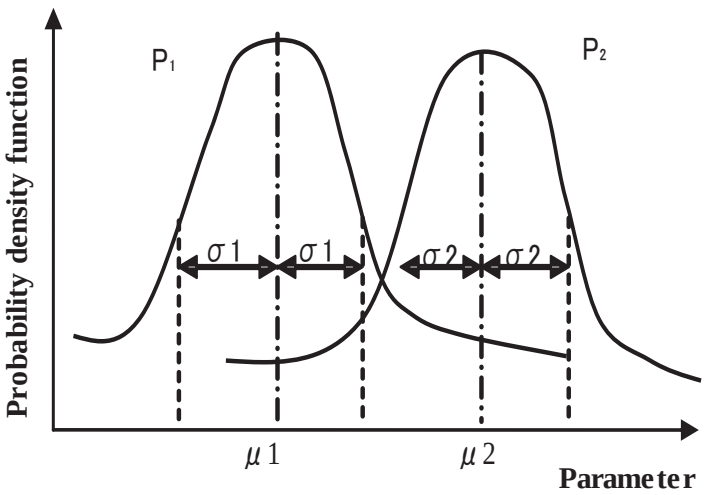

Fig. 5 Gaussian distribution of parameters p_1 and p_2

Here, the probability of P_2—P_1＜0 can be obtained by below Eq.(4)

$$P_P = \int_{-\infty}^{0} f(p_2 - p_1) d(p_2 - p_1) \tag{4}$$

We can perform change of variables u shown in Eq.(5) to Eq.(1).

$$u = \frac{p_2 - p_1 - (\mu_2 - \mu_1)}{\sqrt{\sigma_2^2 + \sigma_1^2}} \tag{5}$$

Then, Eq.(4) can be converted to Eq.(6).

$$P_P = \frac{1}{2\pi} \int_{-\infty}^{-\frac{\mu_2 - \mu_1}{\sqrt{\sigma_2^2 + \sigma_1^2}}} \exp(-\frac{u^2}{2}) du \tag{6}$$

The absolute value of upper limit of the integral on Eq.(6) can be defined as the Discrimination Index (DI) shown in Eq.(7). In short, DI can be simply expressed by average and deviation values of parameter p_1 and p_2.

$$DI = \frac{|\mu_1 - \mu_2|}{\sqrt{\sigma_1^2 + \sigma_2^2}} \tag{7}$$

3. Analytical Results and Consideration

Fig.6 represents the histograms of evidence values which are correspond to young's modulus of raw Tiger and Sirosaba puffer meats respectively. Average value of young's modulus on Tiger puffers is about 36.07 [MPa], its standard deviation of above case shows 6.84, at the same time, Young's modulus and its standard deviation in the case of Sirosaba puffer are about 25.90[MPa] and 4.46 respectively. Fig.6 makes it perfectly obvious to someone that Tiger puffer's values on young's modulus are generally higher than Sirosaba puffer's values, Discrimination Index (DI) between Sirosaba and Tiger puffers on these young's modulus calculated by Eq.(7) is 1.25. Fig.7 shows the histogram of the average frequency response function value (stiffness) obtained from frequency modulated signal (Sweep signal) 0 to 300[Hz] of raw Tiger and Sirosaba puffers based on the proposed method. Fig.7 makes it perfectly obvious to someone that the sensitivity of discrimination in the case of proposed method is inferior to the evidence values obtained by the compression test. Effectiveness of

wide band excitation from frequency 0 to 300[Hz] must be evidenced at the next stage. Basically, there is a possibility that the estimated DI based on wide band excitation is lower than actual DI, to be calculated average values of wide band excitation from 0 to 300[Hz]. Fig.8 shows a typical frequency response function form correspond to weight and kind of each puffers. To consider the effectiveness of wide band excitation, integrated DI which represents sum of each DI about frequency response function from 0 to 300[Hz] can be evaluated in Fig.9,10 and 11. There is a trend toward sudden decrease of DI along with increase of frequency, generally, sensitivity of discrimination increases in proportion as DI value increases. The DI obtained by a compression test is 1.14 shown in Fig.3, in the vicinity of intersection between proposed and evidenced methods is instability to possess the drastic transformation. For the above reason, evaluation of the stiffness by the wide band excitation is infelicity. Secondly, effectiveness of single frequency excitation must be evidenced. Fig.12 shows the variety of the DI correspond to each frequency, the sensitivity of DI along with increase of frequency is relatively stabilized than the sensitivity of integrated DI, consequently, estimation of stiffness by single frequency excitation is more acceptable than the wide band one. Most optimum excitation frequency of puffer meat is about 40[Hz] judging from the intersection in Fig.12. Fig.13 represents the histogram of stiffness based on frequency response function estimated by single excitation frequency 40[H], the sensitivity of discrimination on texture (stiffness) is apparently improved compared to the histogram of Fig.7 in the case of the wide band excitation. It demonstrates that estimation method of stiffness based on identified single excitation frequency is acceptable.

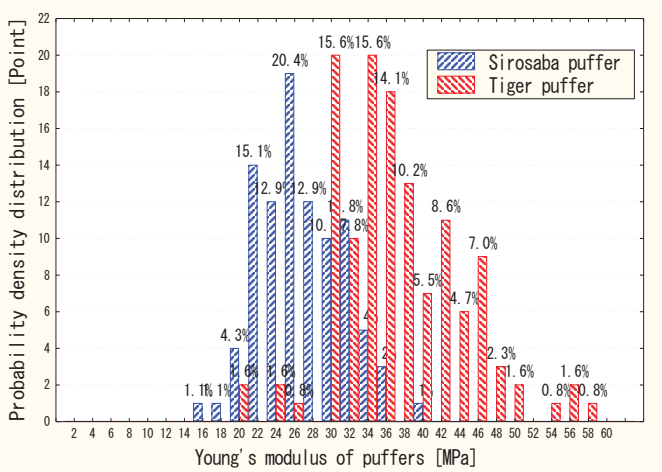

Fig. 6 Histogram of Young's modulus of puffer meats

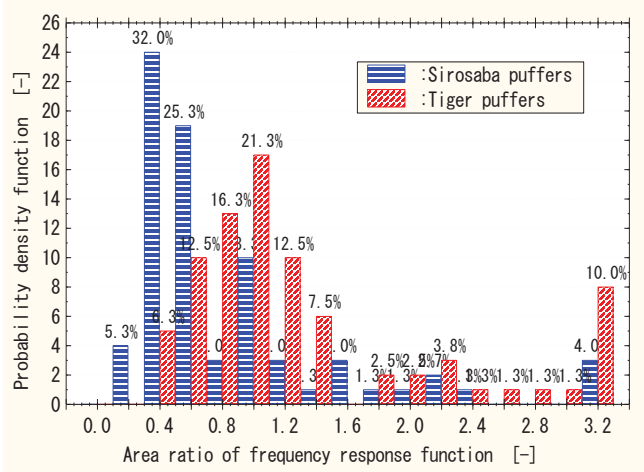

Fig. 7 Histogram of the stiffness by the proposed method

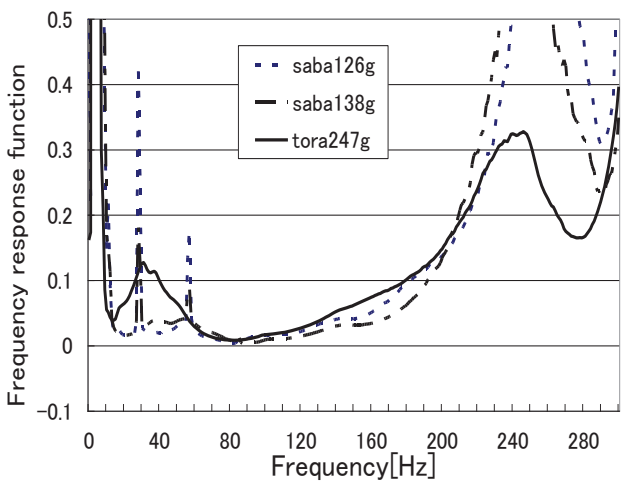

Fig. 8 Typical frequency response function of puffer meats

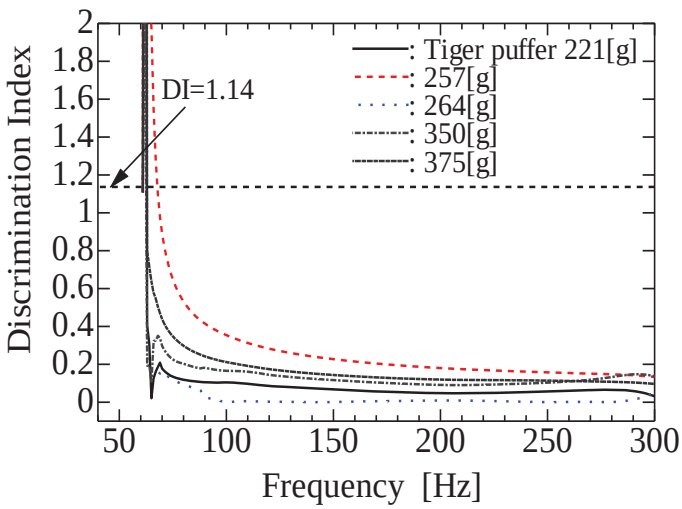

Fig. 9 A DI of Sirosaba puffer 148[g] against Tiger puffers

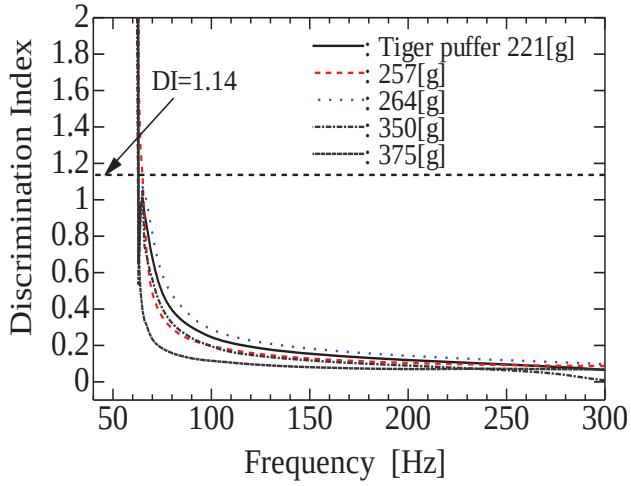

Fig. 10 A DI of Sirosaba puffer 139[g] against Tiger puffers

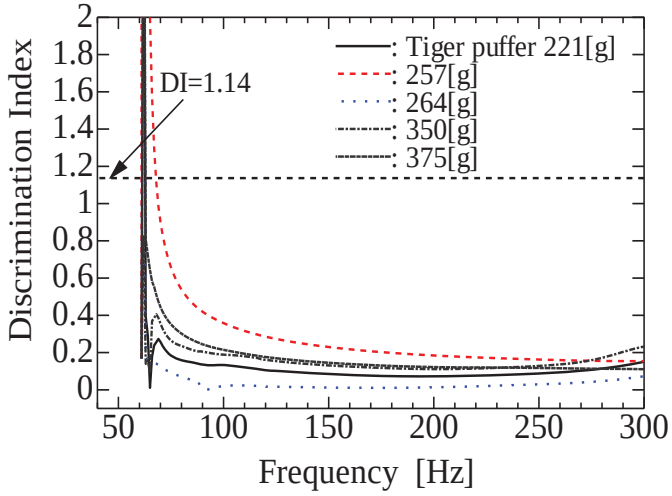

Fig. 11 A DI of Sirosaba puffer 124[g] against Tiger puffers

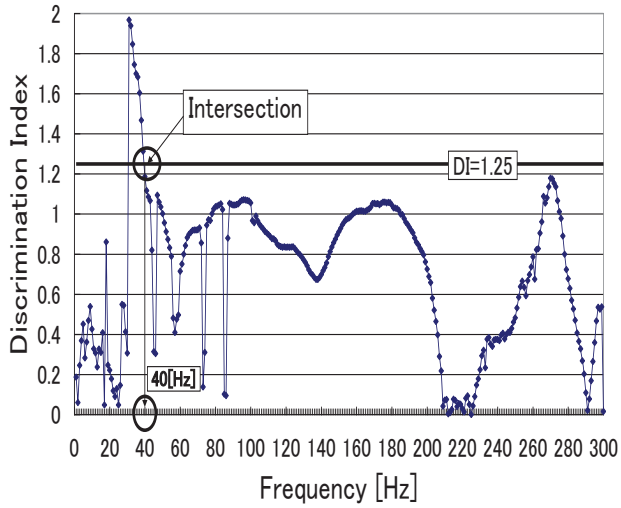

Fig. 12 A DI of each shaken frequencies

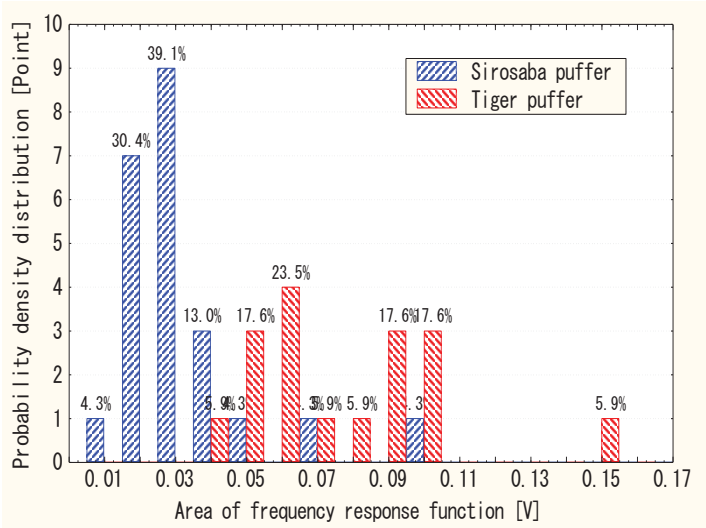

Fig. 13 Improved histogram of stiffness based on single shaken frequency (40Hz)

4. Conclusions

The delicious taste of raw puffer meat has been mostly evaluated from the texture (stiffness) on account of ingenious taste compared with other fishery products. The texture of raw puffer meat is defined as its stiffness associated with mechanical dynamics. This paper experimentally proposes a novel estimation method on stiffness of raw puffer meat. The proposed method has been exercised by the evaluation based on frequency response function obtained from puffer meats. The proposed method is characterized by non destructive, quantitative, speedy and concise procedure more than conventional destructive method such as compression test. Additionally, to improve estimation accuracy of proposed method, acceptable single excitation frequency is identified from the Discrimination Index which statistically discriminates sensitivity of two parameters. The sensitivity of discrimination on stiffness between Tiger puffer meat and Sirosaba puffer one is apparently improved by the identified optimum single excitation frequency.

References

[1] H. Ohta, K. Seto and S. Ezoe. Estimation Method about Amount of Fish Fat Using Ultrasonic Sensor, *International Transaction on Acoustic Science and Engineering*, Vol. 4, No. 11, pp. 9-18, 2005.

[2] H. Ohta, K. Seto and T. I. Khan. Estimation Method about Amount of Fat on Tuna Using Ultrasonic Sensor, *The 9th Western Pacific Acoustics Conference (WESPAC IX), Proceedings of WESPAC IX*, pp. 578-584, 2006.

[3] Y. Aoki. *Culture of Puffers*, Seizando Publishing Company, pp. 69-77, 1999.

[4] H. Ohta, M. Nakamura, S. Ezoe and E. Morimoto, Nondestructive Evaluation Method about the Texture of Puffer Meat, *JSME 12th Asia Pacific Vibration Conference (APVC2007)*, pp.124-130, 2007.

[5] H. Ohta, K. Sasada and M. Nakamura. Non Destructive Evaluation Method about the Texture of Puffers Meat on Its Response, *Proceedings of the 23nd International Congress Condition Monitoring and Diagnostic Engineering Management (COMADEM 2010)*, pp. 377-380, 2010.

[6] A. Nagamatsu. *Introduction to Modal Analysis*, Corona Publishing Company, pp.15-19, 1993.